Experiment ECOKATS-2 On Melt Spreading and Subsequent Top Flooding

Test and Data Report

**CONTRACT FIKS-CT1999-00003
EX-VESSEL CORE MELT
STABILIZATION RESEARCH**

**H. Alsmeyer, T. Cron, J. J. Foit,
G. Messemer, S. Schmidt-Stiefel,
W. Häfner, H. Kriscio**

**Institut für Kern- und Energietechnik
Programm Nukleare Sicherheitsforschung**

Januar 2005

Forschungszentrum Karlsruhe

in der Helmholtz-Gemeinschaft

Experiment ECOKATS-2
On Melt Spreading and Subsequent Top Flooding
Test and Data Report

CONTRACT FIKS-CT1999-00003
EX-VESSEL CORE MELT STABILIZATION RESEARCH

H. Alsmeyer, T. Cron, J. J. Foit, G. Messemer, S. Schmidt-Stiefel,
W. Häfner*, H. Kriscio*

Institut für Kern- und Energietechnik
Programm Nukleare Sicherheitsforschung

*Becker Technologies, Eschborn, Germany

Abstract

As part of the ECOSTAR project sponsored in the 5th Framework Program of the European Commission, large-scale experiments on melt spreading were performed.

In the experiment ECOKATS-2, fast and complete spreading of a considerable quantity of melt was investigated, followed by subsequent top flooding with a prescribed water flow rate. 3200 kg high temperature melt were spread in a 2 m by 2 m concrete cavity. As a consequence of melt attack, the concrete was decomposed releasing a large gas flow, which penetrated through the melt layer. The influence of the melt/concrete interaction on the processes of spreading and subsequent cooling was an important part of the experiment ECOKATS-2.

The used large melt mass had the same composition as in the experiment ECOKATS-1. It was generated by a modified thermite reaction, which produced a heavier iron fraction of 895 kg and a lighter oxide fraction of 2305 kg. The melt was poured to the spreading area under controlled conditions with high release rate of 20 to 30 litres/s. Discharge of the melt was completed after 33 s and the melt evenly filled the cavity some 20 cm high a few seconds after the end of pouring. No decay heat was produced in the melt, so that spreading and concrete erosion were controlled by the initial overheat of the melt.

During intense concrete erosion, about 30 s after the end of spreading, the surface of the melt was flooded with coolant water, which was supplied from one side of the spreading area with 4 liters/s. The contact of the water with the upper oxide melt layer was very smooth and did not produce energetic melt/water interactions. A closed surface crust was formed that firmly anchored to the vertical sidewalls of concrete. The crust at the wall was stable throughout the test, whereas in the center of the spreading cavity the initially flat crust was slowly elevated by up to 20 cm, probably driven by gas release from the concrete. Also 16 volcanic vents piled up through which some melt was expelled in the form of lava flow, but their contribution to melt coolability was small.

The majority of the melt under the crust was not fragmented, and solidified as a compact layer without open porosity. This showed that ingression of coolant water to the bulk of the melt was not possible. Also, no significant cracks were visible in the lower solidified melt. Only the uppermost 4 cm of the dense (unvoided) oxide melt were transferred into a configuration that was coolable due to its high porosity, whereas the bulk of the oxide melt and the iron layer at the bottom were not cooled by water ingression from the top.

With respect to reactor application it is concluded that top flooding alone is not sufficient to extract the decay heat from a deep corium melt and to stop concrete erosion.

According to the deliverables of the ECOSTAR contract this report is divided into the two main chapters "Spreading" and "Top Flooding". In each chapter the required test report with the data report is given.

The report includes the following deliverables of the ECOSTAR contract:

WP 2.1, 2-D Spreading: Part D14; Test report.
                                        Part D16; Data report.

WP 3.4.2ab; Coolability/Top Flooding: Part D39; Data set of experimental results.
                                        Part D40; Evaluation and test report.

Experiment ECOKATS-2:
Schmelzenausbreitung mit anschließender Kühlung von oben

Zusammenfassung

Im Rahmen des ECOSTAR-Projekts wurden Experimente zur Ausbreitung von Schmelzen in großem Maßstab durchgeführt. Sie waren Teil des 5. Rahmenprogrammes, welches von der europäischen Gemeinschaft unterstützt wurde.

Im Experiment ECOKATS-2 wurde die schnelle, vollständige Ausbreitung einer großen Schmelzenmenge untersucht, die anschließend durch Aufgabe von Wasser auf ihre Oberfläche geflutet wurde. Es wurden 3200 kg heißer Schmelze auf einer 2 m x 2 m großen Betonfläche ausgebreitet. Als Folge des Angriffs durch die Schmelze zersetzte sich der Beton und setzte eine große Menge von Gas frei, die durch die Schmelze abströmte. Der Einfluss der Schmelze/Beton-Wechselwirkung auf den Vorgang der Ausbreitung und die anschließende Abkühlung war ein wichtiger Schwerpunkt des Experiments.

Die große Schmelzenmasse wurde durch eine modifizierte Thermitreaktion erzeugt, mit der gleichen Zusammensetzung wie beim Experiment ECOKATS-1. Sie bestand aus einer schweren Fraktion mit 895 kg Eisen und einer leichteren Fraktion mit 2305 kg Oxid. Die Schmelze wurde unter kontrollierten Bedingungen mit einem Volumenstrom von 20 bis 30 Liter/s auf die Ausbreitfläche aufgegeben. Nach 33 s war der Ausströmvorgang beendet und einige Sekunden später war die Ausbreitfläche ca. 20 cm hoch gleichmäßig mit Schmelze gefüllt. In der Schmelze wurde keine Nachzerfallswärme simuliert, sodass sich die Ausbreitung und die Betonerosion alleine durch die Überhitzung der Schmelze einstellten.

Während der heftigen Betonerosion, ungefähr 30 s nach Ende der Ausbreitung, wurde die Oberfläche der Schmelze mit 4 Liter Wasser/s geflutet, das von einer Seite der Ausbreitfläche aufgegeben wurde. Der Kontakt des Wassers mit der oberen Schicht der Oxidschmelze verlief sehr mild und erzeugte keine heftigen energetischen Reaktionen. Während des Flutens entstand eine geschlossene Schmelzenkruste, die sich mit den Betonwänden verankerte. Die Kruste an der Wand blieb bis zum Ende des Experiments stabil, während sich die Kruste im Zentralbereich der Fläche langsam um bis zu 20 cm anhob, vermutlich getrieben durch die Gase aus der Betonerosion. Es bildeten sich 16 Vulkankegel, durch die etwas Schmelze als Lavastrom austrat, aber ihr Beitrag zur Kühlung der Schmelze war gering

Der größte Teil der Schmelze unterhalb der Kruste wurde nicht fragmentiert, sondern erstarrte als kompakte Schicht ohne offene Porosität. Dies zeigt, dass ein Eindringen des Kühlwassers von oben in den Zentralbereich der Schmelze nicht möglich war. Weiterhin waren keine wesentlichen Risse in der unteren Schmelze vorhanden. Lediglich die oberen 4 cm der zunächst kompakten Schmelze erstarrten als offenporige Kruste, die wegen ihrer hohen Porosität kühlbar war. Der Zentralbereich der Schmelze und die unten liegende Eisenschicht wurden nicht durch Eindringen von Kühlwasser gekühlt.

Im Hinblick auf die Anwendung für den Reaktor wird gefolgert, dass Wasseraufgabe auf die Schmelze alleine nicht ausreicht, um die Nachwärme aus einer dickeren Schmelzeschicht ausreichend abzuführen und die Betonerosion zu stoppen

Entsprechend den Aufgabenpaketen im ECOSTAR-Vertrag ist der vorliegende Bericht in die wesentlichen Teile „Spreading" und „Top Flooding" gegliedert. In jedem Teil werden die geforderten experimentellen Ergebnisse mit den dazugehörenden Messdaten dokumentiert.

Der Bericht enthält die zu liefernden Berichtseinheiten des ECOSTAR-Vertrages:
WP 2.1, 2-D Spreading: Part D14; Test report.
                        Part D16; Data report.
WP 3.4.2ab; Coolability/Top Flooding: Part D39; Data set of experimental results.
                        Part D40; Evaluation and test report.

CONTENTS

List of Figures

List of Tables

1   Introduction

To mitigate and control ex-vessel corium melts in the case of core melt accidents, spreading of the melt on the available basement and subsequent flooding of the melt are important processes under consideration for existing and future LWRs. These processes are studied in the ECOKATS experiments, which are part of the ECOSTAR Programme, co-sponsored in the 5th Framework Programme of the European Commission [1].

From the hydrodynamic point of view, melt spreading is strongly influenced by the initial conditions of the melt flow, predominantly by the release rate and the viscosity of the melt. Heat losses may delay or even stop the spreading process if parts of the melt start to freeze. Therefore, the initial melt overheat is also important, as well as the viscosity increase during transition of the melt from liquid to solid, which in most cases is characterized by a wide freezing interval, as the melt consists of a mixture of oxides, such as UO_2, ZrO_2, and decomposing concrete.

For many light water reactors, discharge of the melt from the reactor pressure vessel to the concrete floor occurs under dry conditions. As a consequence of melt attack, the concrete starts to decompose and releases large amount of steam, penetrating through the melt layer. This may have an important influence on the processes of spreading and subsequent cooling, as investigated in various tests, see e.g. [2] and [3]. Incomplete spreading on a large concrete surface under low flow conditions has been investigated recently in the ECOKATS-1 test in combination with benchmarking of detailed codes which shall be used for the analysis of accident situations under various conditions [4].

Successful spreading is important to minimize the melt height and therefore to enhance the cooling process when water is added to the melt. These are the conditions that were realized in the actual ECOKATS-2 experiment. Shortly after completion of the spreading process the melt was flooded from the top by adding water from one side of the large cavity, a process that could be the result of an accident management procedure in case of an accident. While it is realized that melt coolability by a water overlayer may be hard to achieve for thicker melt layers and alternative cooling methods are being investigated [5], it is required to quantify the dominant cooling mechanisms and the cooling efficiency during top flooding.

The MACE experiments on the efficiency of top flooding have been performed at ANL with simulation of decay heat in the melt, which contained Uranium oxide and other relevant oxides. The size of the test section was from 30 cm x 30 cm to 120 cm x 120 cm. The experiments have shown that heat removal is restricted by a surface crust that attached itself to the sidewalls of the test section and eventually separated from the melt [5], [6]. The tests also showed the eruption of some melt material through the crust into the water overlayer, contributing to the formation of a coolable particle layer. This process was, however, not sufficient to achieve stop of concrete erosion and arrest of the melt. During the largest test with a surface of 120 cm x 120 cm, separation of the melt from the crust was counteracted by a planned increase of the simulated decay power, which increased the melt level. A substantial part of the melt was subsequently ejected through volcanic eruptions.

From these experiments and additional theoretical investigations, the following phenomena during top flooding needed further clarification and are the objectives of the present ECOKATS-2 experiment:

- The possibility of vigorous melt-water interactions during top flooding

- The role of bulk cooling during the first melt/water contact

- The existence of an anchored or floating crust for the large size of the reactor cavity

- The formation of cracks in the surface crust and their role for water ingression

- Rate and duration of (volcanic) particle ejection driven by gas release from the decomposing concrete.

To perform the planned experiment ECOKATS-2, the existing test facility and the measuring equipment were adequately adapted. The main components were (1) the existing thermite crucible to generate and release the mass of 3200 kg of thermite melt (never used before with this very large mass of thermite melt), with controlled opening of the melt release valve and a reliable weighing system, (2) the whirl basin, (3) the spreading cavity to which the melt was released, with all the necessary instrumentation and (4) the thermal resistant water basin for top flooding with the equipment for the controlled water supply.

The new parts had to be designed and supplied, and the components had to be assembled and tested.

2   2-D Spreading Experiment ECOKATS-2

2.1   Description of the Experiment (D14)

2.1.1 Main Test Parameters

The experiment ECOKATS-2 was designed as a large-scale experiment allowing spreading and flooding of the melt in a 2 m x 2 m concrete cavity (see Figure 2-1 and Figure 2-2). The large dimensions should reduce the influence of the sidewalls, especially with respect to the possible formation of an anchored or floating crust, and make the geometrical conditions, as far as technically feasible, comparable to the situation in the reactor cavity with a typical dimension of 6 m. Furthermore, the minimum height of the melt after complete spreading should be some 20 cm or more to allow the occurrence of cooling and crust formation at the melt surface, while the bulk of the melt is agitated by the gases from concrete erosion. The required melt volume is therefore > 0.8 m^3.

This big melt volume did not permit the use of a UO_2-based corium melt. Furthermore, technical feasibility, especially the large cavity dimensions, did not allow application of sustained heating to the melt to simulate the nuclear decay heat during the test. Therefore, a simulant melt was selected for the test that was generated mainly by the thermite reaction of alumina with iron oxide and the admixture of further oxide additives. This melt with an initial temperature of more than 1800 °C would have sufficient overheat over the liquidus temperature to show the important effects also in a transient test. The missing decay heat should have no influence on the very fast process of melt spreading, but limits the relevant time during melt cooling by top flooding to a period of 10 to 20 minutes, which should be sufficient to observe the most important phenomena of crusting and cooling.

The required melt mass of 3200 kg was generated by ignition of the specific thermite mixture in a separate crucible (Figure 2-1). After completion of the chemical reaction and separation of the lighter oxide melt on top and the heavier metal melt at the bottom within 3 minutes, the melt was released through a nozzle of the thermite crucible to the whirl basin, from which the melt passed through the horizontal 1-d flow channel which was 2.7 m long and 0.3 m wide. The melt then entered the large concrete surface for spreading and subsequent flooding. Because of the two melt phases first a layer of metal melt of about 2.7 cm and then a layer of oxide melt of about 14.3 cm (without void) covered the spreading area.

The whirl basin eliminated the downward momentum of the melt from the thermite crucible, so that the spreading process was driven only by gravity from overflow of the basin. The 1-d flow-channel and the large spreading area including the sidewalls were fabricated from silica concrete of German reactor specification as one single element, in order to have a highly even, well-defined geometry.

Flooding of the surface occurred over the full width of the backside of the spreading cavity via a distribution basin with a weir (Figure 2-1), initiated with 4.13 litre water/s after completion of the spreading process. Flow channel and spreading surface represented one half of a symmetric geometrical situation in a reactor with the long side of flow channel and spreading surface as symmetry line.

Similarly to ECOKATS-1, the instrumentation of the experiment consisted of load cells for the thermite crucible from which the release rate to the spreading surface was determined. Weight cells to which the spreading surface with flow channel and whirl basin are suspended gave additional information on the mass of the spread melt and the mass of the coolant water during the test. During the melt release high temperature W-Re-thermocouples measured the temperature of the melt in the whirl basin. Furthermore, 4 thermocouples modules in the spreading area were prepared to give information about the temperature of the melt and of the eroded concrete. The rate of coolant water was measured by a flow meter. Video cameras registered the spreading and flooding process from side and from top of the cavity. To facilitate geometrical interpretation, cross signs were drawn over the whole area in distances of 20 cm (see Figure 2-2).
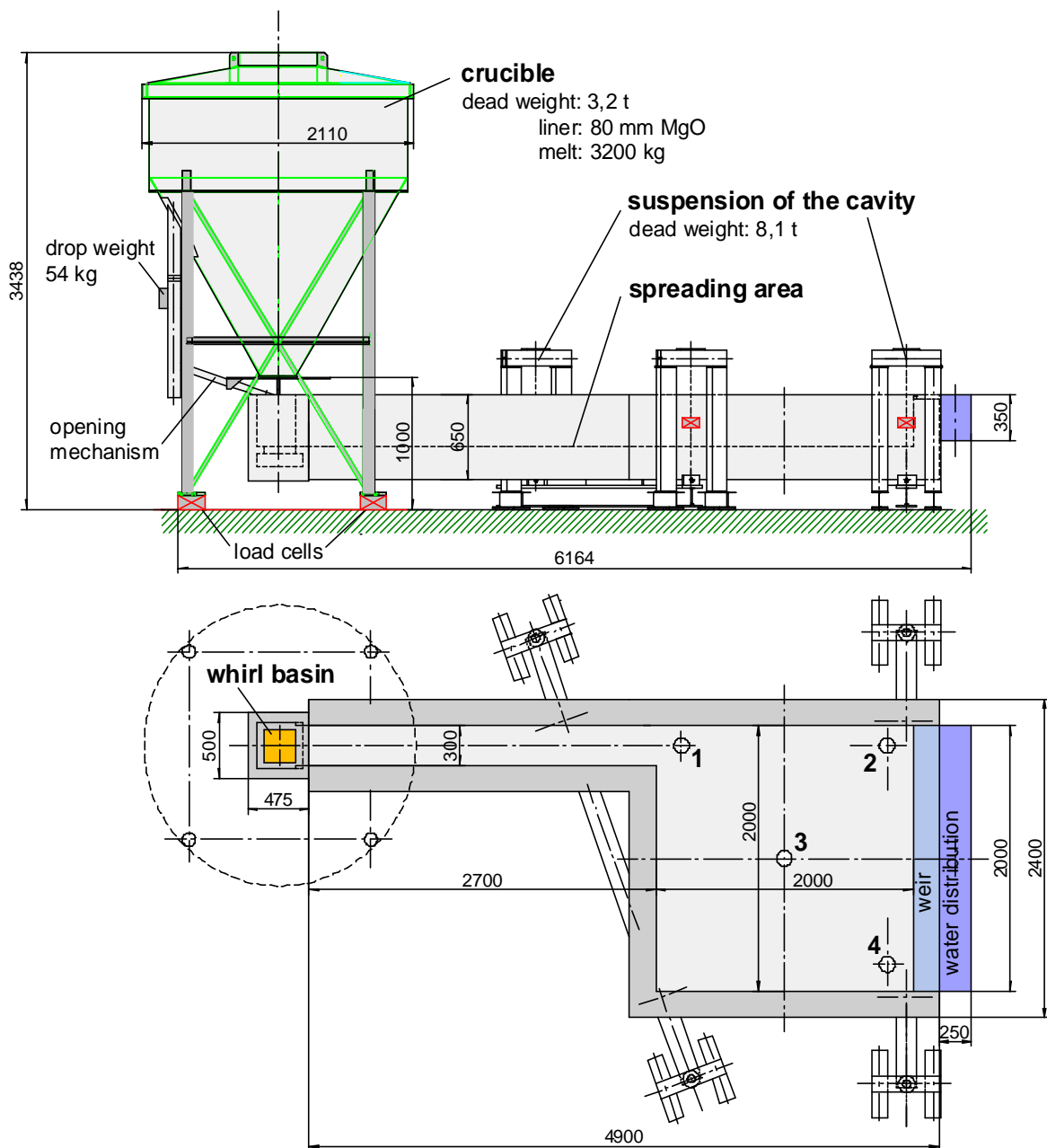
Figure 2-1: Arrangement of thermite crucible, whirl basin, spreading cavity and water distribution for the experiment ECOKATS-2

Test configuration ECOKATS-2
Thermite crucible in the background

Support leg of the spreading cavity
with load cell
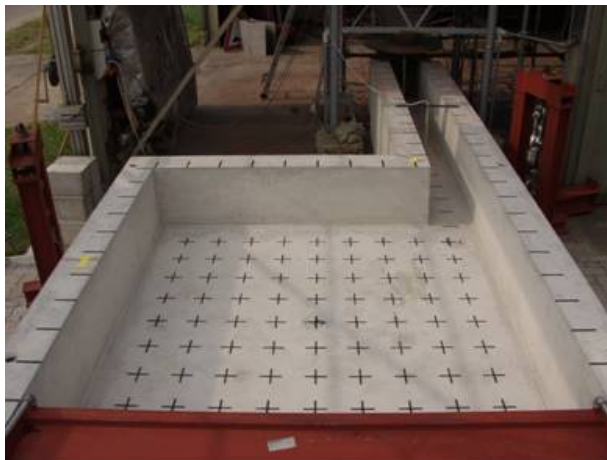
Spreading area with weir in front
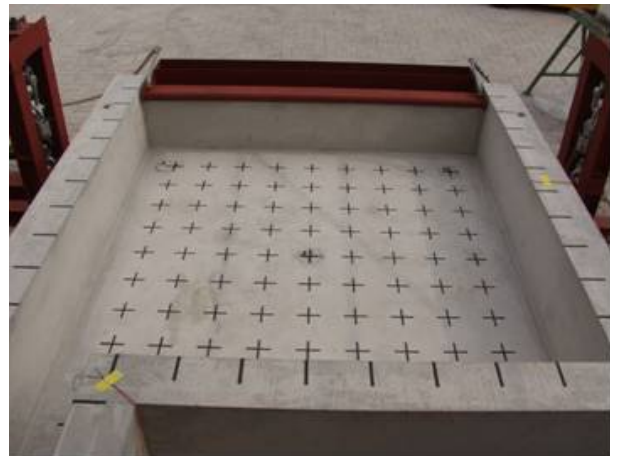
Spreading area
with water tank and weir in the background

Thermite crucible with load cells,
outlet to the whirl basin,
and supply channel

Test configuration ECOKATS-2 with scaffold
for the video observation

Figure 2-2: Assembly of the experiment ECOKATS-2

2.1.2 Melt Generation in the Thermite Crucible

The composition and physical properties of the simulant melt are very important because of the required correspondence to the corium melt. To produce the simulant melt, a thermite mixture of aluminium with iron oxide and the admixture of further oxide additives were selected. The composition of the 3200 kg thermite mix which was loaded to the thermite crucible is given in Table 1. Therein additionally the constituents of the melt products (2352 kg oxide and 848 kg metal) are listed. It shows that the oxide fraction of the melt is composed of a mixture of alumina, calcia, silica, and iron oxide. This composition was selected to have a wide freezing range which should be comparable to a corium melt after admixture of melted concrete products, however at lower temperatures. The melt freezing range was calculated using the GEMINI 2 code with the THERMODATA data base [11], as described in [8] (see Figure 2-3). The wide freezing range is important not only for the growth and stability of the crust, but also for the viscosity of the melt, which substantially increases, when by onset of crystallization in the agitated melt a slurry of crystals and liquid may be generated.

The melt with an initial temperature of more than 1800 °C would have sufficient overheat over the liquidus temperature to show the important effects also in a transient test. To reach a sufficiently high initial melt temperature, the thermite powder was preheated to 100 °C for at least 18 hours prior to its ignition.

To start the chemical reaction, 3 electrical igniters were placed inside the thermite powder. After completion of the chemical reaction and separation of the lighter oxide melt on top and the heavier metal melt at the bottom within 3 minutes, the melt was released to the whirl basin through a nozzle at the lowest point of the thermite crucible. The densities of the high temperature melts are 6771 kg/m^3 for the metal phase and 3263 kg/m^3 for the oxide phase [11].

Table 1: Mix of thermite powder and generated oxide and metal melt compositions for the experiment ECOKATS-2

Thermite Mixture		Oxide Melt 73.5 %		Metal Melt 26.5 %	
Constituent	**Mass**	**Constituent**	**Part**	**Constituent**	**Part**
Aluminum Thermite	2023.88 kg	Al_2O_3	41 %	Fe	˜100 %
CaO	493.97 kg	FeO	24 %	Si	<0.24 %
SiO_2	352.84 kg	CaO	19 %	Al	<0.30 %
Fe_2O_3	329.31 kg	SiO_2	16 %	Mn	0.01 %
Total	**3200.00 kg**	**Total**	**100 %**	**Total**	**100 %**
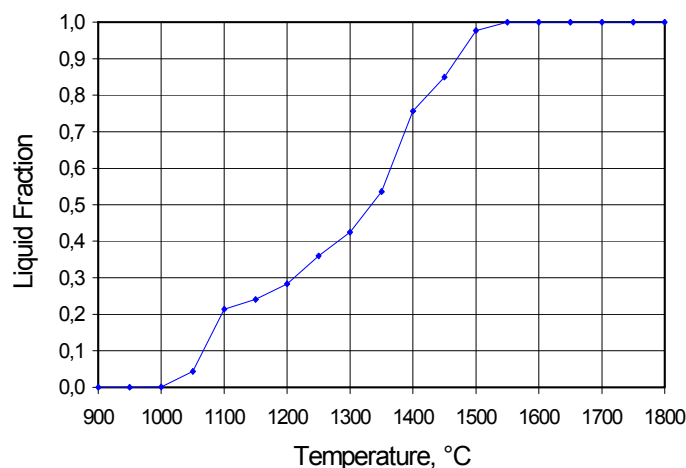
Figure 2-3: Calculated freezing range of the oxide melt

2.1.3 Spreading Cavity

The spreading cavity with the attached whirl basin is shown in Figure 2-4. In order to have a well-defined geometry the spreading cavity was fabricated as a single element of reinforced silica concrete of German reactor specification and had a very even, horizontal surface. The quadratic surface of the spreading area measured 2 m x 2 m. To supply the melt, a channel 0.30 m wide and 2.70 m long was attached on the left side. The base plate had a thickness of 0.25 m and was surrounded by a concrete wall 0.20 m wide and 0.40 m high. All the edges from the bottom to the sidewalls were rounded with a radius of 30 mm. To obtain the specified quality of industrial concrete the minimum curing time of 28 days was kept. With respect to melt inflow, flow channel and spreading area represent one half of a symmetric geometrical situation in a reactor, with the flow channel as symmetry line.

To measure the temperature of the incoming melt and the response and downward erosion of the concrete area, 4 instrumentation modules with various thermocouples were integrated in the spreading device. For this purpose, 4 openings were provided at selected measurement positions of the cavity, as shown in Figure 2-4. The modules were produced with complete wiring as separate plugs of concrete with a diameter of 120 mm and were inserted after fabrication flush with the inner surface of the cavity. A detailed description of the modules is given in section 2.1.7.

The whirl basin (Figure 2-5) was designed to eliminate the downward momentum of the melt when released from the thermite vessel, thus allowing quiet feeding to the spreading area driven by gravity flow from the whirl basin. The basin was fabricated as a steel case, coated with a ceramic liner. The whirl basin was directly mounted to the supply channel and thus its mass was determined together with the spreading cavity. During the experiment its retention volume of 15.4 litres should be totally filled with metallic melt of about 100 kg.
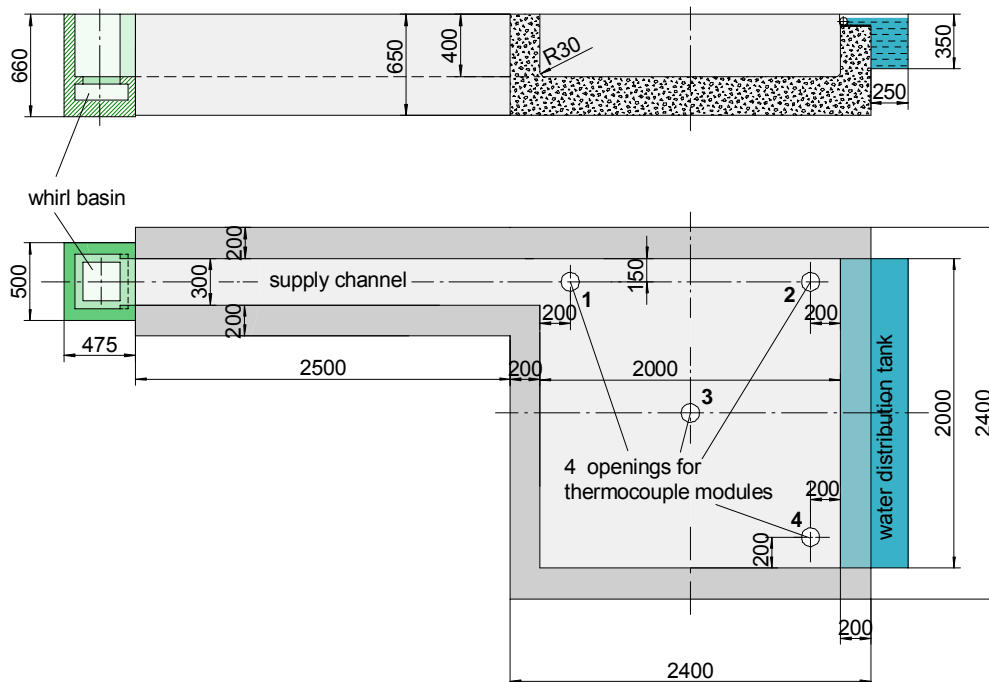
Figure 2-4: Spreading cavity of concrete with attached whirl basin and water tank

7
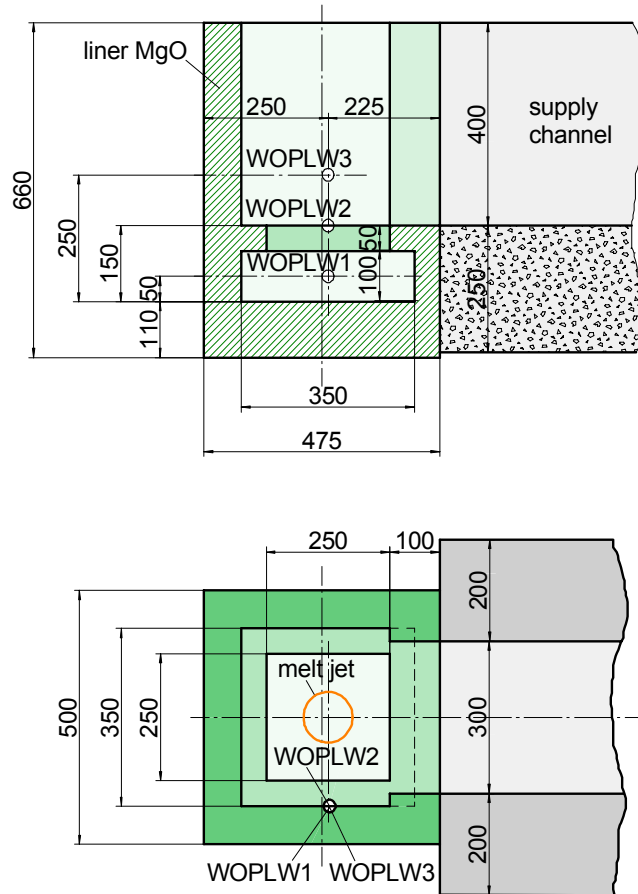
Figure 2-5: Geometry and instrumentation of the whirl basin

2.1.4 Composition of the Concrete

The siliceous concrete of the spreading cavity was fabricated with the following specification:

Material	Mass per m^3
Water	190 kg
Cement CEM III/B 32,5 NWHS	350 kg

SiO$_2$-Aggregates
  (Rheinkies) with:
    Gravel 0 – 2 mm
    Gravel 2 – 8 mm
    Gravel 8 – 16 mm
    Gravel 16 – 32 mm
	1783 kg
	
	35 %
	15 %
	25 %
	25 %

Its density is ρ = 2323 kg /m$^{3.}$

As this composition has only minor deviations from the standard concrete composition of the previous BETA experiments, its decomposition enthalpy can be assumed as
Δ h = 2.1 MJ/kg.

8

2.1.5 Pour of the Melt

Release of the melt took place through a nozzle at the bottom of the thermite crucible. The nozzle had an open diameter of 100 mm to allow for an initial flow rate of about 20 litres/s, see Figure 2-6. The aperture was closed with a steel disc at a closure pin. Opening of the nozzle was done by a lever mechanism that drove the closure pin upwards through the overlaid sand into the thermite melt.

At first, the heavier iron fraction of the melt poured out into the whirl basin underneath the crucible, followed by the lighter oxide melt. After filling the whirl basin to 150 mm, the melt poured into the supply channel and spread onto the spreading area. By the use of the whirl basin no major horizontal momentum was generated.
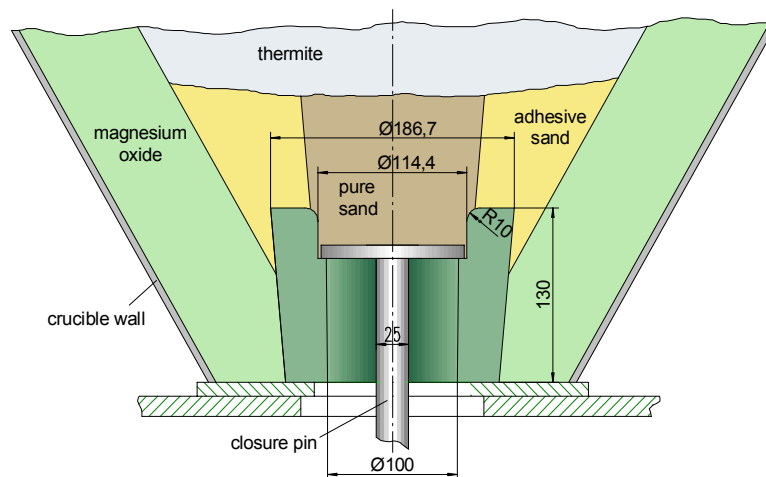
Figure 2-6: Geometry of the nozzle to release the melt

2.1.6 Top Flooding with Coolant Water

To allow top flooding of the melt surface, a water distribution tank was mounted at the opposite wall of the spreading cavity (see Figure 2-7). The tank was 2 m long and covered the wall completely. The water, supplied to the water tank by the water inlet tube, entered the melt surface by overflow over the water-cooled weir, which was located 15 mm beneath the top cover (Figure 2-8). In order to provide a quiet and continuous flow along the weir, the inlet tube, which was located near the bottom of the tank, was equipped with distributed holes. These holes were evenly placed along the tube in distances of 10 cm with quarterly partition in the circumference of the tube as shown in Figure 2-8. A baffle inside the tank provided for a uniform water flow.

For a prompt start of top flooding the tank was totally filled before the test. Top flooding was started by an external activated electro-pneumatic valve, which was calibrated to 4 litres water / s. The water flow was measured with a magnetic inductive flow meter.

During the experiment the tank was closed with a top cover.

Figure 2-7: Water distribution tank of 200 liters mounted at the opposite wall of the cavity
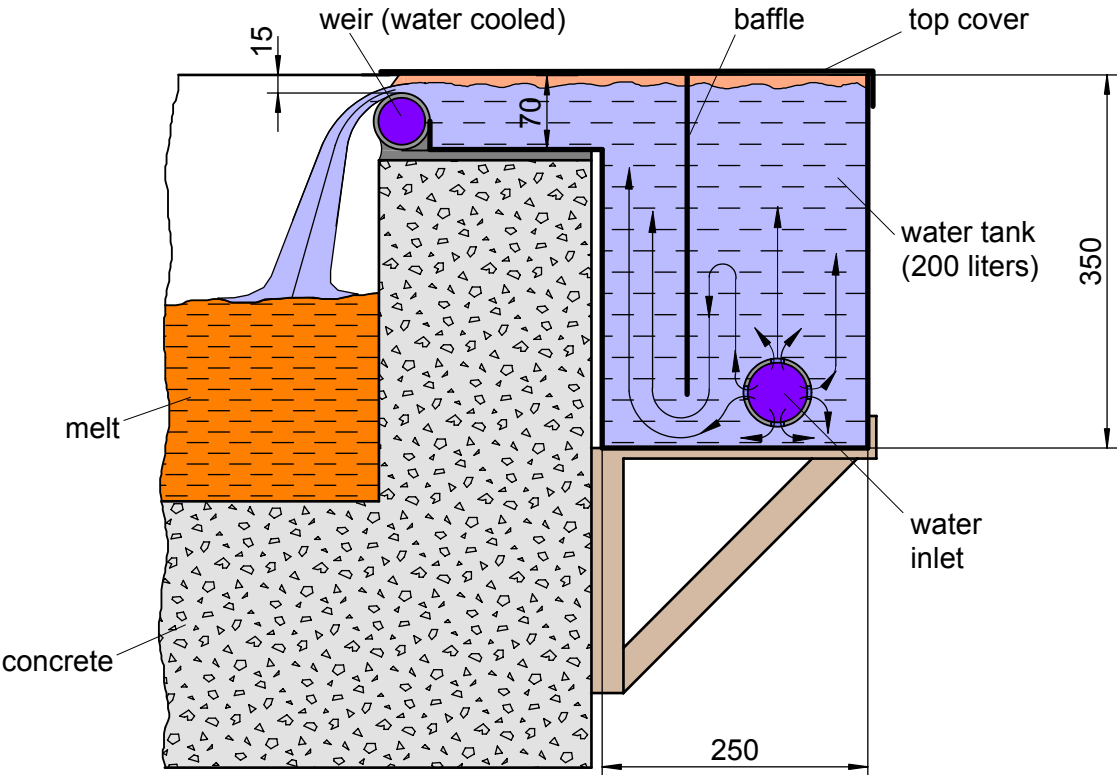
Figure 2-8: Cross section of the water tank with integrated weir for top flooding

2.1.7 Instrumentation

The ECOKATS-2 facility was primarily equipped with load cells, thermocouples, water flow meter, video and infrared cameras. Declarations of the sensor encodings and the sensor locations are given in the instrumentation plan in the Appendix and in Figure 2-2 and Figure 2-9. The cameras and the crucible instrumentation are not shown in Figure 2-9. The origin of the time axis for the recorded data was set to the time point when the electrical start signal for the tapping was recorded.

Mass of Thermite Crucible

As shown in Figure 2-1 and in Figure 2-2, the thermite crucible was positioned on 4 load cells to determine the total mass and the melt release during the experiment. Each load cell had a maximum capacity of 4.7 t with an error less than 0.05% and with the sensitivity of 2.85 mV/V ±0.1 %. The signal of each load cell was given to an electrical summing element, which delivered the analog signal of the total crucible weight. The sum signal was fed to an amplifier, which raised the measured signal to a maximum output value of +10 V.

Because of the measuring range of about 6500 kg for the loaded crucible, the amplifier was configured such that a maximum weight of 8000 kg yielded the maximum output signal of +10 V. The measured load signal of the crucible was defined as LOAD00.

Temperature of the Melt during Pouring and at the Spreading Area

The initial temperature of the melt was measured in the whirl basin with 3 W-Re thermocouples WOPLW1, WOPLW2 and WOPLW3 (W-Re plunging type). The locations of these thermocouples are shown in Figure 2-5.

The temperature measurement of the melt during spreading began at the entrance of the supply channel with the thermocouples NIMAC1 (Ni-CrNi mantle type) and WOPLC1 (W-Re plunging type) as shown in Figure 2-9. At the distance of 1.5 m downstream from the channel entrance, the thermocouple WOPLC2 (W-Re plunging type) was placed. The active junctions of these thermocouples were located 10 mm above the concrete surface.

For the temperature measurement of the spreading melt, the thermocouple modules 1 to 4 were mounted in the bottom of the spreading cavity (Figure 2-9). As shown in Figure 2-10 and Figure 2-11 each module was equipped with a rake of 8 staggered thermocouples NIWImi (Ni-CrNi wire type) to measure the temperature and the penetration depth of the melt in the concrete. The first thermocouple no 1 of the rake was in line with the concrete surface. The following two thermocouples no 2 and 3 were only 2 mm apart whereas the next two thermocouples no 4 and 5 had a distance of 4 mm each. The last three thermocouples no 6 to 8 were placed in distances of 6 mm. With this instrumentation, the uppermost 30 mm of the concrete could be observed. In the rake, the tip of each thermocouple was bent in an angle of 80° to be nearly parallel to the isotherms in the concrete, in order to avoid temperature errors due to the conductivity of the thermocouple itself. The thermocouple WOPLm1 (W-Re plunging type) measured the temperature of the arriving melt, 13.5 mm above the concrete surface.

In addition, the temperature of the environment was measured at several positions with the sensors RTEM01, RTEM02 and RTEM03.
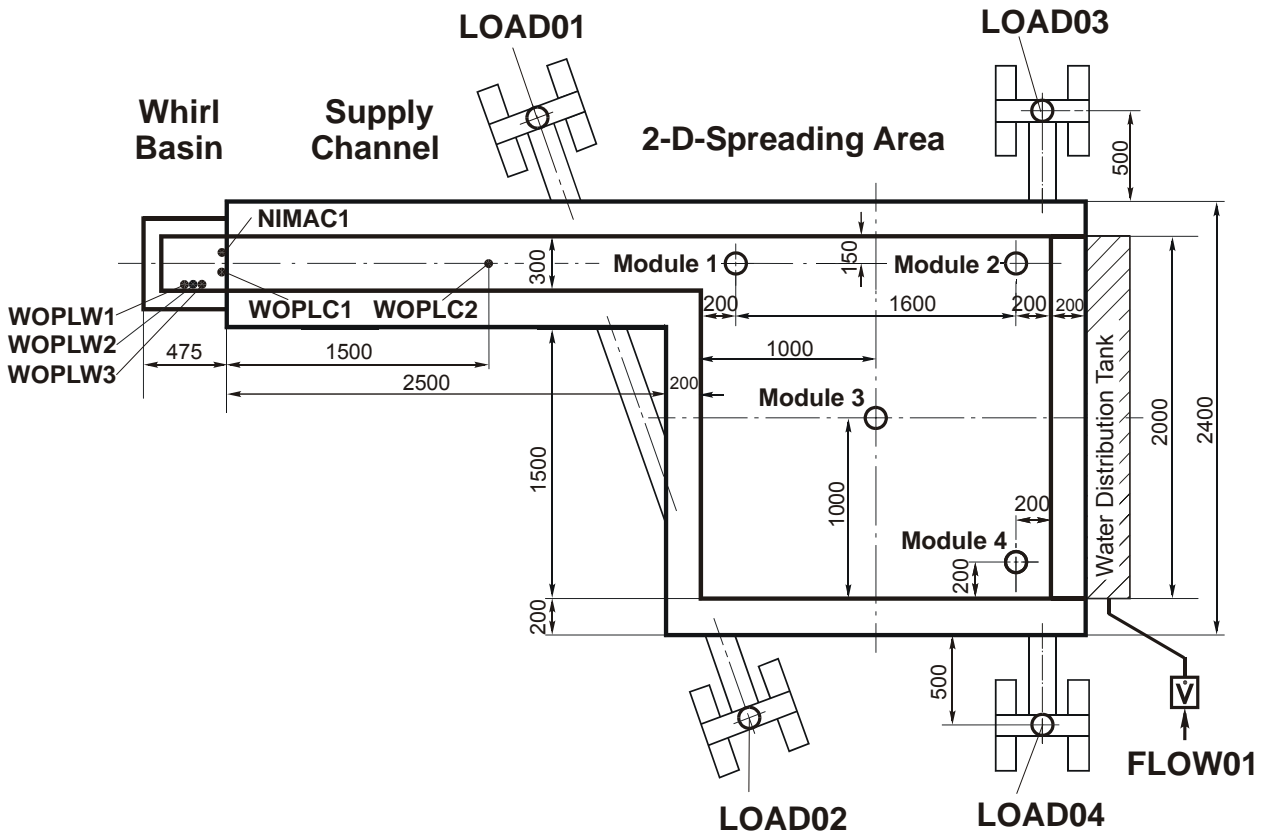
Figure 2-9: Instrumentation of the spreading cavity in ECOKATS-2
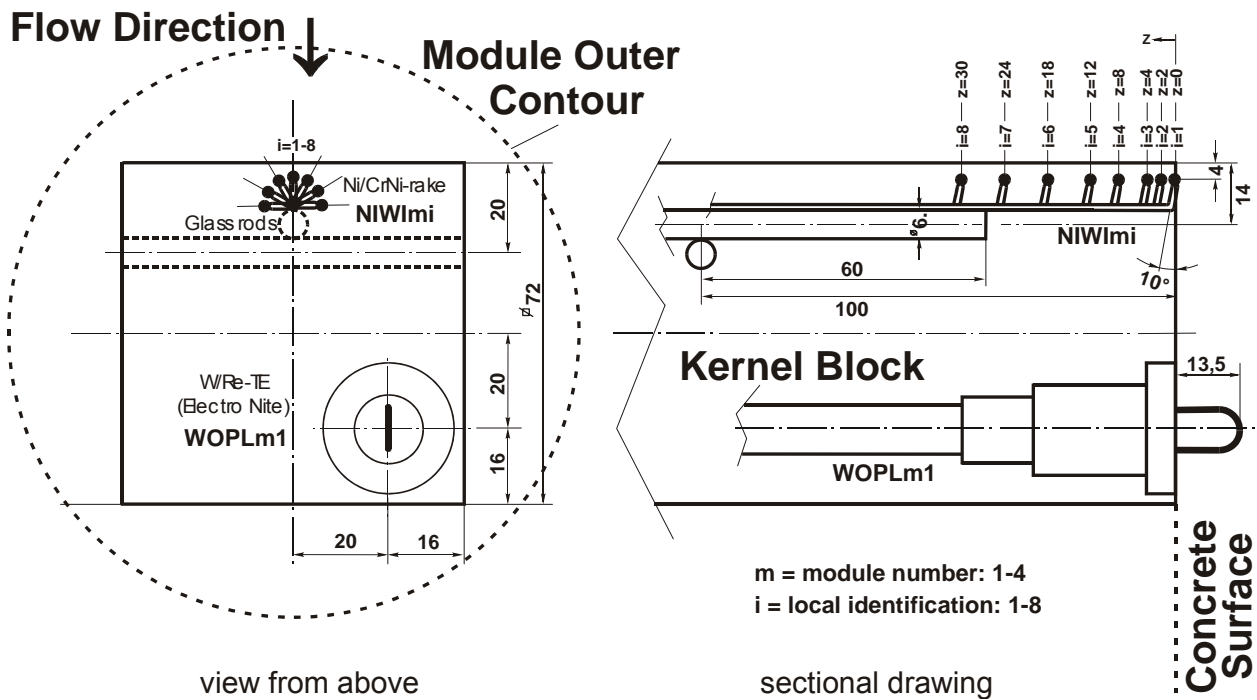
Figure 2-10: Detail of the thermocouple modules used in ECOKATS-2

Total View

Detailed View

Figure 2-11: TC modules: Thermocouples in the mould prior to filling with concrete

Water Flow Rate for Top Flooding of the Melt

For the top flooding of the melt a water tank with integrated weir was mounted at the backside of the spreading cavity, see chapter 2.1.6, Figure 2-7 and Figure 2-8. During the flooding process the water flow rate was measured with a magnetic inductive flow meter with the measuring range of 0 - 5 litres/s. Within its working range, the flow meter provided an analog signal of 0-20 mA defined as FLOW01. For the test ECOKATS-2, a constant water flow of 4 l/s was planned.

Mass of Spreading Cavity during Spreading of the Melt

The steel support of the spreading cavity was made up of a suspension system with 4 support legs as shown in Figure 2-1 and Figure 2-9. The legs were prepared with the load cells LOAD01 – LOAD04 to measure the total weight of the spreading cavity and hence the resultant weight of the supplied melt.

Each load cell had a maximum capacity of 50 kN with an error less than 0,04 % and with the sensitivity of 2 mV/V ±0,1 %. Each load signal was processed by an instrumentation amplifier, which raised the measured signal to a higher output value. Thus the maximum load signal of 50 kN yielded a maximum output signal of +10 V.

2.1.8 Data Acquisition

The data recording has been done by an application program under LabWindows (National Instruments, Version 2.3.1). The implementation provided for a maximum of 128 input channels. For the actual application, about 40 channels were sufficient for all installed sensors. The recording system provided a time base by setting a time stamp to all the measured signals. In addition to the sensor signals, the control voltage to open the outlet nozzle has been registered as time mark for start of the melt pour and simultaneously as start of the experiment.

With the sample frequency of 10 Hz and the maximum recording time of 1 hour, the total capacity of the required memory was some 6 Mbytes.

The instrumentation plan with all implemented sensors is given in the appendix. Three I/O submodules (5001) from Analog Devices with 16 amplifiers on each module were available primarily for processing the signals of the thermocouples. All load cells were prepared with special bridge amplifiers, as mentioned in section 2.1.7.

For the data transfer to the recording PC, four multiplexer units SCXI from National Instruments with 32 input channels per unit were available, from which only 2 multiplexer units were used for the actual experiment.

2.1.9 Camera Observation

Video Camera

For observation of the experiment, 5 conventional colour video cameras with a frame rate of 25 Hz were installed by FZK. Two cameras were behind the crucible: One to monitor the ventilation head of the crucible during the reaction phase and one to observe the mechanism for opening of the release nozzle. Three cameras registered the spreading process: One observed the whole cavity of the test facility from the side; one monitored the melt flow in the supply channel and one registered the melt spreading on the spreading area. The last camera was mounted above the cavity at a vertical distance of 5 m. Figure 2-2 shows the scaffold on which the different video systems were mounted.

Becker Technologies provided one black & white CMOS camera with arbitrary logarithmic characteristic i.e. sensibility versus brightness. Because of the low aperture angle of this camera objective only a section of the supply channel was visible even at the maximum vertical distance of 5 m.

To analyse the movement of the melt during the test, cross signs were painted over the hole spreading area with spacing of 20 cm.

Infrared Camera

From Automation Technology GmbH an infrared (IR) camera was positioned 5 m above the spreading area to register the temperature at the melt surface. The camera was calibrated for the measuring range of 350-1800 °C with an error <±2 %. The actual accuracy is, however, defined by the emissivity of the melt surface, which is known with minor accuracy. Because of the large 60° angle of the objective, the whole spreading area has been monitored from the mounting distance. The camera had a picture ratio of 4:3 with 320 x 240 pixels with a frame rate of 8.333 Hz.

Besides general information on the dynamics of spreading, evaluation of the IR-records should allow an estimation of the characteristic temperatures of the melt.

2.2 Experimental Results and Measured Data (D16)

2.2.1 Test Procedure

The realized experimental process of the ECOKATS-2 experiment is provided in Table 2, with 9 shaded s which characterize 9 periods of water supply for top flooding or of refill. Refill was activated when evaporation had significantly reduced the water layer.

Before start of the experiment, the thermite powder was preheated in the thermite crucible to 100 °C with electrical heater rods for at least 18 hours to give a higher initial temperature of the melt. After completion of all preparations for the test, the thermite powder was ignited 180 s before start of the melt pour.

Table 2: Realized process of the experiment ECOKATS-2. Flooding periods are shaded.

Time	Relative time [s]	Event
10:57:00	-210	data acquisition started and operating
10:57:30	-180	ignition of thermite starts with slow reaction
10:58:15	-135	intense thermite burn with strong aerosol release
10:58:45/50	-105	during thermite burn: parts of the roof above thermite crucible explodes with 2 loud bangs
10:59:50	-40	thermite burn ends, weight of thermite crucible nearly constant
11:00:30	0.0	opening of the thermite crucible as planned, start of melt release with non-uniform outflow
11:00:32	1.9	begin of spreading, melt at the channel edge
11:00:33	3	uniform melt outflow, bright melt jet visible and fast spreading, flames from decomposing concrete more than 1 m high, loud sound from intense MCCI
11:00:34	3.6	melt at TC WOPLC2, 1.5 m in the supply channel
11:00:34	4.3	melt at the end of the supply channel, melt leaves the channel with almost supercritical velocity (Froude-No. > 1) in longitudinal direction
11:00:35	5.4	melt at the opposite wall of the cavity, beginning of transverse spreading
11:00:37	7.1	end of metal pour, oxide comes out
11:00:38	8.1	melt reaches the farthest right sidewall of the cavity
11:01:03	33.2	end of melt outflow, 3200 kg melt released, strong MCCI
11:01:37	67.1	start of cooling water (top flooding), strong MCCI ongoing, upper scaffold structure bending (about - 10 cm)
11:02:00	90	water flow continues, no direct effect on the surface of the melt, small water droplets visible above the melt surface, smooth flooding, no steam explosion
11:02:30	120	noise from boiling of water, surface of the melt still bright
11:03:00	150	intensity of boiling reduced
11:04:20	230	melt surface is still bright, flooding continues
11:05:15	285	Sony Video camera destroyed by high temperatures, melt is still partly red
11:05:45	315	bang from metal?
11:06:00	330	condensing steam flow increased
11:07:53	443	first overflow of water over the crucible wall because of some melt/crust relocation ?
11:08:32	481.8	coolant water flow interrupted, as water level reaches the edge of the crucible

11:11:00	630	water drains from cracks in the concrete crucible
11:11:28	658	water overflow occurs by some melt/crust relocation
11:13:01	750.9	start of 2nd flooding period, water level 4-5 cm below upper edge
11:13:24	774	water overflow by some relocation, surface of the melt on the left side increased?, large flat volcano is visible with significant steam release, water level 4 cm below upper edge
11:14:26	835.8	end of 2nd flooding period, surface of melt is visible because of less steam release (subcooled water)
11:14:40	850	steam release is visible from the vents of various volcanoes
11:16:55	985	minor pop from crucible
11:18:01	1051	start of 3rd flooding period, new volcanoes near the edge of the water supply?
11:18:30	1080	water level 4 cm below upper edge
11:19:15	1125.4	end of 3rd flooding period, water level 1 cm below upper edge, minor boiling
11:20:00	1170	after inspection: water covers melt in flow channel, but no water spills to whirl basin
11:30:03	1772.8	start of 4th flooding, water level was rather low
11:32:01	1890.9	end of 4th flooding, no mayor boiling processes
11:38:55	2304.6	start of 5th flooding, still steam from vents visible
11:40:15	2385.3	end of 5th flooding
11:51:04	3034.1	start of 6th flooding
11:52:12	3102.2	end of 6th flooding
12:02:31	3721	start of 7th flooding
12:03:49	3799	end of 7th flooding
12:12:44	4334	start of 8th flooding
12:14:03	4413	end of 8th flooding
12:43:45	6195	start of 9th flooding
12:45:19	6279	end of 9th flooding

Figure 2-12 is the weight of the thermite crucible, which shows the reaction period of the thermite (from -180 to -45 s) and the start of the melt pour at time zero (definition of t= 0 s). In the last phase of thermite reaction intense burning occurred measured by increasing oscillations of the crucible. These oscillations are characteristic for the thermite burn, which came to an end 135 s after the ignition, as indicated by the end of oscillations of the weighing system. The short remaining time of 45 s until pour was just sufficient for the segregation of the metal and of the oxide phases.

The release of 3200 kg melt (895 kg metal and 2305 kg oxide, respectively) was started at time zero and ended at 33.2 s. Because of the relatively wide nozzle, the melt outflow period was very short.

Figure 2-13 gives a more detailed view of the weight of the thermite crucible during melt release indicating the very smooth signal. Two different slopes characterize the weight reduction: The steeper slope is related to the release of the heavier metal, and reduces to a more moderate slope at t=7.1 s, when the melt changed from metal to the lighter oxide. From video recording it was observed that the outflow of the melt began at 1.2 s with some irregularities lasting until 3.6 s, visible in Figure 2-13. Probably an obstacle from the closure mechanism in the nozzle of the crucible caused this behaviour.

16

From the weight curve the equivalent mass flow (pouring rate) into the whirl basin was derived. Due to the discontinuities of the melt outflow at the beginning the curve was useful for determining the start of spreading at 1.9 s (i.e. start of outflow to the supply channel) which was not clearly visible in the video record. The curve characterizes the whole spreading period until its end at 33.2 s.
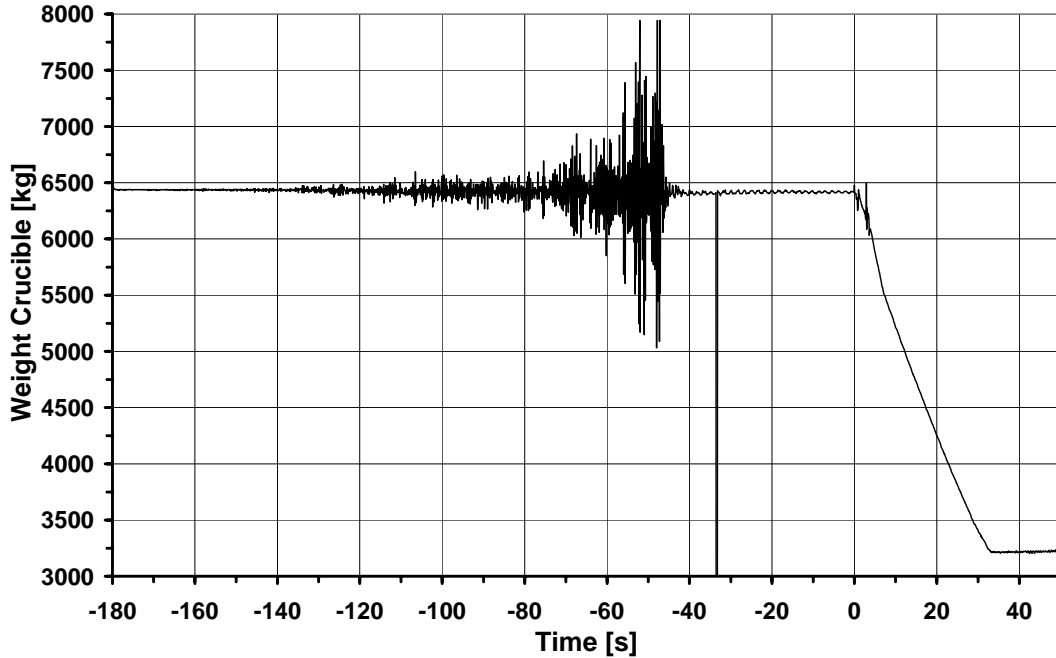
Figure 2-12: Weight of thermite crucible during thermite burn and melt release
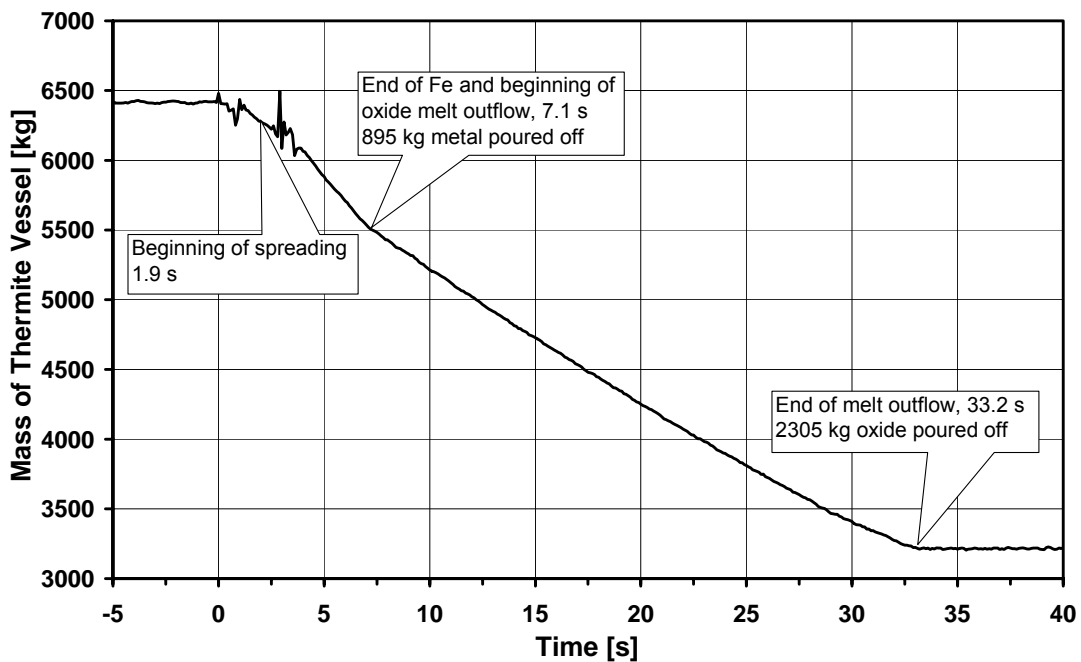
Figure 2-13: Mass of thermite crucible during outflow of the melt

Table 3 gives the time intervals, for which a stepwise constant mass flow rate was determined to be used for code calculations. With the density of 6771 kg/m³ for the metal and 3263 kg/m³ for the oxide at 1830 °C, the volume flow was calculated and is included in the table. The initial volume flow started with 22.6 litres/s and reached the maximum value of 30.6 litres/s at the beginning of the oxide outflow.

After complete spreading the height of the melt (without void) in the cavity should reach some 17 cm, whereof the metal fraction should have a part of about 2.7 cm.

Table 3: Stepwise const. outflow of the melt in ECOKATS-2

Time interval [s]	Mass flow [kg/s]	Volume flow [liters/s]	Event
0	0	0	Opening of the nozzle
1.2 – 1.9	153.3	22.6	Metal outflow
1.9 – 3.9	107.5	15.9	Metal outflow
3.9 - 7.1	178.1	16.3	Metal outflow
7.1 - 17	99.7	30.6	Oxide outflow
17 - 27	89.4	27.4	Oxide outflow
27 – 33.2	68.4	21.0	Oxide outflow
33.2	0	0	End of melt outflow

The mass of the melt which arrived at the spreading area was registered by weighing the whole spreading cavity including the attached whirl basin. Figure 2-14 shows the history of the registered weight during the experiment with inevitable unsteady loadings due to the melt concrete interaction. For the interpretation of the measurement the smoothing of the curve was necessary as shown in Figure 2-14.

With both weight curves Figure 2-13 and Figure 2-14 the mass balance of the spread melt could be analyzed and were found to be in excellent agreement.
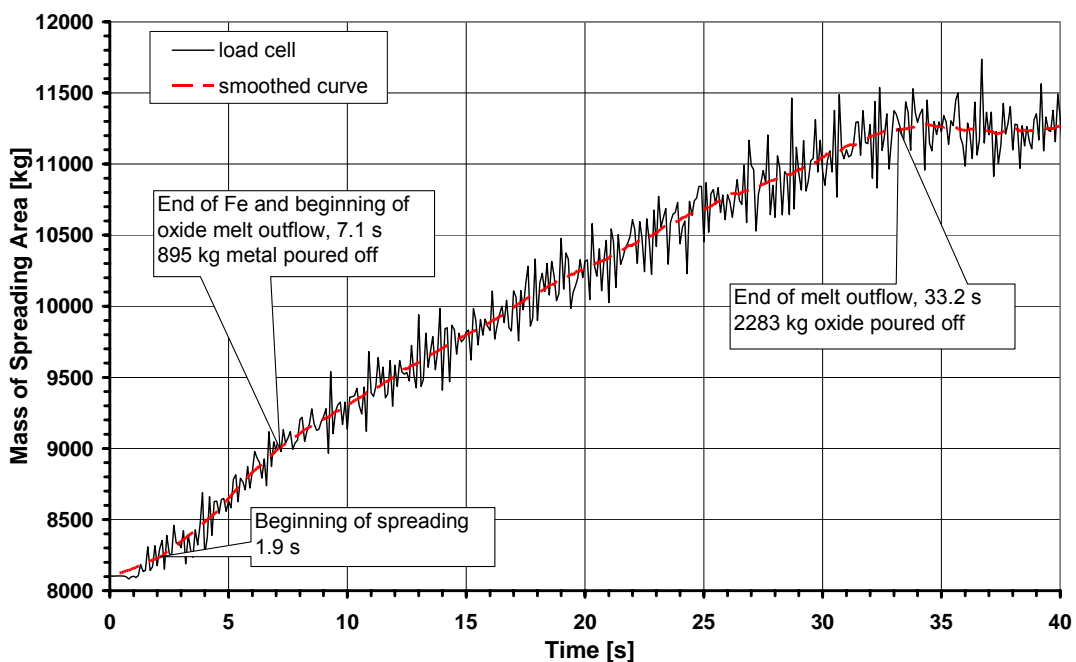
Figure 2-14: Mass of spreading cavity during outflow of the melt

The resulting masses for the experiment ECOKATS-2 are given in Table 4 together with other characteristics of the melt during spreading. The difference of the released and received measured melt mass is 12 kg, which corresponds to a deviation of 0.4 % only. The total melt mass is therefore known with high accuracy.

The mass loss, however, as the difference of two large numbers, has a significant error, which is due to (1) the error of the load cells and (2) the statistical error due to the oscillations by melt agitation. Further on, inevitable mass losses are due to some loss of splashed melt, and the evaporation of water from the concrete. The "missing" 12 kg can therefore be considered only as a rough estimate for these mass losses.

Table 4: Characteristics of the melt during spreading in ECOKATS-2

Parameter	provided in the crucible	outflow from crucible	received at spreading area
total mass of mixed thermite	3200 kg	3200 kg	3188 kg [2]
preheating of thermite mixture	100°C		
metal fraction	895 kg [1]	895 kg	895 kg
oxide fraction	2305 kg [1]	2305 kg	2293 kg
initial temperature of melt	1830°C [3]	1830°C [3]	1830°C [3]
initial rate of melt outflow		22.6 liters/s	22.6 liters/s
maximum rate of melt outflow		30.6 liters/s	30.6 liters/s
duration of metal release		7.1 s	7.1 s
duration of oxide release		26.1 s	26.1 s
total duration of melt release		33.2 s	33.2 s

[1] calculated from previous experiments with the same thermite mixture
[2] the missing12 kg are due to measurement errors, mass losses by melt splashing, and evaporation of water from the concrete
[3] TC measurement in the whirl basin

2.2.2 Spreading Behaviour of the Melt

The most important observations during melt release, spreading, and top flooding are given in Table 2. Different states of the experiment ECOKATS-2 are shown in Figure 2-15. The melt overheat and melt release rate were sufficiently high for a complete and rapid spreading of the melt. Time 0 was defined by the start of melt release through the nozzle of 100 mm diameter in the bottom of the thermite crucible. The pouring rate which was measured by the weight loss of the crucible is given in Table 3. Until 7.1 s 895 kg iron melt was released followed by 2305 kg oxide melt. Overflow of the whirl basin occurred at 1.9 s, which defined the entrance of the melt to the 1-d flow channel and subsequently to the spreading area. Melt release ended at 33.2 s, and the melt evenly filled the spreading cavity. Top flooding was started at 67 s, that was 33.8 s after end of spreading.

The first picture a) in Figure 2-15 shows the spreading test at 30 s, which is near the end of the melt release. Intense melt/concrete interaction occurred with high gas release, substantial melt agitation, and ejection of melt droplets. These phenomena are typical for melt/concrete interaction, and were observed from onset of spreading until the first minutes after completion of spreading. Intense flames about one meter high were visible above the melt surface, which were the result of hydrogen produced by steam release from concrete erosion and its subsequent chemical reduction by the iron melt fraction.

Controlled top flooding with water started at 67 s with a flooding rate of 4.13 litres/s. Flooding was very mild and did not produce energetic interactions of melt and water, or any type of steam explosion. When the hydrogen flames had ceased, small water droplets were visible above the flooded melt surface, shown in picture b). These fine droplets are generated by the intensely boiling water overlayer and are visible up to some 30 cm above the surface. The sound from MCCI changed into noise from boiling water. At least part of the surface was still bright at about 270 s, shown in picture c). At 443 s an sudden overflow of water over the crucible wall occurred because of some relocation of melt or crust. The top flooding was interrupted first time at 482 s as the coolant water level reached the upper edge of the concrete crucible.

a) Spreading at 30 s
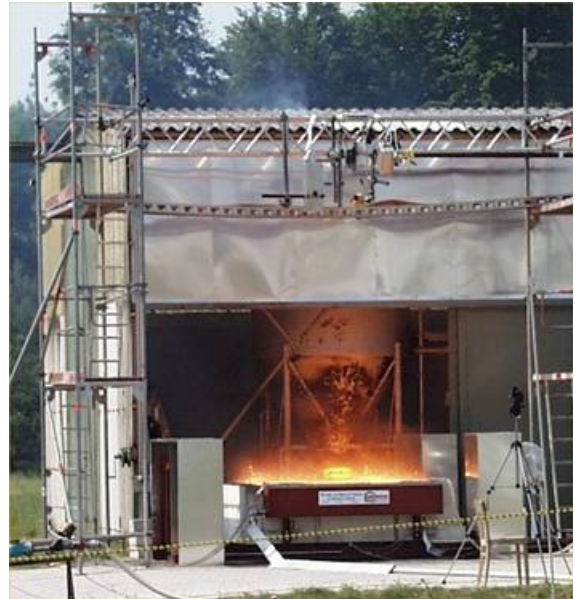
b) At 150 s or 83 s after flooding

c) At 270 s or 203 s after flooding
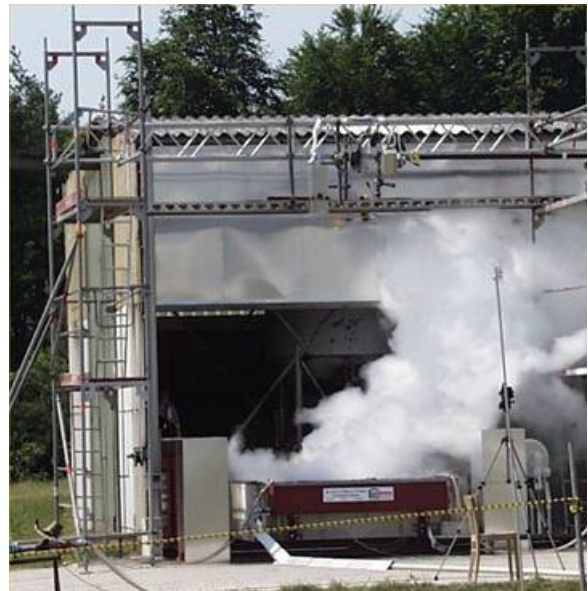
d) At 700 s or 633 s after flooding

Figure 2-15: Different states of ECOKATS-2 during spreading and top flooding

Figure 2-16 shows successively the spreading of the melt with pictures from the infrared camera. In these pictures the spreading area and the supply channel are marked with white lines. Unfortunately, the right concrete wall of the supply channel inhibited the total view into the channel. After the whirl basin was filled with the metallic melt, the melt began to spread along the channel 1.9 s after opening of the thermite crucible. Each picture is labelled with the time referring to the start of spreading and with the absolute time in brackets, which starts with the opening of the thermite crucible. The oxide melt entered the channel after the metallic melt at 5.2 s [7.1 s] (see Figure 2-13).

As shown in Fig. a) the melt reached the end of the supply channel at 2.4 s. The melt front velocity at the end of the channel was 1.7 m/s. The almost 1d supercritical flow (Froude number>1) reached the opposite wall at 3.5 s (see Fig. b). At 3.8 s, a new melt front was observed on the large spreading area, which propagated in circular form from the end of the supply channel over the indicated sector of approx. 45° (Fig. d-f).

The right cavity wall was reached at 6.1 s. Beginning from 7.1 s a relatively long time of 3.9 s elapsed to fill the adjacent edge at the right wall with melt. This area of about 0.28 m² is marked in the Fig. g) and h).

At 11.0 s the whole spreading area was completely covered by the melt. From the video recording it was observed that during further melt inflow, one large vortex developed on the spreading area rotating in the clockwise direction.

a) 2.4 s [4.3 s]

b) 3.5 s [5.4 s]

c) 3.8 s [5.7 s] beginning of 2d spreading

d) 4.3 s [6.2 s]
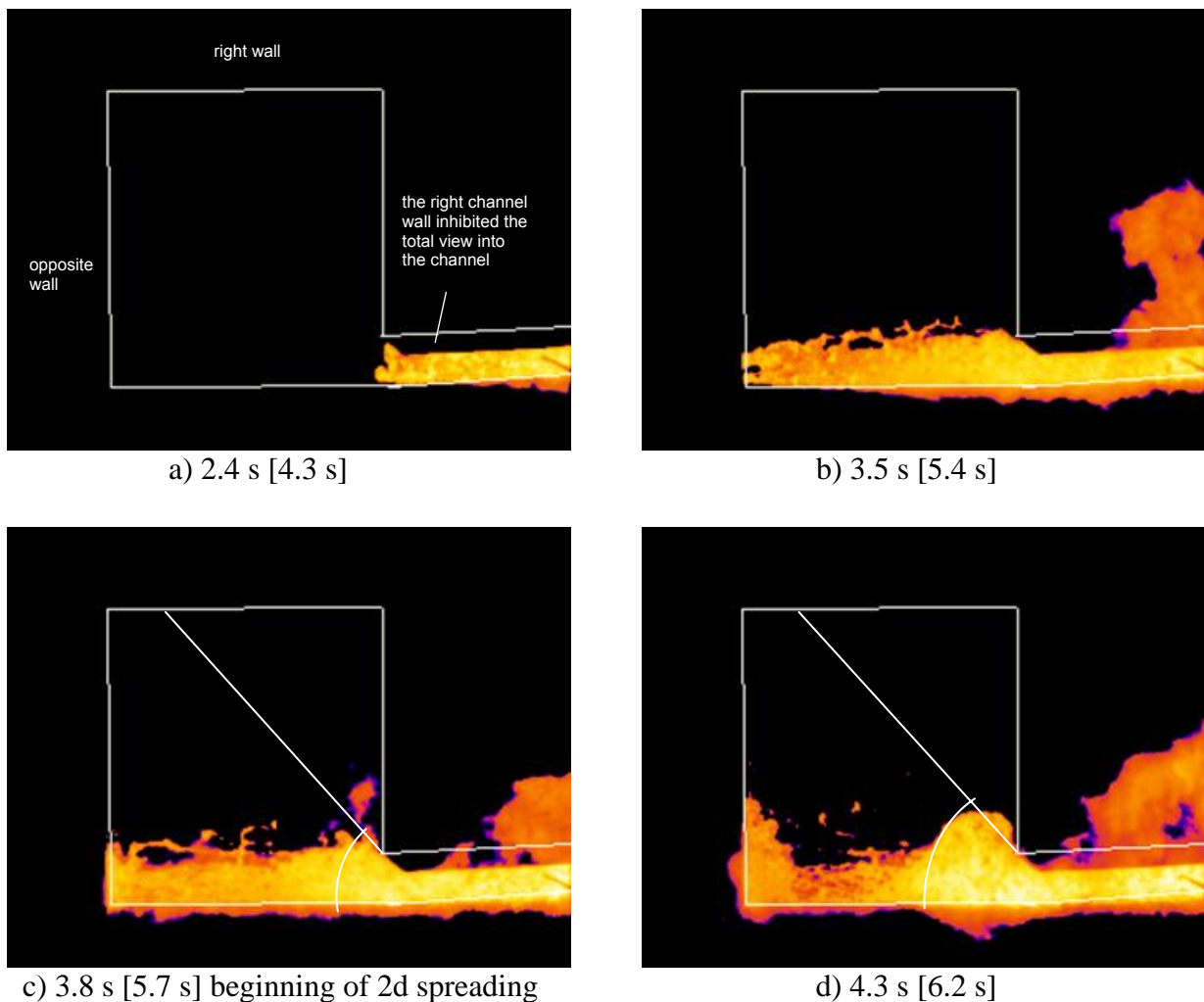
Fig 2-16: (a-d) Spreading of the melt in ECOKATS-2 from infrared measurement
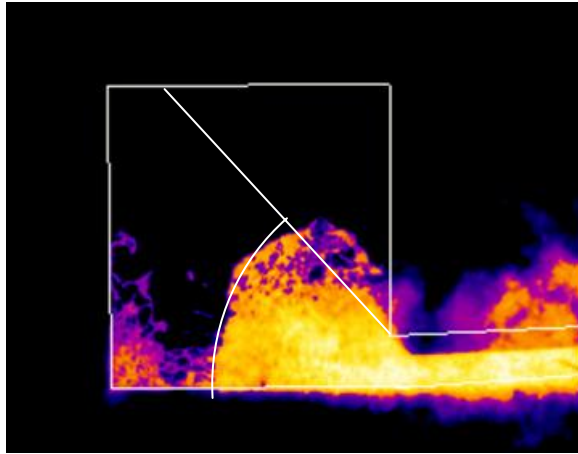
e) 4.9 s [6.8 s]
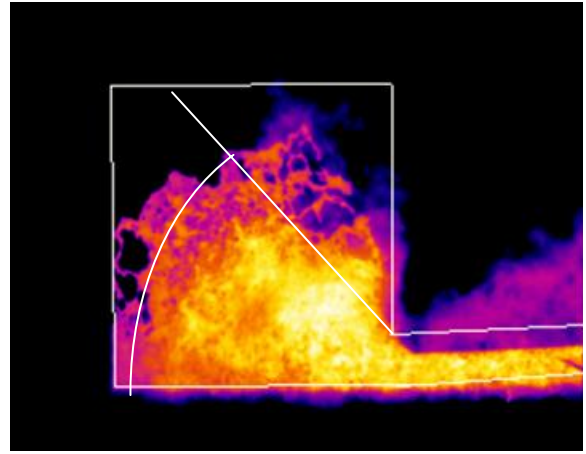
f) 5.5 s [7.4 s]
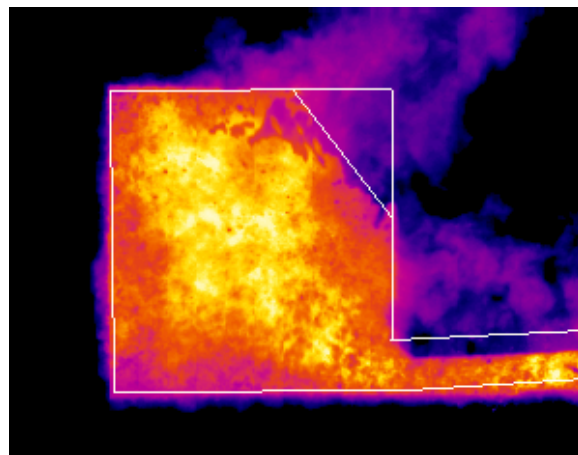
g) 7.1 s [9.0 s]
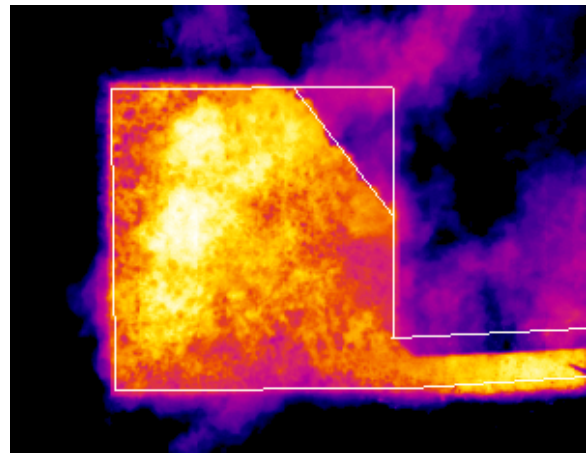
h) 8.94 s [10.84 s]
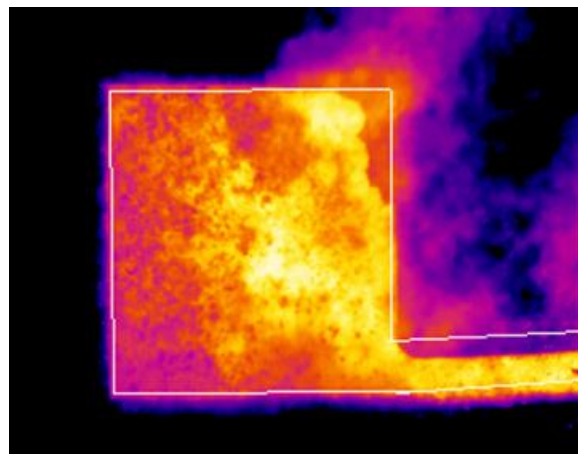
i) 9.77 s [11.67 s]
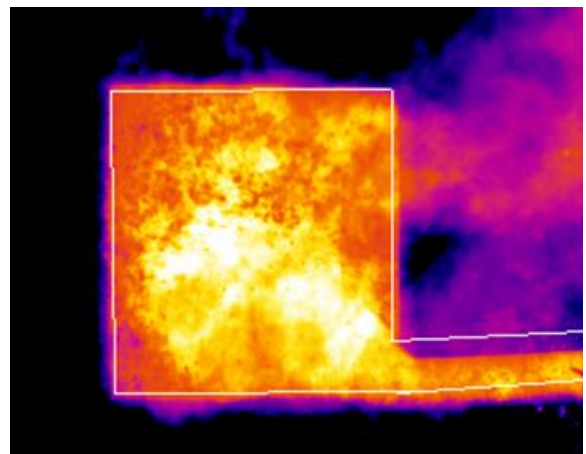
k) 10.97 s [12.87 s]

Figure 2-16: (e-k) Spreading of the melt in ECOKATS-2 from infrared measurement

Figure 2-17 shows a comparison of the experimental analysed melt front position with an approximate gravity-inertia solution for a channel geometry [9]. The melt front could be clearly identified at 0.5 m in the channel. Up to 1.3 s the theoretical curve is in good agreement with the experimental results. For t>1.3 s the approximate solution underestimates the measured front position considerably due to the supercritical character of the actual flow.

The estimated position of the second circular-symmetric melt front measured from the end of the channel (see c – f in Figure 2-16) as a function of time is in good agreement with predictions of an approximate gravity-inertia solution for sector geometry (Figure 2-18).
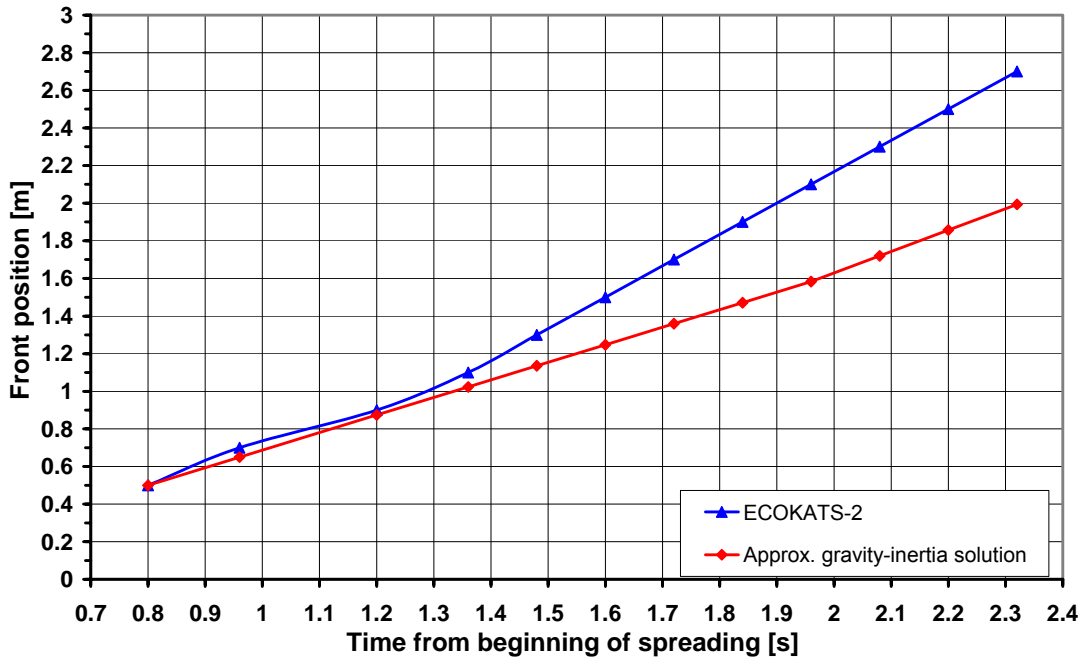
Figure 2-17: Evolution of the melt front in the supply channel
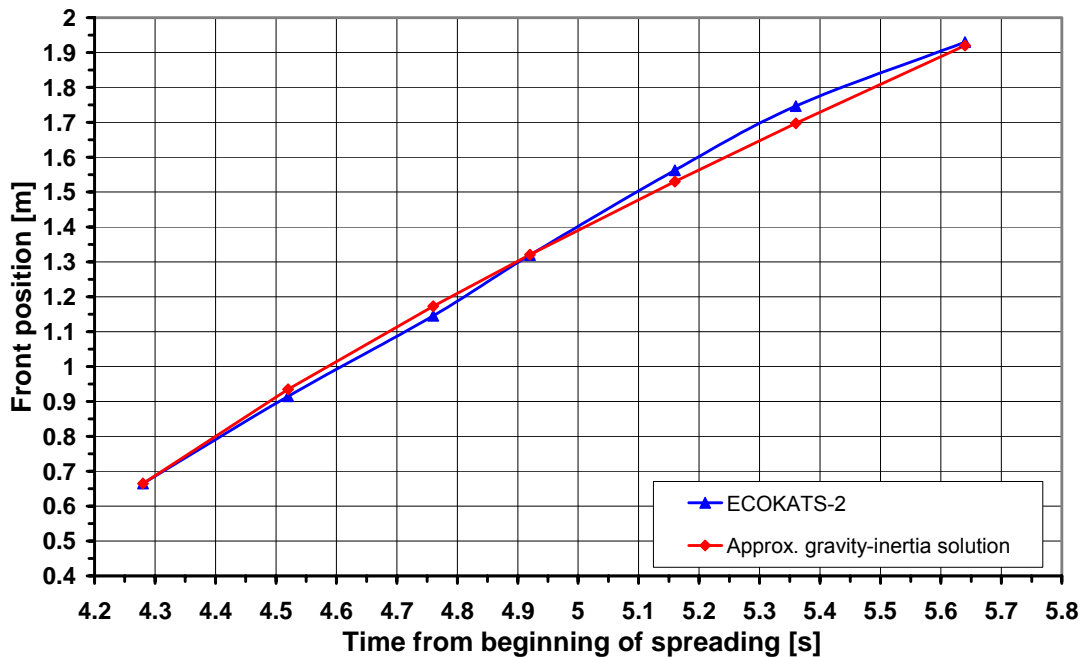
Figure 2-18: Evolution of the melt front on the large spreading area

2.2.3 Measured Temperatures

2.2.3.1 Temperature of the Melt in the Whirl Basin

To measure the temperature of the melt at the start of spreading, three W-Re thermocouples WOPLW1 to -3 were installed in the whirl basin at elevations of 50 mm, 150 mm and 250 mm above the bottom (Figure 2-5). The measured temperatures are shown in Figure 2-19. Due to the high mass flow the response time for the direct melt contact at the tip of the elements was very short and a radiation-dominated heat transfer period didn't appear. The measurement overview verifies that all signals are plausible in the time period to 17 s, and give a temperature range between 1790 °C and 1900 °C. The thermocouple WOPLW1 measures the temperature in the metal layer 50 mm above the bottom of the whirl basin. As measurements in the metal layer have a higher accuracy than in the oxide layer atop, this measurement was selected as the most probable initial temperature of the melt, which is 1830 °C with the standard deviation of $\pm 40°C$.
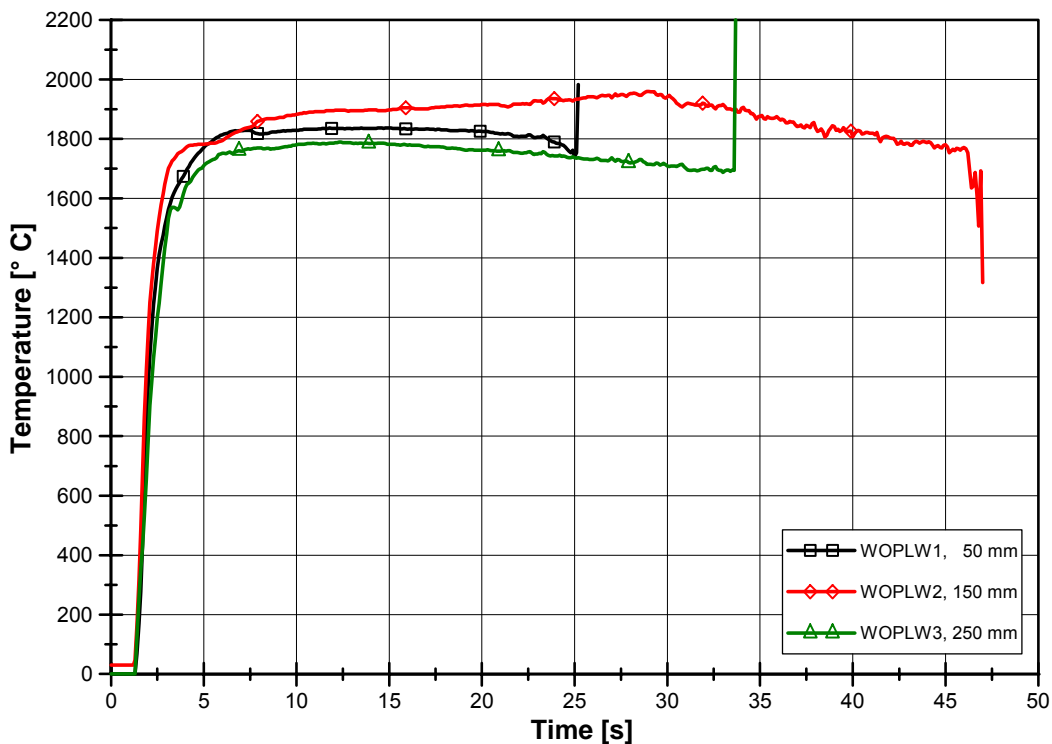
Figure 2-19: Temperature of the melt in the whirl basin

2.2.3.2 Temperature of the Melt in the Supply Channel

The temperatures of the melt at the entrance of the supply channel and 1.5 m from the entrance were measured with the thermocouples WOPLC1, NIMAC1, and WOPLC2 as illustrated in Figure 2-9. All these thermocouples were placed 10 mm above the concrete surface. The corresponding measurement signals with the associated arrival time of the melt are shown in Figure 2-20.

The thermocouples at the beginning of the channel failed very soon. Thermocouple NIMAC1 was primarily implemented to identify the arrival time of the melt at the entrance of the supply channel. Unfortunately, because of the discontinuity of the melt

outflow, NIMAC1 measured a melt splash somewhat earlier than the beginning of spreading. WOPLC1 indicated shortly a realistic temperature of 1840 °C. The thermocouple WOPLC2, 1.5 m downstream, measured somewhat longer and reached finally 1740 °C, when it failed. One can assume if this element had measured any longer it would have reached about 1800 °C. These measurements confirm the initial temperature of the melt at 1830 °C.

In Figure 2-20 additionally the signals of the thermocouples NIWI11 and WOPL11 are given. Both sensors were imbedded in thermocouple module1 which was 0.2 m behind the channel end at position 2.9 m. NIWI11 (Ni-CrNi, flush with the concrete surface) measured faster and a higher value than WOPL11 (W-Re) which was protruding 13.5 mm into the melt. The higher value of 1300 °C from NIWI11 is identical with the melt temperature of concrete and seems to be correct. The temperature of WOPL11 is unphysical as the measured temperature in the melt is lower than at the concrete surface.

With the volume flow in Table 3 the height of the melt could be determined. Consequential at position 1.5 m the melt reached 45 mm and increased to 58 mm at 2.9 m.
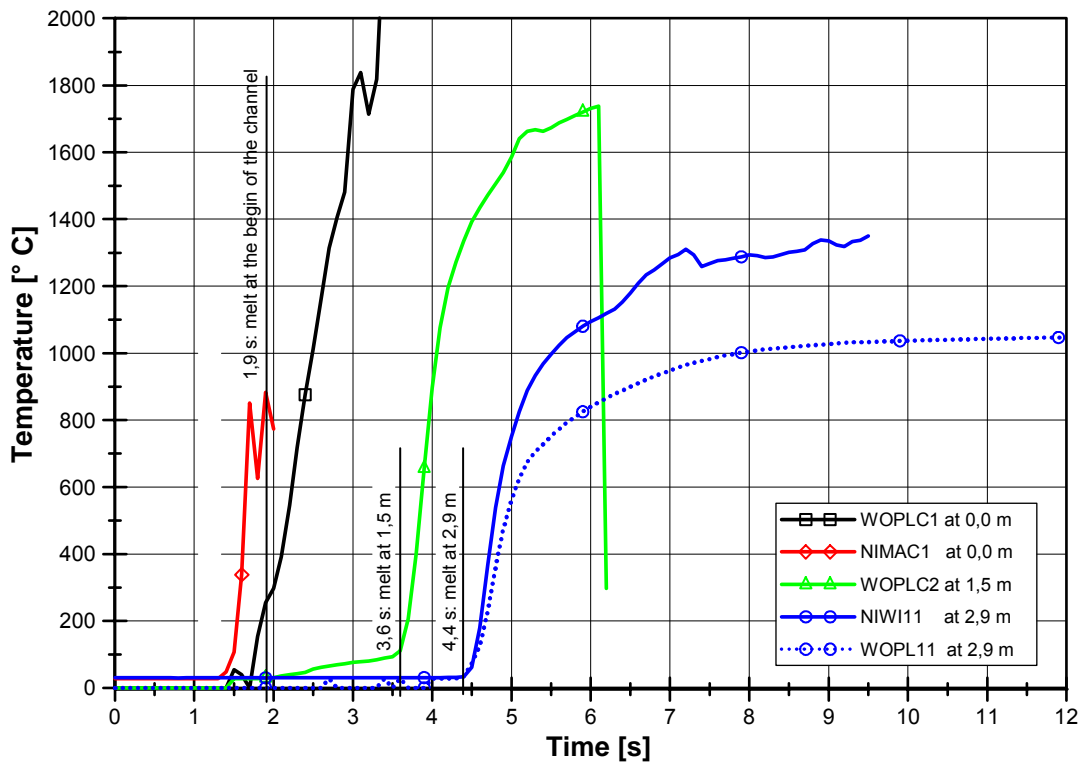
Figure 2-20: Temperature of the melt measured in the supply channel and nearby

2.2.3.3 Temperatures of the Melt on the Spreading Area

To measure the temperature of the melt on the large concrete area and the temperature distribution in the upper concrete layer, four thermocouple modules of concrete with several types of thermocouples were implemented in the concrete (Figure 2-9 and Figure 2-10).

To determine the melt temperature on the concrete surface those thermocouples are useful that were located flush with or slightly above the concrete surface. These are the thermocouples NIWIm1 of Ni-CrNi-type (at 0 mm) and the thermocouples WOPLm1 of W-Re–type (protruding +13.5 mm). Under ideal conditions, they would register the temperature in the bottom boundary layer of the spreading melt which is lower than the bulk temperature. Figure 2-21 shows the corresponding measurement signals at all four thermocouple modules over time. The signals of Ni-CrNi-thermocouples seem to be correct, because they measured the melt temperature of concrete which is about 1300 °C, indicated by a maximum or by a plateau. Shortly after the measurement they failed. With the exception of thermocouple WOPL21 the thermocouples of W-Re –type measured a too low and unphysical temperature, as it is below the temperature at the spreading area. Possibly the heat transfer through the glass protection tube around the sensor tip or a growing melt crust influenced the measured temperature, so that it may not represent the actual temperature of the melt. Only thermocouple WOPL21 measured a plausible value of 1630 °C at 40 s which is probably the right temperature of the melt in the layer at 13.5 mm.
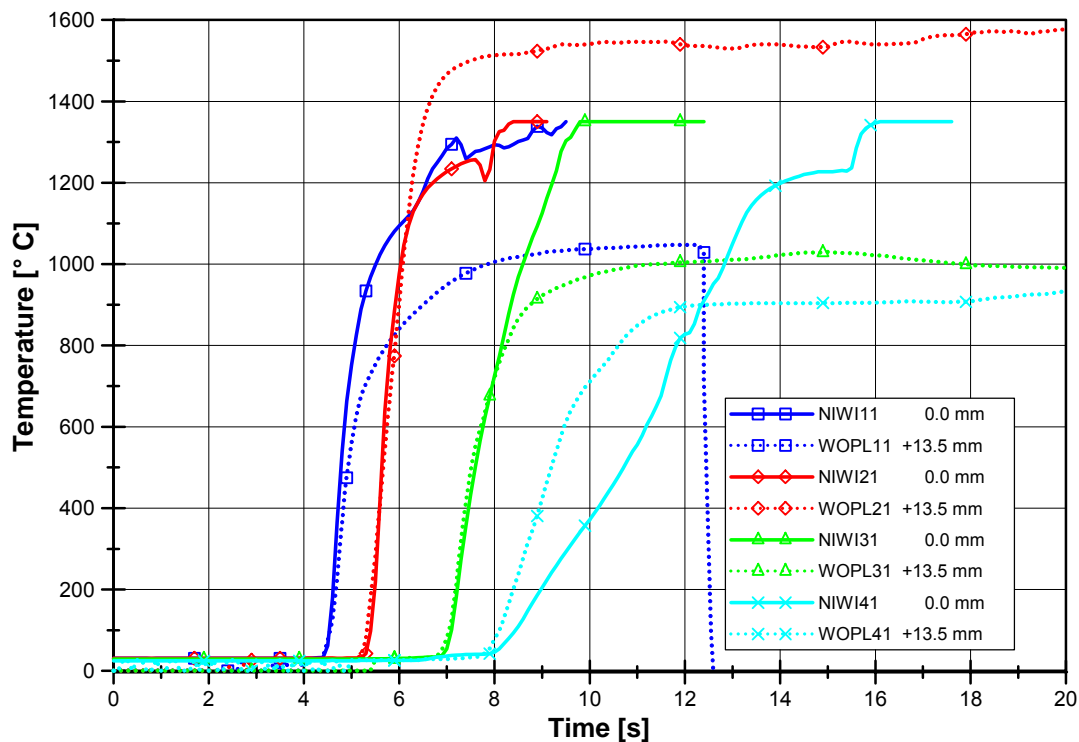
Figure 2-21: Temperature of the melt measured at the thermocouple modules

The temperatures measured by thermocouples can be compared with the temperatures of the melt surface measured with the infrared camera. The maximum temperature values were taken at a small region at the end of the supply channel (sign IR-A1) and at the entire spreading area (sign IR-A2) over a time period of about 50 s. Figure 2-22 presents the results of this evaluation together with thermocouple measurements in the

whirl basin and at the thermocouple modules 2, 3 and 4, already described above. The comparison shows a plausible decrease of the surface temperature of the melt along the spreading path from 1830 °C to 1550 °C and confirms the correctness of thermocouple WOPL21. Simultaneously it indicates that the thermocouples WOPL31 and WOPL41 protruding from the concrete surface didn't measure the temperature of the melt correctly.

It is important to keep in mind that the evaluated surface temperature from the IR video records is, however, lower than the bulk temperature of the melt.
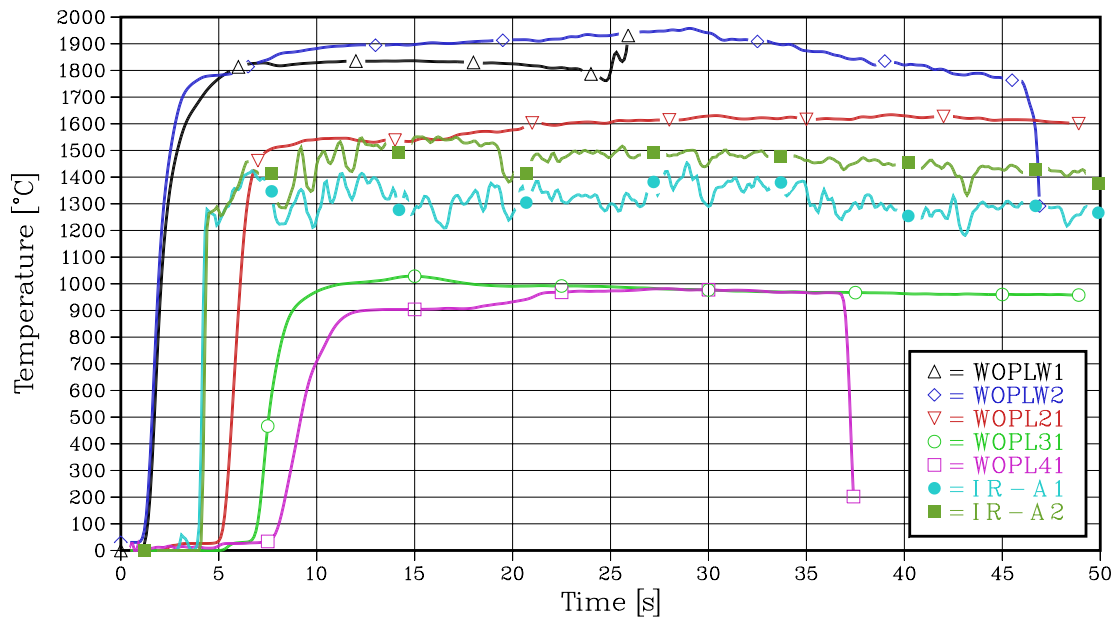
Figure 2-22: Comparison of measurements with thermocouples and with IR technique

2.2.3.4 Temperature Distribution in the Concrete Substrate

The Ni-CrNi thermocouples NIWImi embedded in the concrete of the thermocouple modules were arranged in a staggered, uniformly spaced manner with increasing distances in depth as shown in Figure 2-10. They provided a spatial and temporal distribution of the temperature in the concrete for all 4 modules over a time period of 250 s which is given from Figure 2-23 to Figure 2-26. The thermocouples NIWIm1 were placed flush with the concrete surface whereas the thermocouples WOPLm1 were protruding 13.5 mm into the melt. As shown in the diagrams the thermocouples WOPLm1 of W-Re–type measured generally too low temperatures with exception of thermocouple WOPL21 which was correct. Further on, the thermocouples at and below the initial concrete surface failed successively as expected because of arrival of the erosion front. This behaviour was used to investigate the erosion depth in the concrete which is presented in chapter 3.1.3. The thermocouples that remained intact gave reliable results and showed typical temperature histories based on transient heat conduction. Beside the time delay due to the higher distance from the concrete surface, the curves show by flattening at about 110 °C the influence of the evaporation of water that was present in the pores of the concrete.
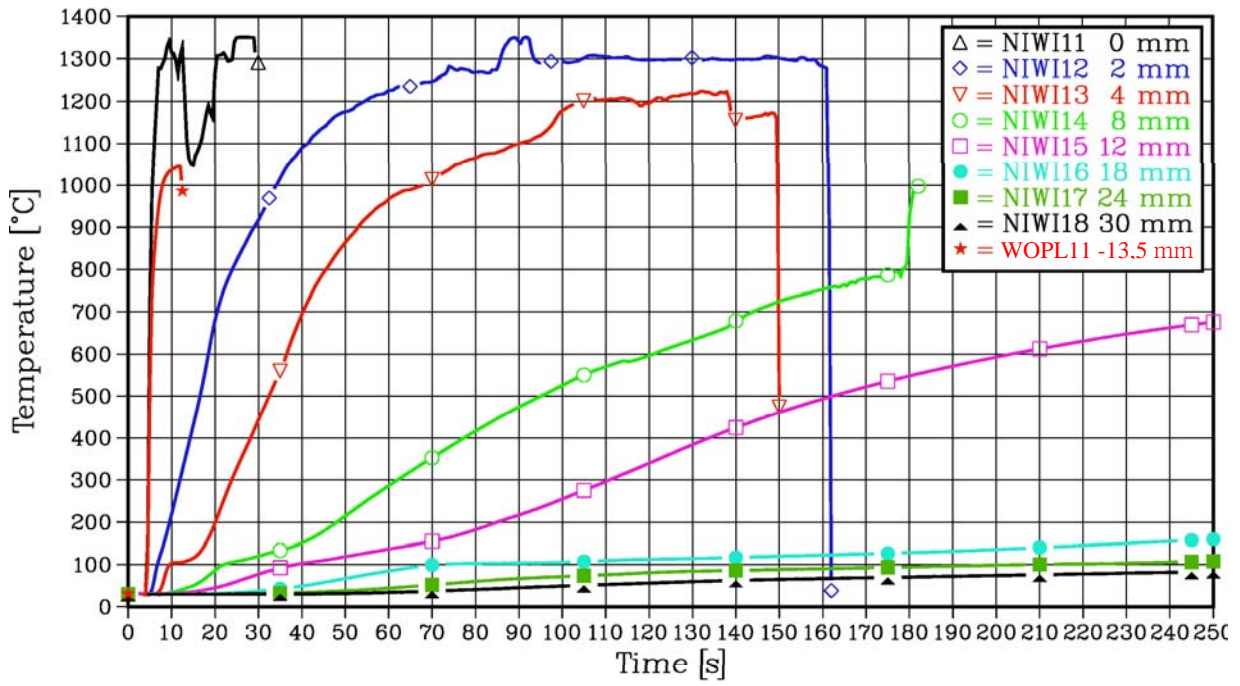
Figure 2-23: Temperature distribution at thermocouple module 1
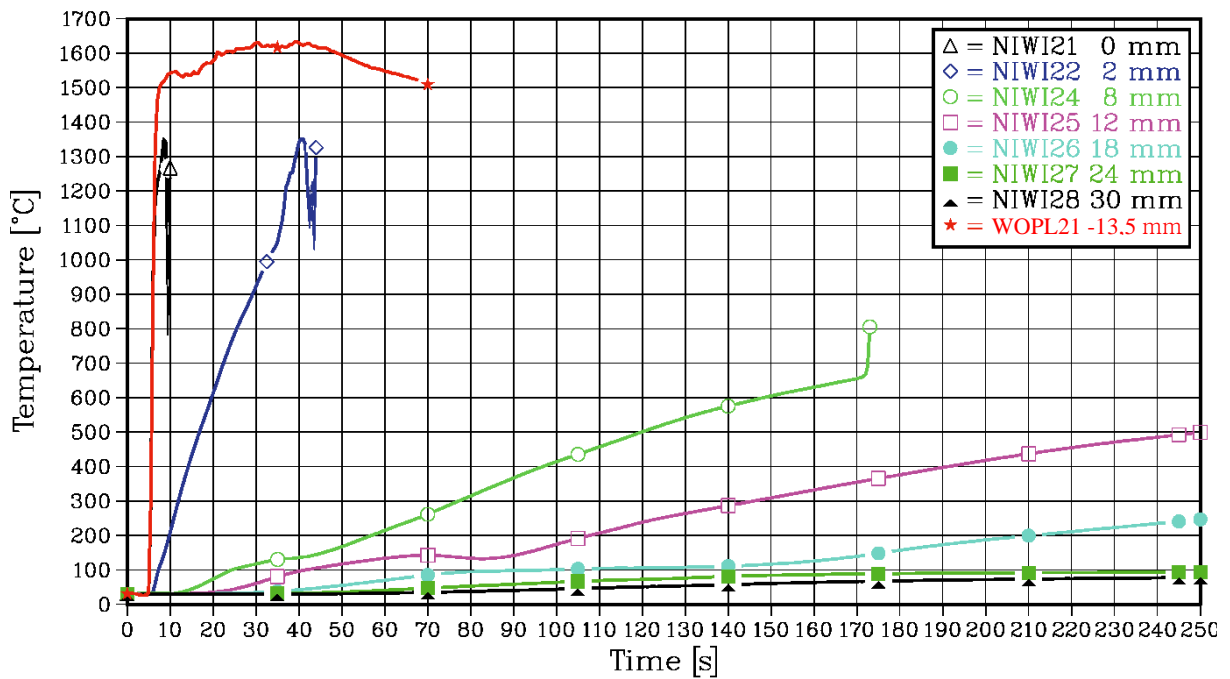
Figure 2-24: Temperature distribution at thermocouple module 2

28
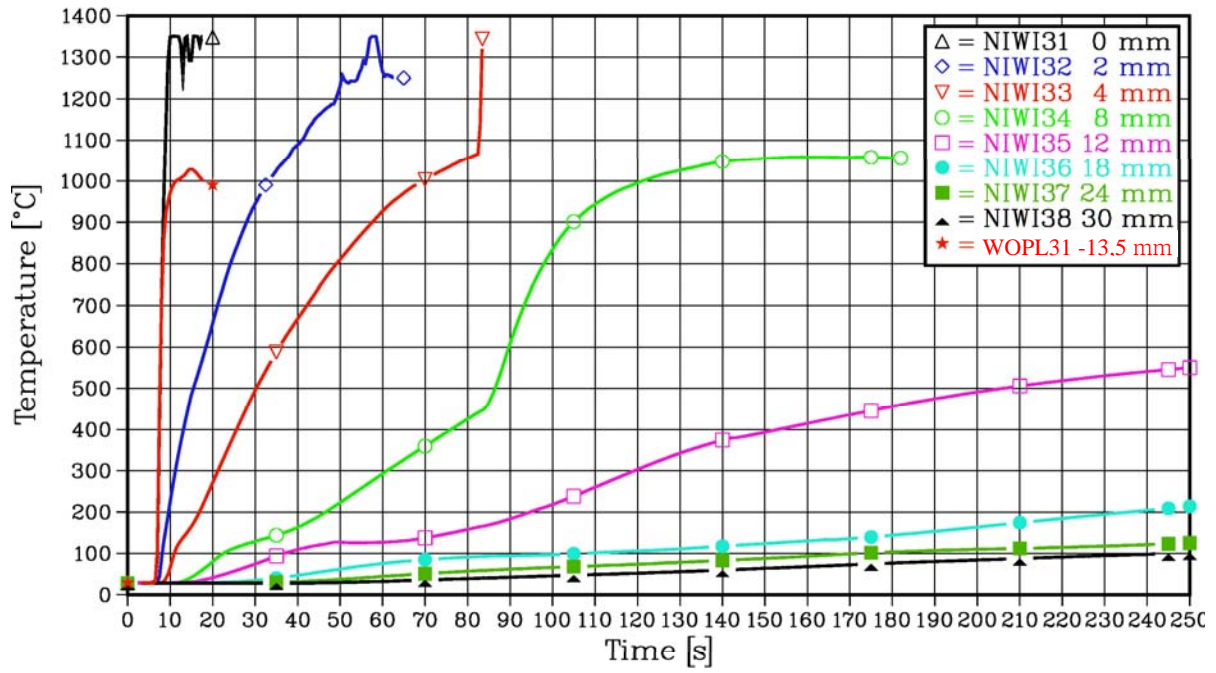
Figure 2-25: Temperature distribution at thermocouple module 3
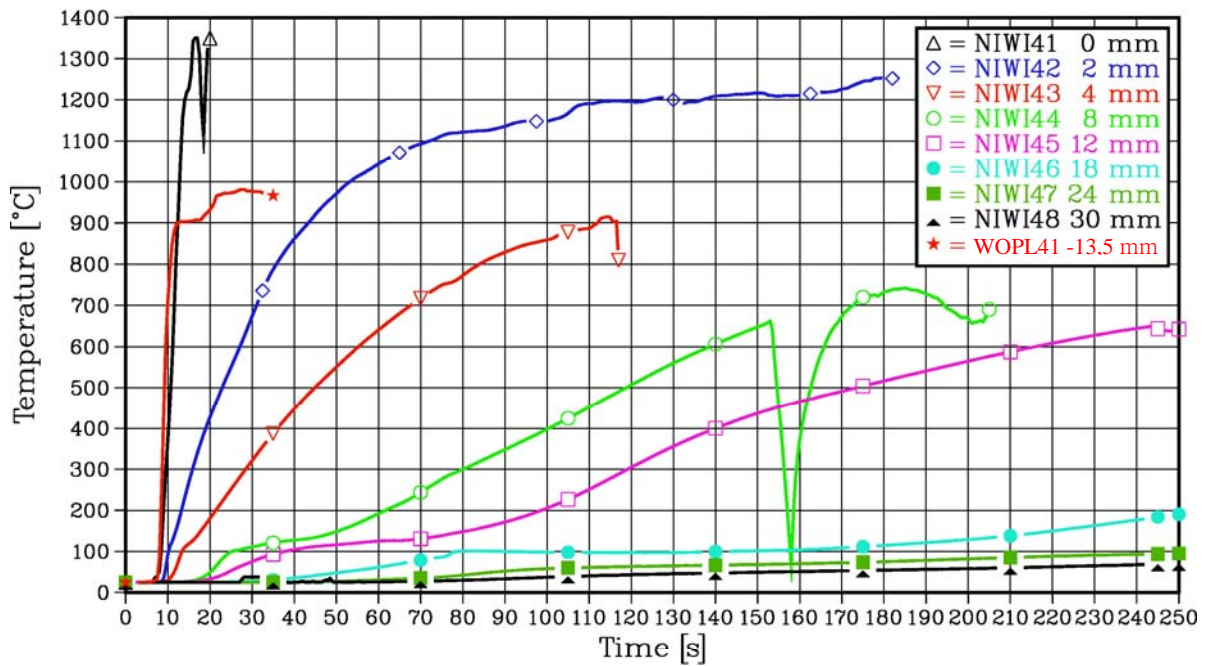
Figure 2-26: Temperature distribution at thermocouple module 4

2.2.3.5 Calculation of the Temperature Distribution in the Concrete

The temporal distribution of the temperature in the concrete at thermocouple modules 1 to 4 which are shown in Figure 2-23 to Figure 2-26 allows the calculation of the corresponding heat flux to the concrete surface. This requires the solution of the inverse heat conduction (IHC) problem where the acting boundary conditions, especially the heat flux, have to be determined by means of their measured effects in the depth of the concrete and which depend on location, on temperature, and on time. The problem was solved with a numerical method according to J. V. Beck [7], where the time integration is stabilized by a special regulation procedure (computer code SINCO). With the applied code only a first approximation of the heat conduction problem is possible. To assess the obtained result, the calculated temperature of the surface was used in a second step for a standard transient heat conduction calculation, where the results are compared with the measured concrete temperatures. This control is useful because of the tendency of the IHC solving methods to become unstable.

Another problem in application of the IHC solver is the change of the concrete properties during heat-up. Furthermore, the evaporation of the water contained in the pores of the concrete caused a hold-up in the temperature rise. This phenomenon shows up like an inhomogeneous material behaviour during the heating up process. Another heat absorbing process that takes place during heat-up is the chemical decomposition of the cement matrix. The weakness of the actual program version, where only constant material properties are accepted, requires the treatment of a short term phase with the properties of normal concrete and a long term phase using modified values for a changed concrete with a lower thermal diffusivity.

For their further use in short term IHC calculation the experimental temperature data must be conditioned by carefully smoothing. This pre-processing is necessary to avoid strong fluctuations due to the amplifying effect of the solving procedure.

Figure 2-23 shows the experimental results of instrumentation module 1. In contrast to the experiment ECOKATS 1 [8] with spreading of a pure oxide melt, here the thermocouples failed rapidly after contacting the metal melt. Neither the W-Re Element (WOPL11) nor the Ni-CrNi Element (NIWI11) at the concrete surface provides a meaningful measurement signal for the temperature determination. They only can be used for the indication of the melt arriving time. The remaining thermocouples are appropriate as long as no melt contact occurred. The most important measurement position for the IHC calculation is next to the surface. As obvious in Figure 2-23, thermocouple NIWI12 (at 2 mm below the surface) shows a suitable transient until about 70 s. Later on, there are disturbances. Therefore low uncertainties can be expected only for the initial time period with the highest heat transfer into the substratum.

The temperature measurements from module 2 are presented in Figure 2-24. Unfortunately NIWI22 failed already at t = 35 s and NIWI23 at the 4 mm position didn't work at all. Nevertheless, a similar heat transfer behavior to module 1 can be identified from the temperature increase at the 2 mm location. In both cases the 1000 °C level is reached at about 33 s.
Figure 2-25 and Figure 2-26 show the corresponding records from the modules 3 and 4 with similar results.

The result of the IHC calculation for module 1 is presented in Figure 2-27 with the label *"SINCO"*, the code name. The comparison of the calculated surface temperature with the corresponding measurement indicates the result as inconsistent. The records of the other three modules also show the fast failure of the surface elements. In subsequent transient heat conduction calculation the theoretical time behavior of the surface temperature was used as boundary condition. The results are depicted in Figure 2-27 as dashed lines and labeled under the header *"Post Calculation"*. The comparison with the measured temperature distribution shows a faster change in the concrete properties than observed in ECOKATS 1, where pure oxide melt acted on the substrate [8]. Therefore, satisfactory agreement between the heat transfer calculations and the measurements can be achieved only with a reduced thermal diffusivity of $a = 0.85 \cdot 10^{-6}$ m^2/s, instead of $1.03 \cdot 10^{-6}$ m^2/s. Then the measured temperature progress at the 2 mm position (NIWI12) is well reproduced and for the 4 mm position (NIWI13) a satisfactory comparison is obtained up to the begin of evaporation at about t = 10 s and again, after the decay of this disturbance, at about t = 60 s. The difference in the depth of 8 mm is caused by the inhomogeneous concrete properties and is of minor relevance for the determination of the heat flux at the surface for the short term phase up to about 60 s. Because of the transient character of the heat transport, an average heat flux value is determined by integrating over the time period of the outflow process which allows a meaningful comparison between the various measurement positions in the spreading area. Figure 2-28 shows the calculated heat flux over time with the averaged value of about 500 kW/m^2.

The following diagrams, Figure 2-29 to Figure 2-34 (in pairs with temperature distribution and heat flux), present the corresponding results for the modules 2 to 4. Despite the sometimes slightly differing conditions, the averaged values for the heat flux during the time period are within the narrow range of 400 kW/m^2 to 530 kW/m^2. In ECOKATS 1 the heat flux was limited typically to 100 kW/m^2 - 150 kW/m^2. This difference is primarily due to the metal melt in this experiment with a higher downward heat flux.

It must be stated, that the results of the transient heat flux calculations to determine the heat flux to the concrete surface are a first approximation only, as the melting process of concrete with chemical decomposition of the cement matrix and the change of the concrete properties with temperature and time are not modeled.
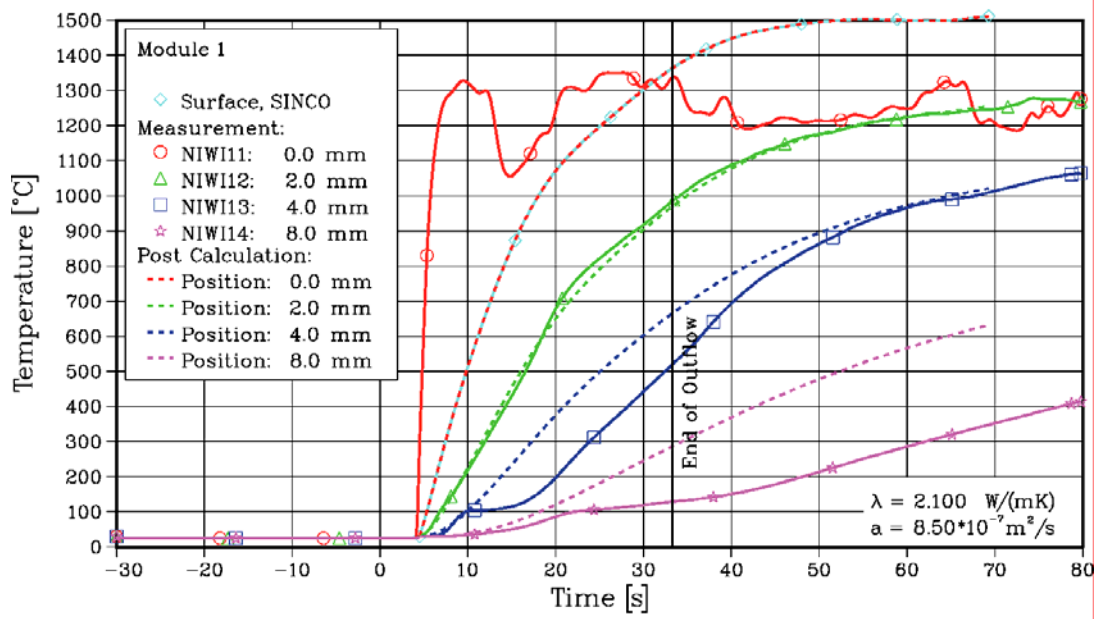
Figure 2-27: Results of inverse heat conduction calculation for module 1
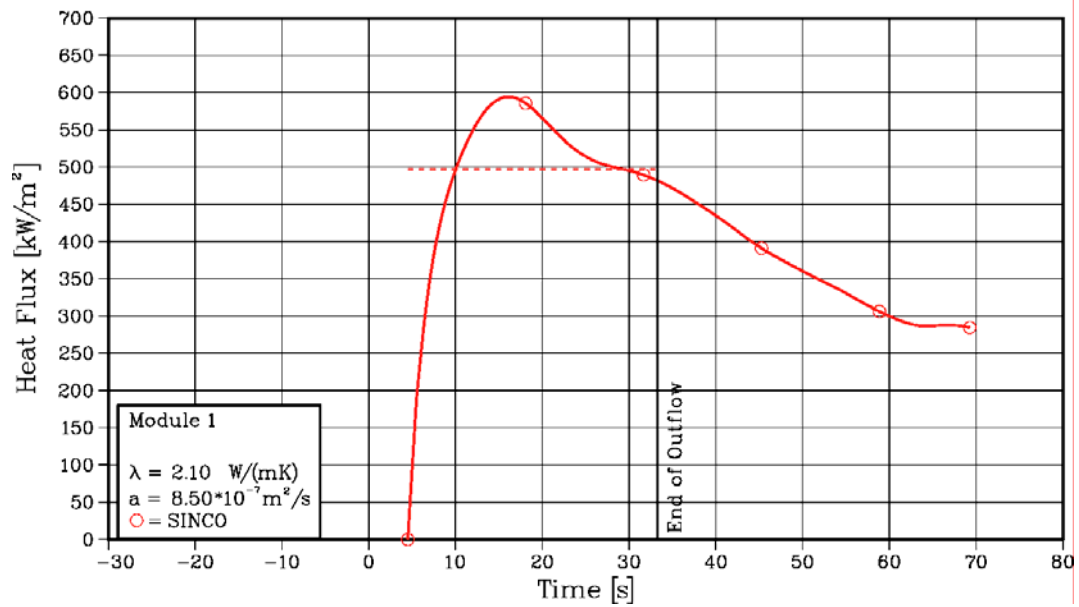
Figure 2-28: Calculated heat flux for module 1

32
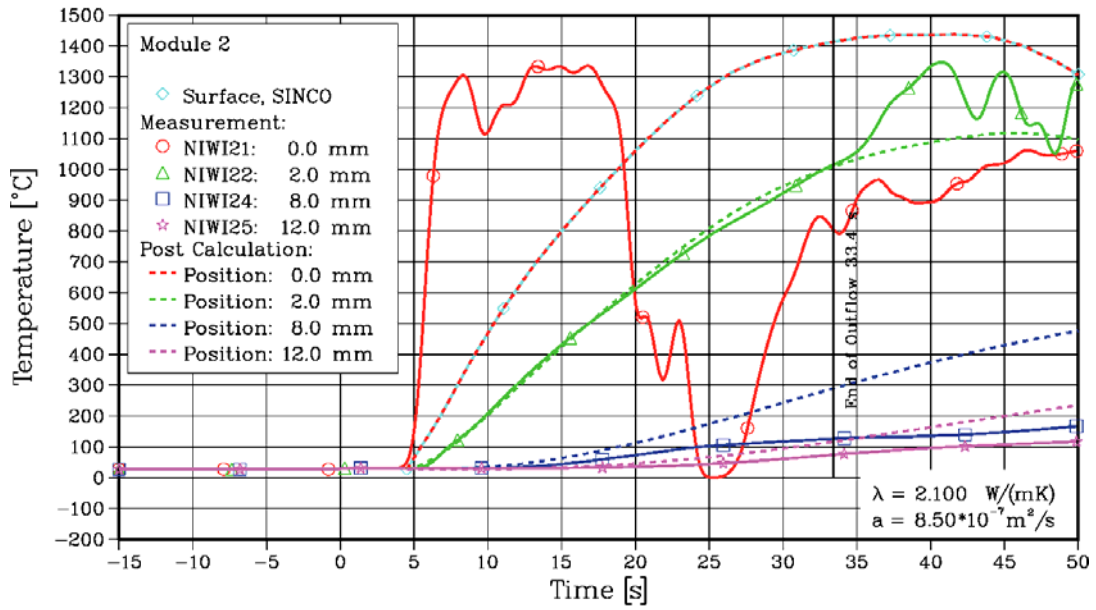
Figure 2-29: Results of inverse heat conduction calculation for module 2
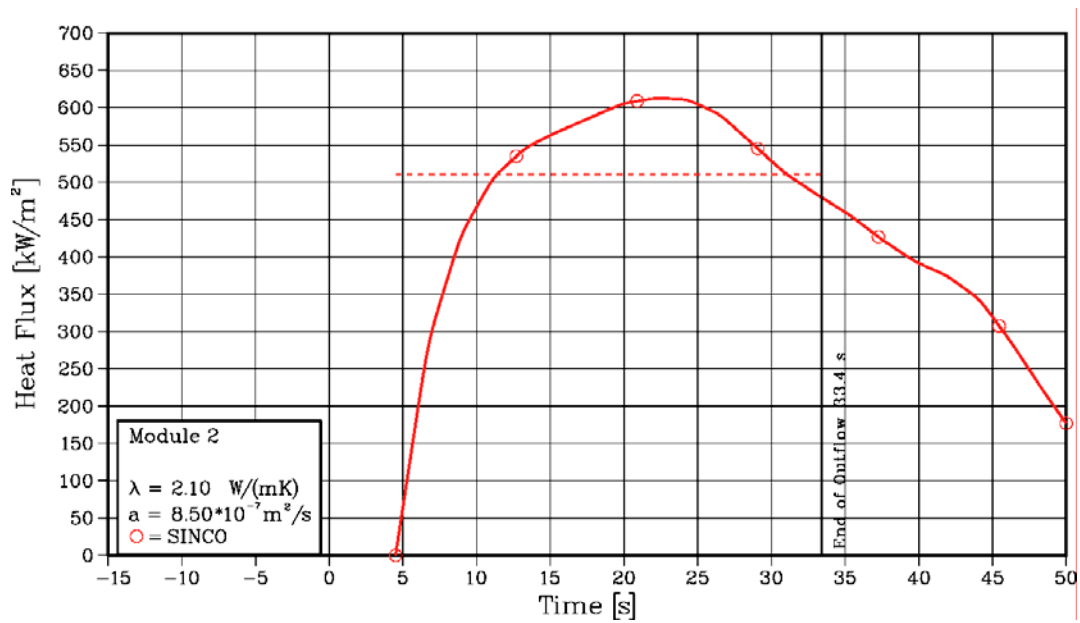
Figure 2-30: Calculated heat flux for module 2

33
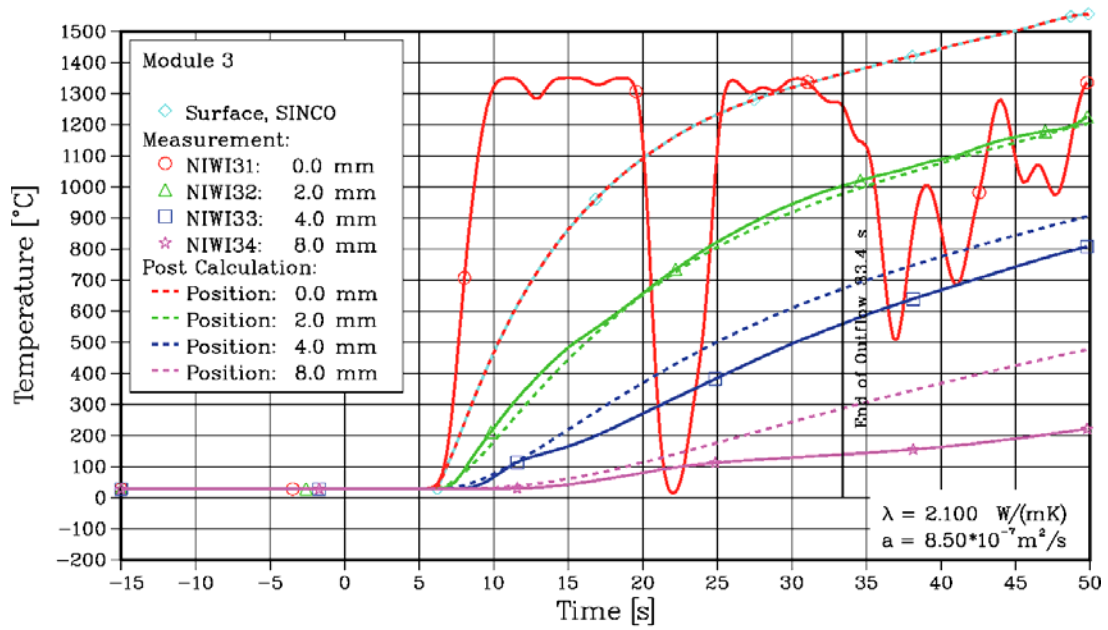
Figure 2-31: Results of inverse heat conduction calculation for module 3
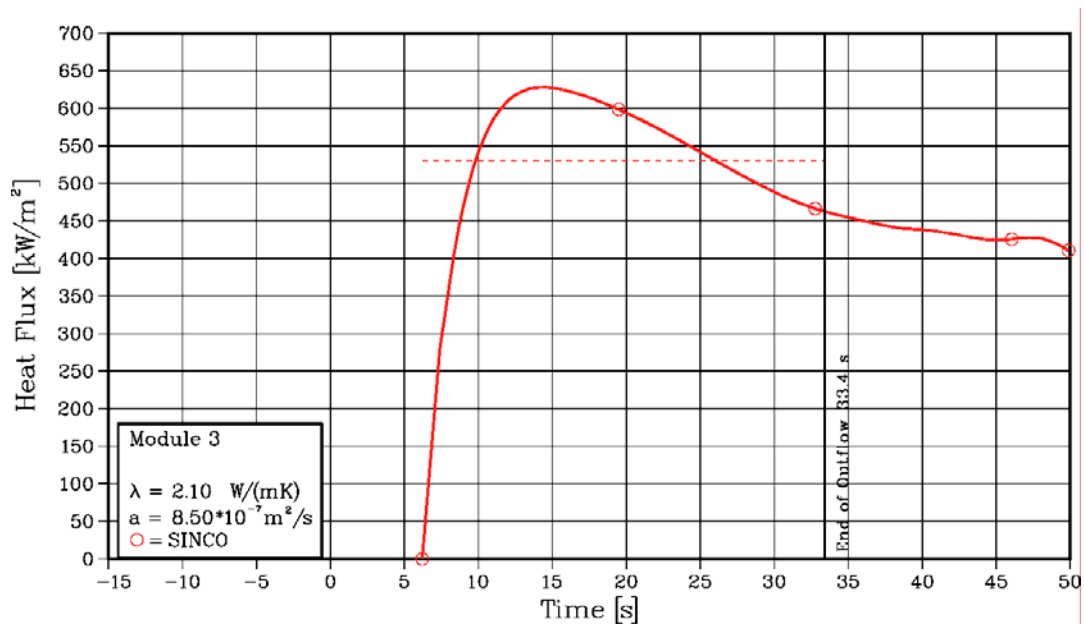
Figure 2-32: Calculated heat flux for module 3

34
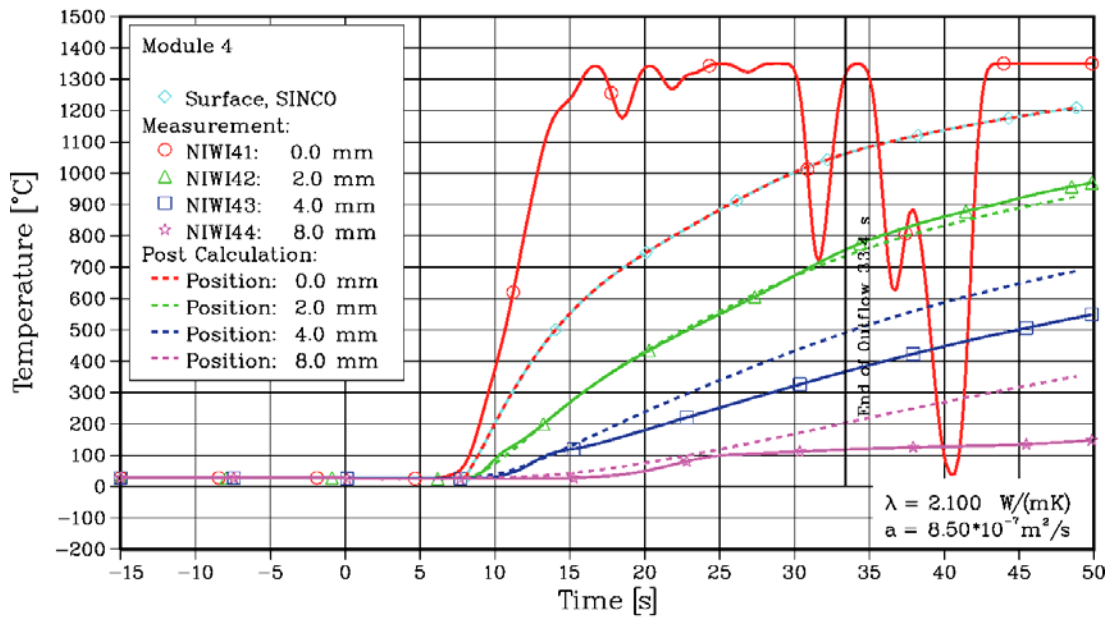
Figure 2-33: Results of inverse heat conduction calculation for module 4
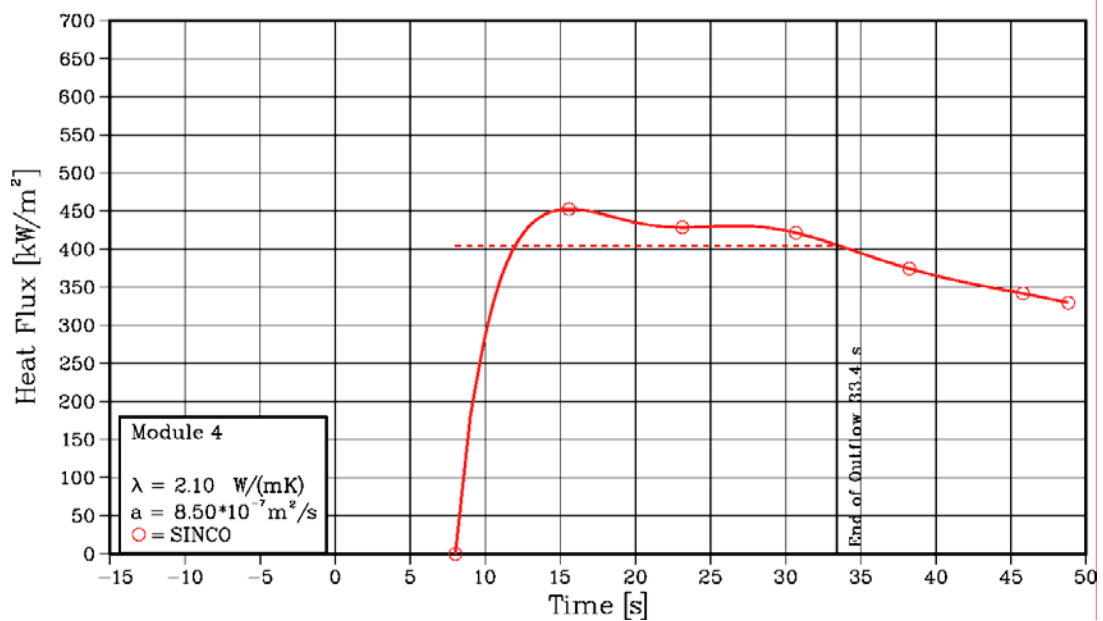
Figure 2-34: Calculated heat flux for module 4

3 Top Flooding of the Melt in ECOKATS-2

3.1 Experimental Results and Measured Data (D39, D40)

3.1.1 Behaviour of the Melt during Top Flooding

The device to flood the surface of the melt is described above in chapter 2.1.6 and the most important observations during the top flooding process are given in Table 2.

During the phase of intense concrete erosion, 67.1 s after start and 34 s after completion of the melt pour, water was given to the surface of the melt to study melt cooling by top flooding. The flooding was achieved by adding of 4.13 litres water/s by overflow over the 2 m wide weir (see Figure 2-1 and Figure 2-2). This first phase of water addition continued until 482 s, when the cavity was filled with about 15 cm water overlayer. Then the water supply was interrupted. The water smoothly covered the agitated melt surface, and no energetic melt water interaction nor steam explosion occurred. In this early flooding phase, film boiling was the expected contact mode between melt and water.

The surface of the melt was completely covered by a thin water overlayer after about 88 s as observed by the infrared camera. Figure 3-1 shows four different infrared pictures in which flooding occurred from left to right. For a better understanding the edge of the melt surface is indicated with lines. From the infrared records it was analyzed that the water spilled over the weir onto the melt surface at 75.6 s with a delay time of 8.5 s after opening of the valve. In each picture the time after beginning of flooding is given in brackets.
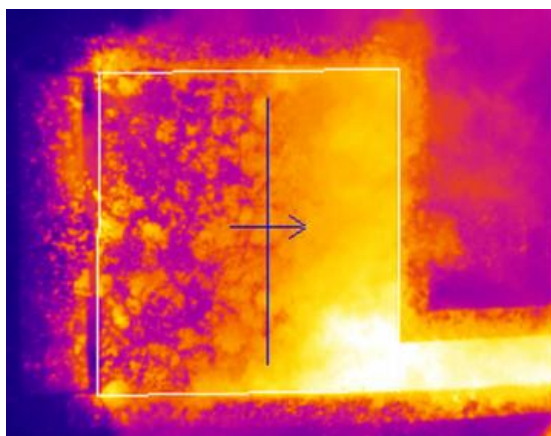
| Reference picture at 83.2 s [50.1 s] | Water front at 79.6 s [46.5 s] |
| Water front at 83.7 s [50.6 s] | Water front at 88.1 s [55.0 s] |
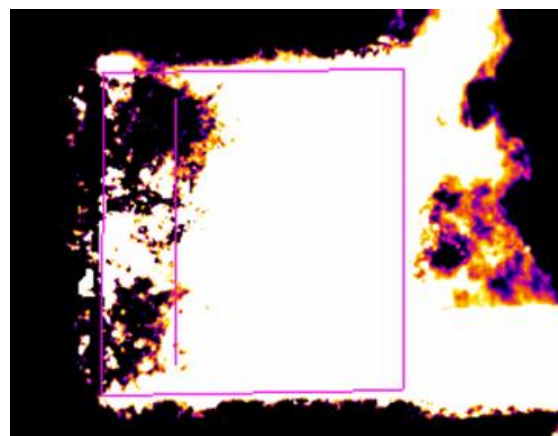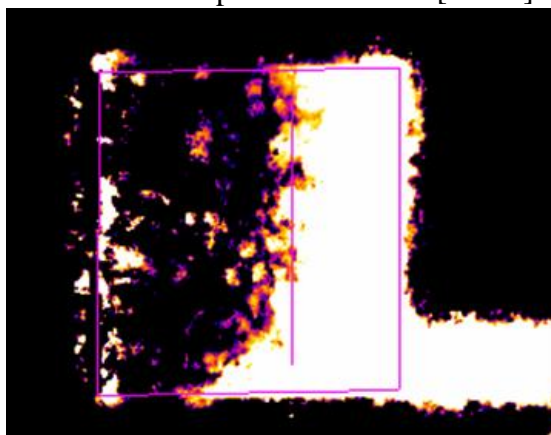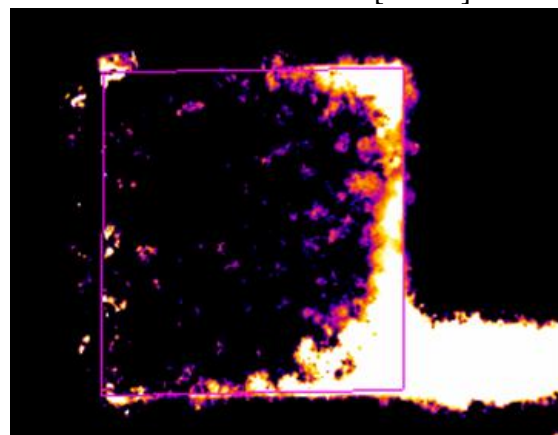
Figure 3-1: Top flooding process from infrared measurement

The first picture is a standard infrared record in which the waterfront cannot clearly be recognized. Therefore the temperature scaling was reduced to the region from 600 to 700 °C. As a result, the areas with lower temperatures appear dark, whereas the hot areas seem bright (or even white).

The evaluation of the infrared pictures provides the spreading characteristic of the water front, given in Figure 3-2. It shows that after 13 s the whole spreading area was already covered with water. The start up transient for the top flooding was very short in comparison to the total first flooding period of 415 s.
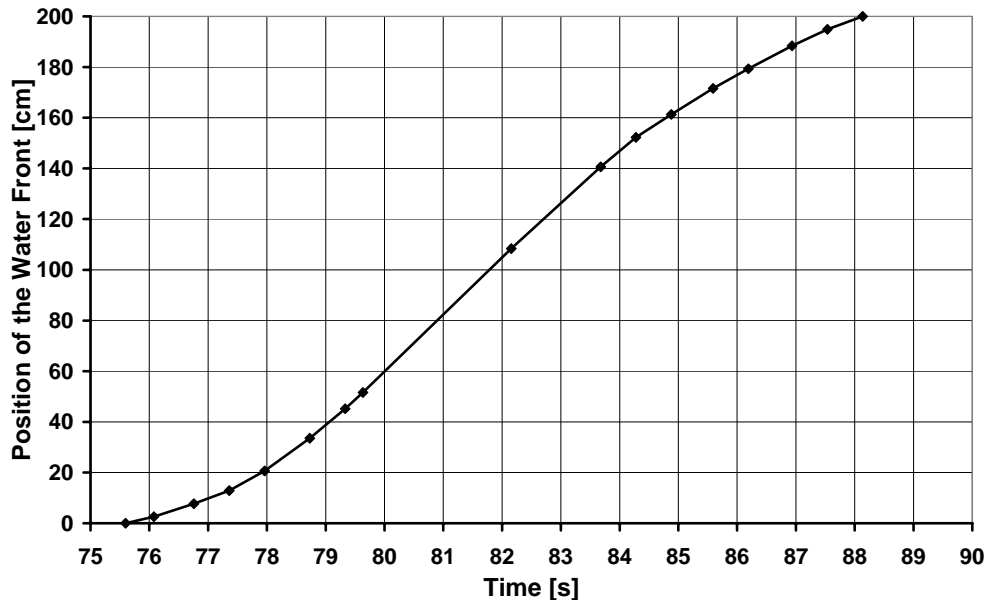
Figure 3-2: Position of the Water Front during Top Flooding

The existence of the water layer does exclude further quantitative evaluation of melt surface temperatures measured by the infrared camera, as water is a strong IR absorber in the measuring range.

The formation of a surface crust on the top of the melt, and first quenching of the surface crust are shown in the photographs of Figure 3-3, in which flooding occurred from right to left. The photographs were taken from above the melt. Since in the first contact phase the evaporating steam was strongly overheated, no mist was formed above the water, so that the surface is clearly visible in Figure 3-3 a) – d). Later on, the pictures were partly obstructed by condensing steam (especially from 140 s to 225 s).

After about 120 s, the shallow water layer cooled the melt surface to some 800°C (orange colour). A relatively even, thin surface crust was formed, through which the gas bubbles (hydrogen and steam) from the decomposing concrete were released to the water layer. This is clearly seen after 225 seconds in Figure 3-3 e) – h), when the crust was less bright (dark-orange), but the holes through which the gases were released, show the brighter bulk of the melt. These holes were relatively uniformly distributed over the surface and their total number was about 30. About 50 % of these holes were closed by further crust growth; however, 16 holes remained open and piled up volcanic vents through expulsion of melt material during the further course of the test (see below).

The crust was anchored to the vertical sidewalls of the cavity already in the early phase of flooding, and no bright gap was visible near the walls or in the central cavity. Later observations confirmed that the crust was firmly anchored to the walls throughout the test. With the exception of the vent holes, the crust was completely closed. A floating crust was never observed.
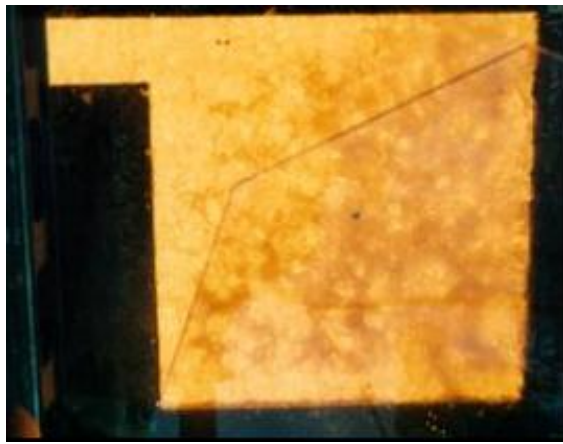
a) 93 s

b) 116 s

c) 126 s

d) 140 s

e) 225 s

f) 230 s

g) 240 s

h) 260 s

Figure 3-3: Formation of surface crust and its quenching by water supply from the right side

Starting at 116 s in the right part of Figure 3-3 b), the bright surface crust was quenched by the coolant flow, probably caused by transition from the film boiling to the nucleate boiling. This is clearly visible as a sharp transition of the crust colour to black, and continuously proceeding from right to left, as seen in Figure 3-3 e) – h). The quench front was relatively straight, indicating the absence of major peaks and valleys on the crust surface during this period. The bright spots in the dark crust, visible in Figure 3-3 e) - h) as vent holes, are clearly identified as the origin of volcanoes which developed during the further test and which were visible after the test (see the following figures).

At 280 s the camera above the melt was destroyed by the intense thermal radiation and hot gases, and no further photos could be taken. In addition, the steam condensation increased considerably; because of less overheat of the released steam, so that the view to the surface was nearly totally blocked.

The period of adding water to the melt was stopped at 482 s when the cavity was nearly filled. This first flooding period lasted 415 s. After decrease of the water height a second flooding period was initiated from 750 to 835 s. During flooding, the visibility improved and important modifications of the crust surface could be recognized. Figure 3-4 demonstrates these flooding periods with the increase of the cavity weight by adding water and its decrease by the evaporation and some leakage. A third and fourth flooding were initiated in the periods 1050-1225 s and 1770-1890 s to refill the cavity. Further refills were made later on.

During flooding the crust in the central region of the cavity was elevated and formed a flat hill some 20 cm above the original level. Figure 3-5 shows the filled cavity after the sixth flooding period with the elevation of the melt surface. A series of volcanic vents were piled up releasing steam, but no ejection of hot melt droplets occurred.

A total of 16 volcanoes were identified on the 2 m x 2 m spreading area. The volcanoes, 10 to 15 cm high, were generated by the lava-type outflow of oxide melt under water, driven by the gases from the decomposing concrete through vent holes in the crust. No ejection of melt particles was seen. This agrees with the observations directly after the test, in that no loose particles were found on the upper crust surface.
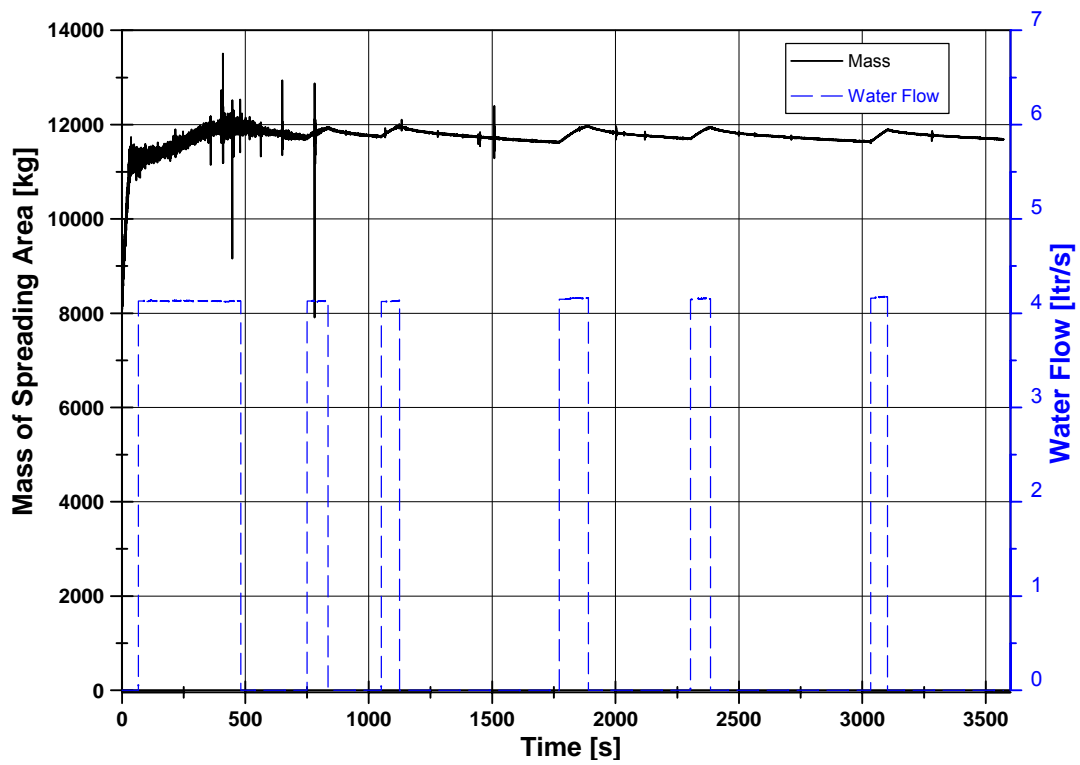
Figure 3-4: Weight of cavity including melt and cooling water with periods of water flow

Figure 3-5: Water layer above the melt at the end of the 6th flooding period

3.1.2 Temperatures at the Concrete Substrate

Figure 3-6 shows the most important measured temperatures in the concrete thermocouple modules 1 – 4 plotted over the first hour after spreading and flooding. Water addition is marked by blue bars. Temperatures are given for the initial positions 0, - 2, and - 4 mm from the concrete surface. All thermocouples failed during the first 120 s of melt attack between 1300 to 1350 °C, which corresponds to the decomposition temperature of concrete. Subsequently, most of the thermocouples formed new thermo-pairs that give plausible measurements of the drop of the interfacial concrete temperature and of the long-term temperature, which is close to 700 °C. However, no measurements are available for the temperatures in the melt as the thermocouples failed by the thermo-chemical melt attack. The temperatures show no significant influence of cooling by top flooding, and their slow reduction with time is mainly due to heat absorption by the 25 cm thick concrete bottom. This confirms the limited influence of top flooding.
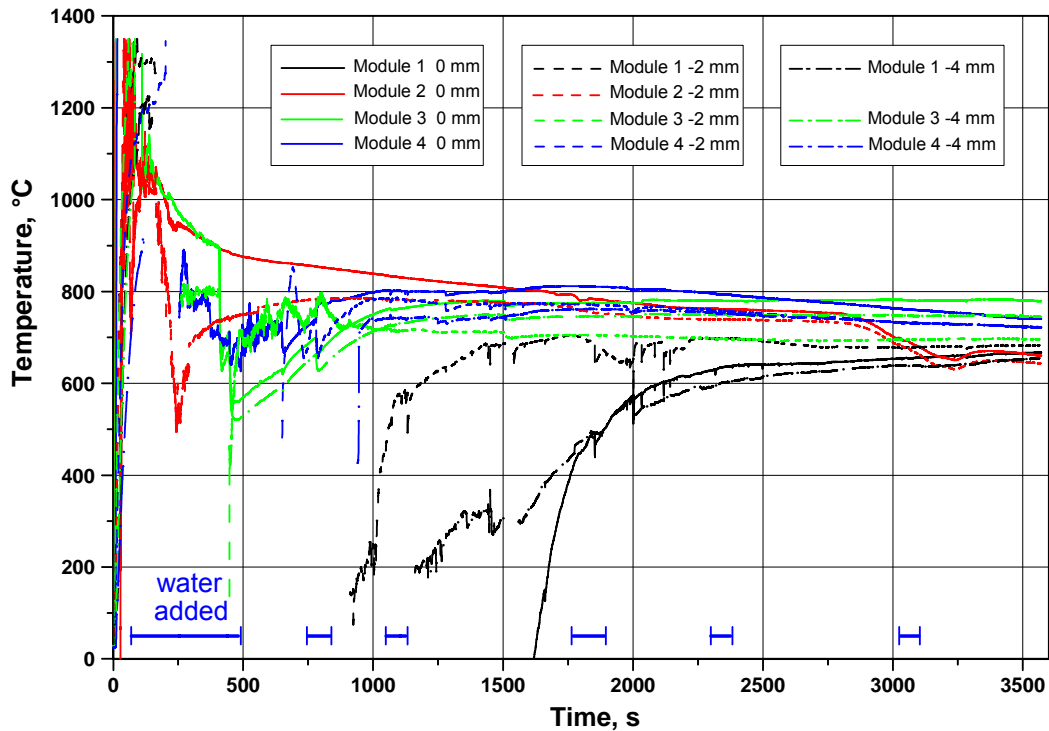
Figure 3-6: Temperatures measured by thermocouple modules 1 – 4

3.1.3 Erosion of the Concrete Substrate

The four thermocouple modules located in the concrete layer according to Figure 2-9 allowed the evaluation of the downward erosion of the concrete substrate by the hot melt. This was determined by the failure of thermocouples in modules 1 - 4. Figure 3-7 shows a first period of strong concrete erosion with a peak erosion rate of 0.05 mm/s, and a substantial reduction of concrete erosion after some 400 s. The overall thickness of the melted concrete layer was some 12 to 18 mm only. This behaviour is typical for unheated melt and is due to the growth of an interfacial metal crust between the melt and the concrete. Also after formation of the interfacial crust, steam releases from the heated concrete into the overlaying melt continued, eventually through vent holes and volcanoes in the surface crust.
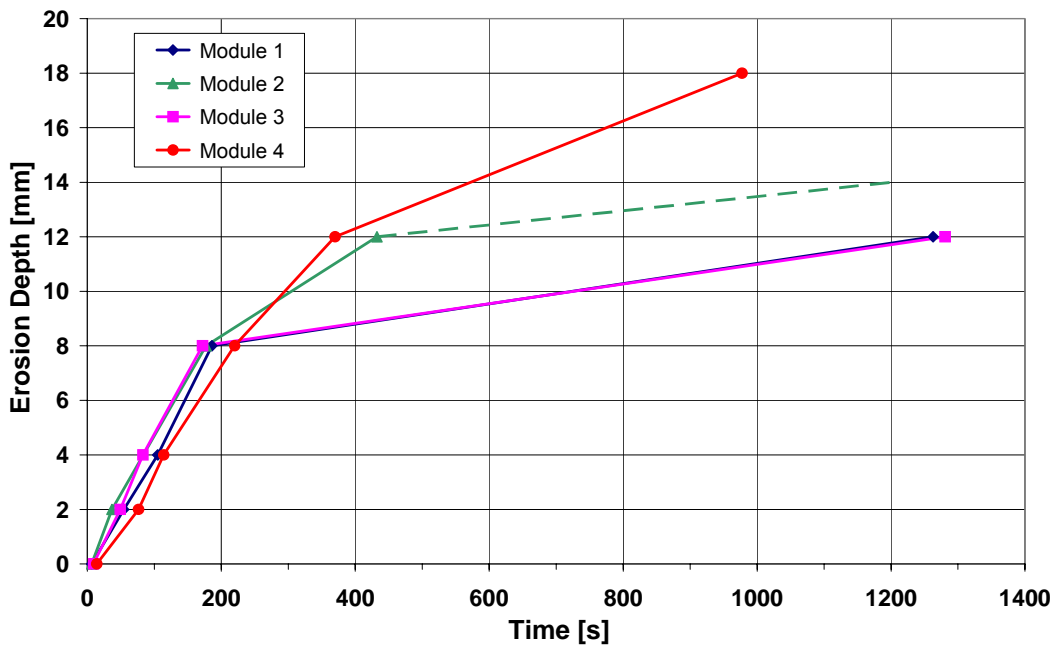
Figure 3-7: Erosion of the concrete substrate by the spread melt

For the post test analysis, a trench was carved through the middle of the solidified melt (see Figure 3-23). At the beginning and at the end of the trench the erosion depth could be determined in the middle of the front wall and the opposite wall. The values are given in Table 5. Figure 3-8 shows these two positions.

Table 5: Erosion at the concrete side walls and at the supply channel

Location of Erosion	Erosion Depth [mm]	Position from above [mm]
Middle of the front wall	9	180
Middle of the opposite wall	20	300
Right channel wall	51	340
Left channel wall	48	270
Bottom of the channel	37	-

In the supply channel the erosion could be easily inspected at the beginning of the channel where the whirl basin was mounted. It is plausible that here the erosion was maximum because of the long term supply of the hot melt. After removing the supply

channel it was obvious that the edges direct in contact with the whirl basin were not changed noteworthy. About 100 mm behind these edges the maximum erosion depth was reached. Figure 3-9 shows the erosion at the beginning of the supply channel.

| front wall | opposite wall |
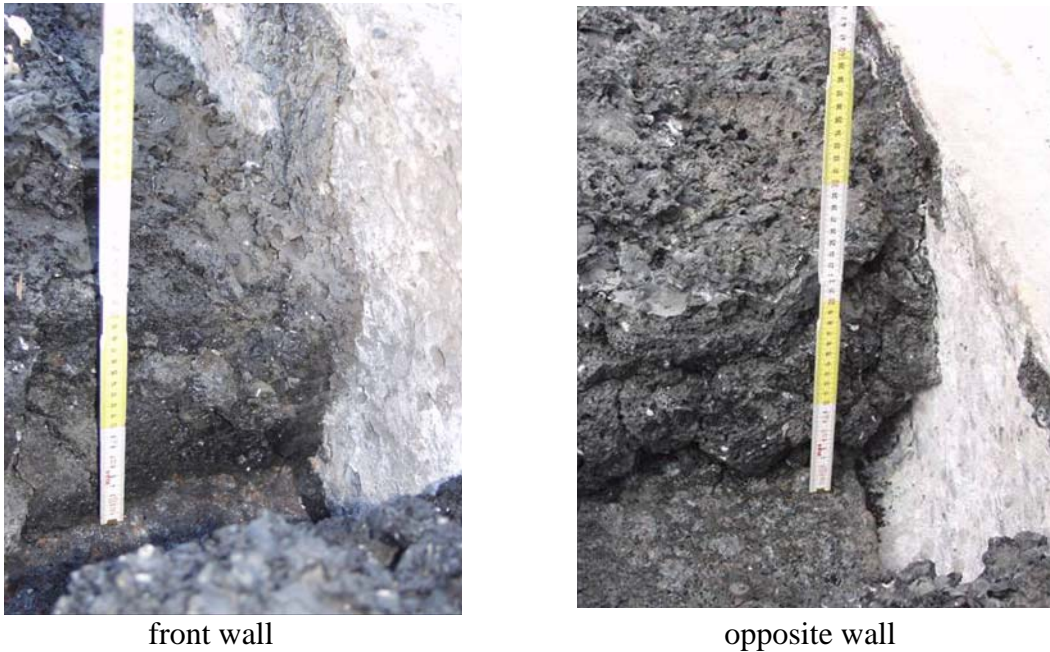
Figure 3-8: Erosion of concrete at the cavity walls

| front view | right channel wall from above |

Figure 3-9: Erosion of concrete at the beginning of the supply channel

3.1.4 Structure of the Solidified Melt

To demonstrate the final melt surface with its volcanic vents and hills, a sketch is shown in Figure 3-10. In this sketch darker colors represent higher elevations. Figure 3-11 and Figure 3-12 show the real structure of the solidified melt surface after the test. The initial flat crust was elevated in the inner part of the spreading area by up to 20 cm. The elevation of the central crust was probably driven by the accumulation of gases under the crust, resulting from concrete erosion. The crust had a rough irregular surface, but no loose particles were found on the surface, that could be produced e.g. by volcanic eruptions. The upper elevated crust layer contained substantial open and closed porosities.

The flat hill had several vents through which gases were released. Also the regions around the hill were weakly lifted, and had some openings, as shown in Figure 3-13.

The crust at the vertical sidewalls was firmly anchored to the concrete and remained in its original position, thus constituting the lowest crust level (see Figure 3-14).

Because of the small dimension of the supply channel no elevation of the melt crust occurred inside the channel, but a lot of volcanoes piled up as shown in Figure 3-15. No melt particles were ejected through the vent holes.

A total of 16 volcanoes were identified on the solidified spreading surface (see Figure 3-16 and Figure 3-17). The volcanoes, 10 to 15 cm high, were generated by lava-type outflow of oxide melt under water, driven by the gases from the decomposing concrete through vent holes in the crust. No ejection of melt particles took place as no loose particles were found on the upper crust surface.

After drying, the upper elevated, highly porous crust layer crashed into small particles during the next hours and days without any external influence, probably because of internal strain or re-crystallization, and a rubble layer a few cm high covered the solidified melt.
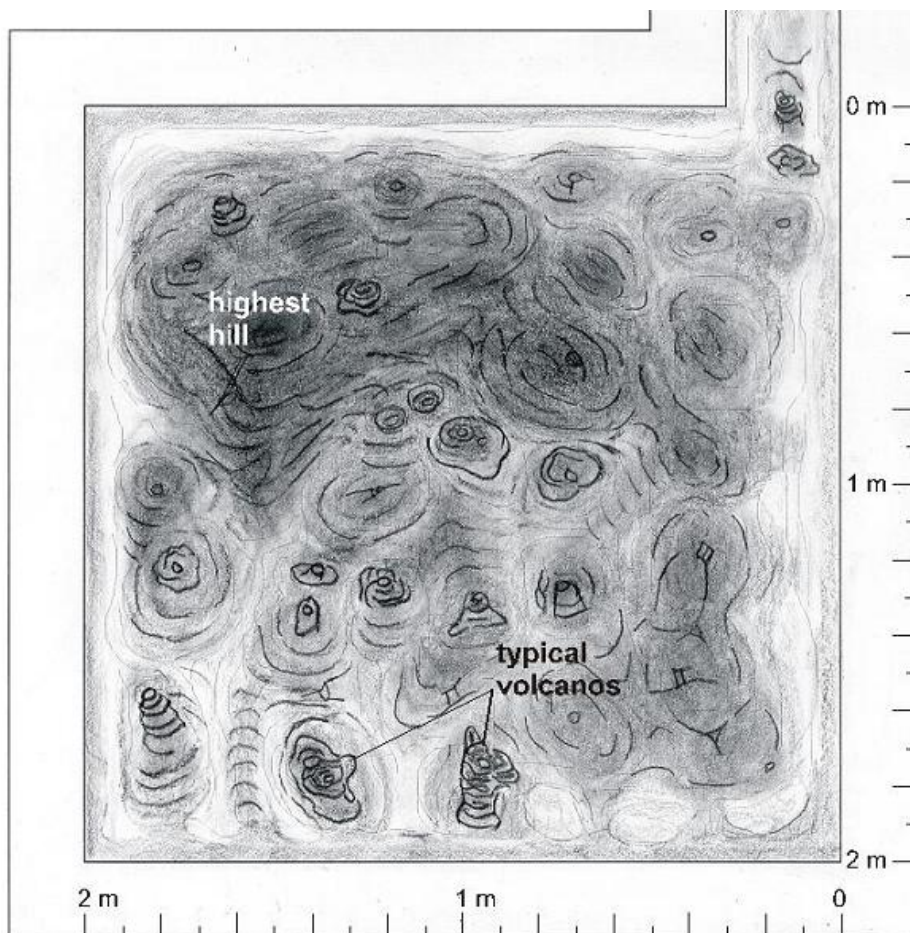
Figure 3-10: Sketch of the melt surface, indicating volcanic vents and hills, darker color represents higher elevations.

Figure 3-11: Surface of the solidified melt. View from the weir after 3 hours

Surface of the solidified melt

Profile of the highest elevation

Figure 3-12: Solidified melt from the left side. Supply channel on the right.

Figure 3-13 : Elevated region near the weir with openings from vents

Figure 3-14: Anchored melt crust at the sidewalls

Entrance section (1m long) of the supply channel, seen from the crucible

Figure 3-15: Solidified melt surface in the supply channel

Figure 3-16: Volcanoes, seen from the weir after 3 hours. Highest hill in the background
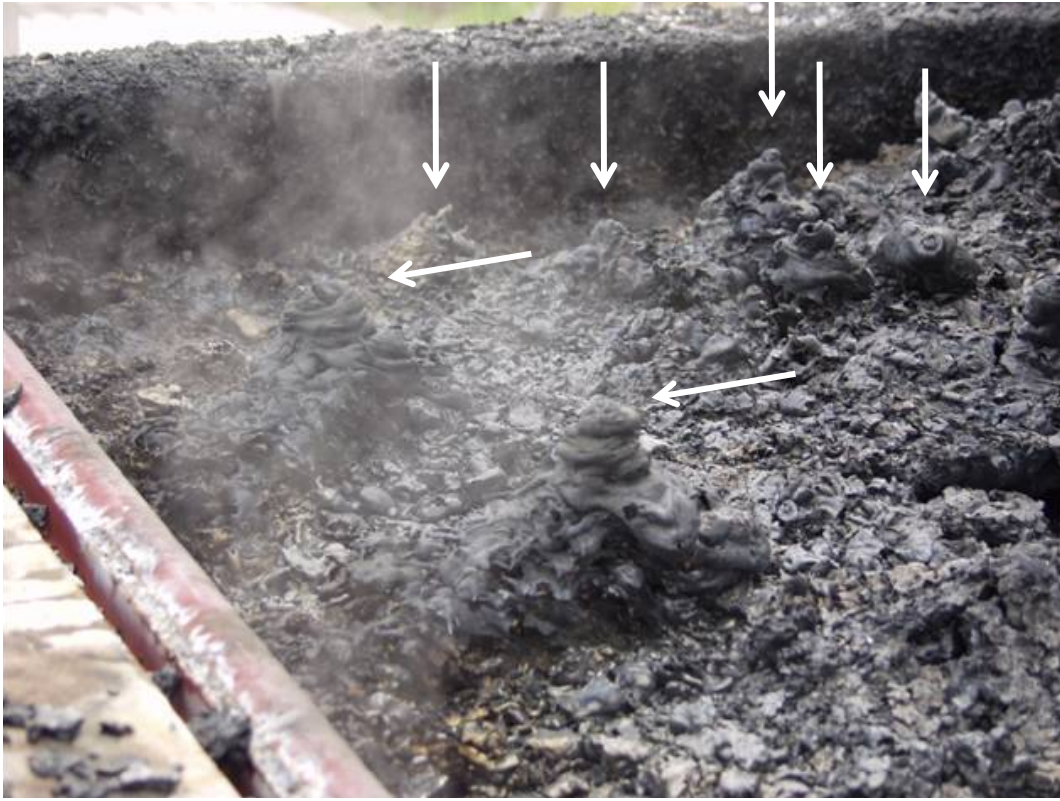
Figure 3-17: Large and small volcanoes which piled up through holes in the surface

3.1.5 Open and Closed Porosities of the Oxide Melt

Efficient coolability by the top flooding requires open porosities in the melt surface. Therefore the porosity of the melt was investigated in detail after the test to identify that part of the melt, from which heat was efficiently removed to the water overlayer.

As a first step, the mass and porosity of the uppermost crashed oxide layer was estimated by removing and weighing the rubble material. For this purpose, the melt surface was divided into 16 regular areas of 0.5 m x 0.5 m shown in Figure 3-18. For each area the profile of the surface was measured before and after removing the loose particles. With the mass and the averaged volume of the removed layer the porosity of each area could be estimated and is additionally listed in Figure 3-18. An accumulated mass of 230.3 kg was removed from the surface and the porosity of this layer was determined between 49 and 71 %. The largest masses were taken from the areas 4, 7 and 10; whereas the highest porosity of 71 % was found at the area 8 followed by the areas 3, 6 and 9. These areas are in the regions with the highest elevation.

The mass of the crashed oxide layer corresponds to 7 % of the total melt mass and represents about 1.7 cm height of the compact oxide melt.

After removing the upper rubble layer, large open cavities appeared in the surface at and around the highest elevation shown in Figure 3-19. The large cavity at the lower edge of Figure 3-19, at area 8, was a solitary cell, 12 cm deep, whereas the adjacent large openings above were interconnected expanding over the areas 2, 3, 4, 6 and 7 and had a maximum height of 8 cm. In Figure 3-21 a look into the extended cavity is given. It looks like a stalactite cave.

Along the concrete sidewalls in the areas 2 to 4 and 4 to 12 (see Figure 3-18) a gap is visible at the surface, which is about 2 cm wide. This gap is restricted to the uppermost porous crust layer and does not extend to the more compact melt structure below. The gap was probably generated by shrinking during cool-down of the porous crust and couldn't contribute to cooling of the bulk of the melt by water ingression. At the edges of the melt surface the gap continued diagonally by cracks about 1 to 2 mm wide. A section of the gap in the area 8 is shown in Figure 3-22.

After removing the uppermost crashed and highly voided melt layer a trench, about 20 cm wide, was carved by hammer and chisel along the centerline of the melt for further analysis of the melt porosity and constitution in the depth. Figure 3-23 shows the trench through the melt seen from the front side. Figure 3-24 gives schematically the condition of the melt after solidification. Figure 3-25 to Figure 3-27 show the structure of the solidified oxide melt at different positions in the trench. Some of the cracks in Figure 3-25 evolved during digging of the trench. Figure 3-27 gives the left side of the trench in the region where the melt is anchored with the concrete wall. Measurements in the channel show that the height of the bulk of the melt varied from about 16 cm near the concrete sidewalls to 23 cm in the central region. As seen in the figures, the bulk is highly compact with homogenously distributed gas bubbles from 1 mm to 5 mm. In spite of a high measured porosity from 45 to 50 %, the closed condition of the porous structure excluded water ingression from the top and no efficient cooling of the bulk melt. The measured slow cool-down at the concrete interface shown in Figure 3-6 is a consequence of this dense structure.

For the upper region of the melt with open porosities and the height of 2 to 5 cm, a porosity of about 50 % was estimated. It can be assumed that this upper layer was cooled by water penetrating from the top.

From the investigations of the solidified melt it is concluded that only the uppermost

3.2 – 3.6 cm of the dense (unvoided) oxide layer were transferred into a configuration that was coolable by water ingression due to its high porosity. This corresponds to 14 - 18 mass-% of the actual test. From the bulk of the melt, heat transfer took place by conduction and convection in presence of stable crusts, which has a low efficiency only.
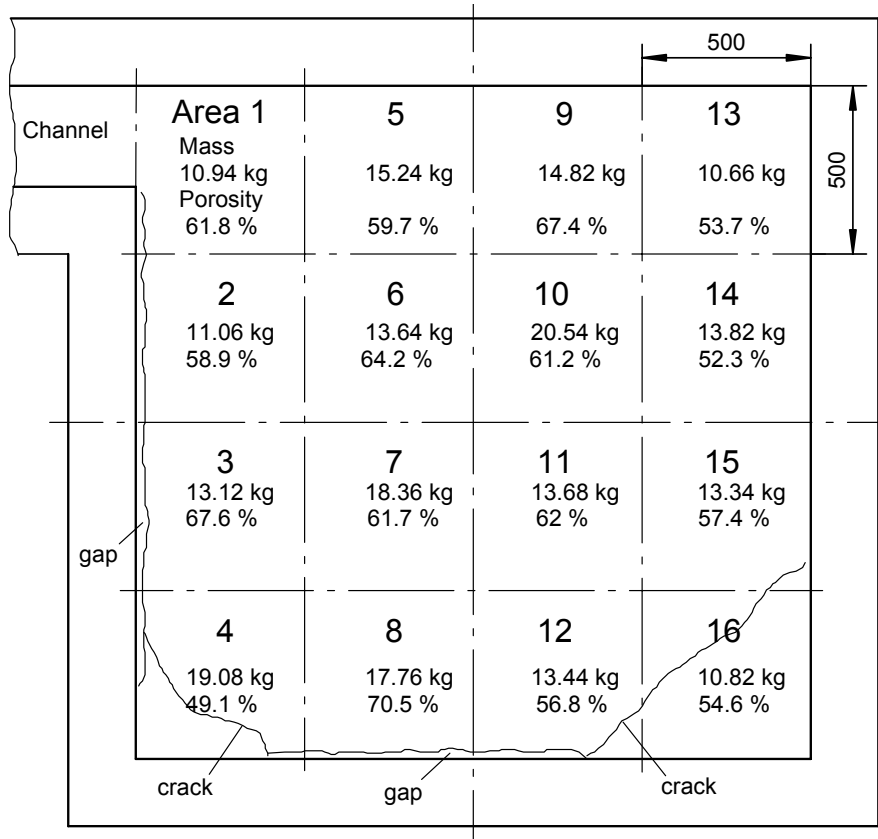
Figure 3-18: Mass and porosity of the upper crashed layer for different areas of the melt surface

Figure 3-19: Melt surface after removing the upper crashed layer

Figure 3-20: Melt surface at the highest elevation after removing the upper layer

Figure 3-21: View into the cavity at the highest elevation (see arrow in Figure 3-20)

Figure 3-22: Gap at the concrete sidewall in area 8 (see Figure 3-18)

Figure 3-23: Trench through the melt to investigate the melt constitution, opposite wall in the background, from which the weir is removed

Upper, open-porosity layer very brittle, 1-18 cm high 49-71 % voids

Lower, open-porosity layer not crushed, 2-5 cm high 50 % voids

Bulk of the oxide melt, 16-23 cm high, 45-50 % closed voids

Metal layer 4-6 cm high

Concrete
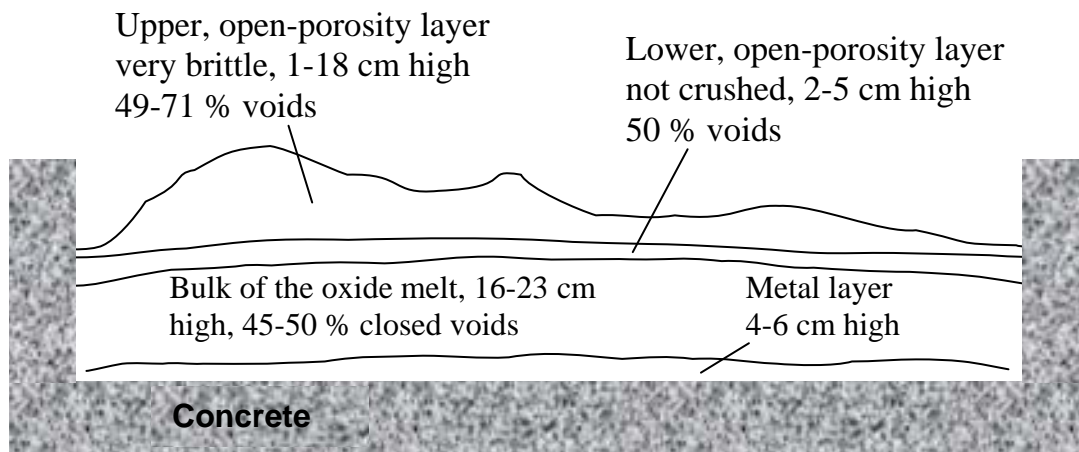
Figure 3-24: Schematic structure of the solidified melt

Figure 3-25: Right side of the solidified oxide melt in the middle of the trench.

Figure 3-26: Left side of the solidified oxide melt in the trench, 1.4 m from the front side.

Figure 3-27: Left side of the solidified oxide melt in the trench at the opposite wall.

3.1.6 Metal Plate beneath the Oxide

The bottom in the trench is formed by the metal part of the melt and produced a very hard, continuous plate that couldn't be cut. In the centre of the metal plate a hole was found of about 8 cm diameter which probably was generated by gases from the decomposing concrete substrate especially from the concrete of thermocouple module 3 that was placed at this position. At the other places of thermocouples modules no penetrations were found in the metal plate. Figure 3-28 gives a close-up view of the lower metal plate in which some knobs, 5 mm high, are seen that were evenly distributed over the whole plate. They were probably built by gases from the decomposed concrete.

Measurement of the upper surface of the metal layer was made in the trench. The height is referred to the –12 mm level of the original concrete bottom, assuming a constant downward erosion of the concrete over the area of the trench (see Figure 3-7). The profile of the plate was nearly symmetric and began at the distance of 5 cm from the sidewalls with the height of about 40 mm. The height increased continuously to about 57 mm at the distance of 70 cm, remaining constant to the centre. The thickness of the metal layer was indeed higher than theoretically calculated, but it is certain that the metal fraction of the melt was not more than planned. One reason for the higher metal layer is that the bottom metal layer in the whirl basin was nearly completely transferred to the large cavity. Examination of the whirl basin showed only a small residual metal layer, 27 x 27 cm wide and 1 cm thick. Another reason is the unknown bottom surface of the metal layer which may be rough and irregular and may have detached from the bottom concrete surface. Unfortunately, the lower side can not be inspected.

Figure 3-28: Structure of the metal plate at the bottom of the melt

3.1.7 Extracted Energy by Top Flooding

In the experiment ECOKATS-2 the total weight of the spreading cavity was measured during spreading and subsequent top flooding, so that inflow and evaporation of coolant water are included in the measurements. Figure 3-4 shows the history of the registered weight during the experiment for the first hour with the associated periods of constant water inflow of 4.13 l/s. Only 6 of totally 9 applied flooding phases are shown. The later flooding phases caused no major boiling processes; their time periods are given in Table 2. The water level in the spreading cavity was controlled manually by opening and closing the water valve. The water inflow was stopped when the water level reached the upper edge of the cavity. After a level loss of more than 5 cm, a new flooding period was started filling up the cavity again to the upper edge. This procedure was repeated for 9 flooding phases in total. Because of the high evaporation rate, the first flooding phase took the longest time, namely 414.7 s. It started 67.1 s after begin of spreading and ended at 481.8 s. As mentioned in chapter 3.1.1, in the first flooding period the cooling water reached the melt surface with a delay of 8.5 s.

The weight curve in Figure 3-4 was used to estimate the evaporated water and hence the associated cooling energy extracted from the melt. For this purpose, the curve with its inevitable unsteady loadings due to melt/concrete interactions and boiling was smoothed. Its time derivative yields the mass change $\dot{m}$ of the installation in kg/s. The evaporation rate $\dot{e}$ from the water layer is the difference of the water flooding rate $\dot{w}$ and the mass change $\dot{m}$:

$$\text{Evaporation rate } \dot{e} = \dot{w} - \dot{m} .$$

This evaluation neglects the role of overspill of the coolant water or leakages that occurred in the installation. Another systematic error when evaluating the heat flux is the time delay between flooding with subcooled water at room temperature and onset of evaporation after heat up to boiling temperature. During this period, the extracted heat does not result in a mass loss.

Figure 3-29 gives the evaluated evaporation rate together with the flooding rate, which was delivered to the melt surface during the flooding periods. The high "evaporation" peak at 443 s occurred due to some melt/crust relocations which caused some water overflow over the crucible wall. Further melt/crust relocations with water overflow occurred at 658 s between the first and the second flooding phases, and at the very beginning of the second flooding phase at 774 s. It is evident that the melt or crust relocations increase the evaporation rate as new surfaces are exposed to the coolant water. But with the involved water overflow, the calculated evaporation peaks are overestimated.

During the second flooding phase, visual observation noticed the elevation of the melt surface, which may be the reason for the two peaks in the evaporation rate.

The evaluated evaporation rate shows a remarkable characteristic during the flooding periods: The evaporation rate increases during flooding and continuously decreases after stop of water supply. This behaviour is not fully understood, but may be due to partial uncovering of elevated parts of the melt, as is visible in Figure 3-5. Parts of the higher crust surface were dried out when the water level was low, and therefore the evaporation rate reduced. Inversely, adding water to the partly uncovered melt increases the evaporation rate.
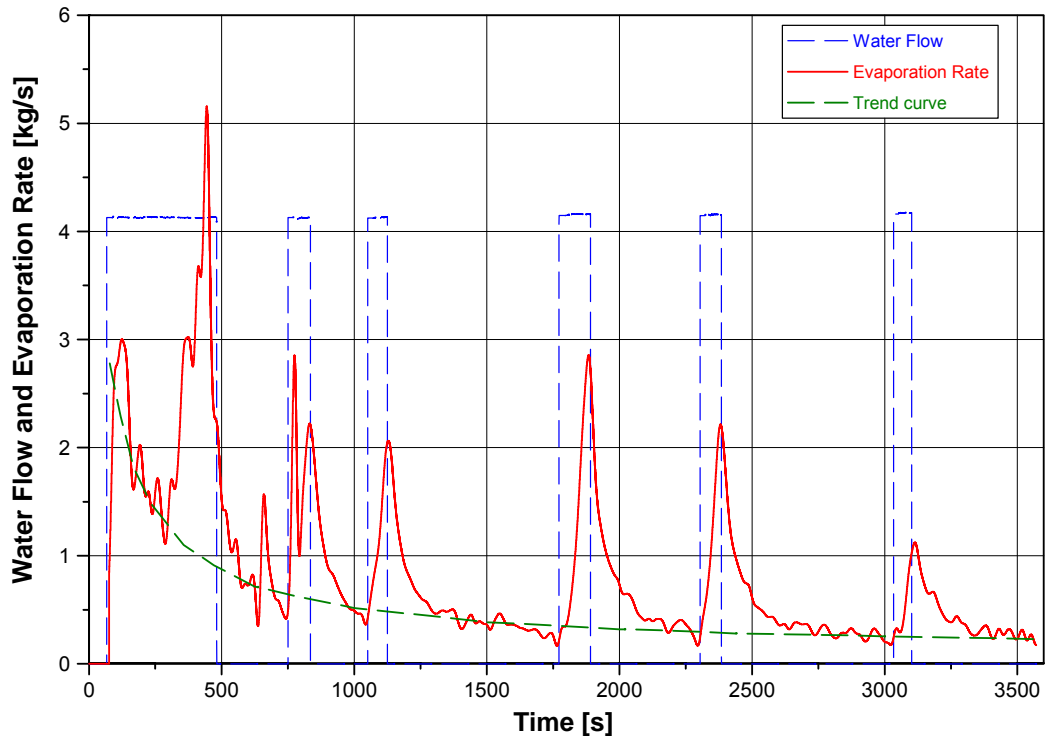
Figure 3-29: Water flow and evaporation rate during the top flooding processes

In Figure 3-29, a lower trend curve for the evaporation rate is included which neglects the temporary peaks. The exact evaporation rate is in between the red solid line and the green trend curve.
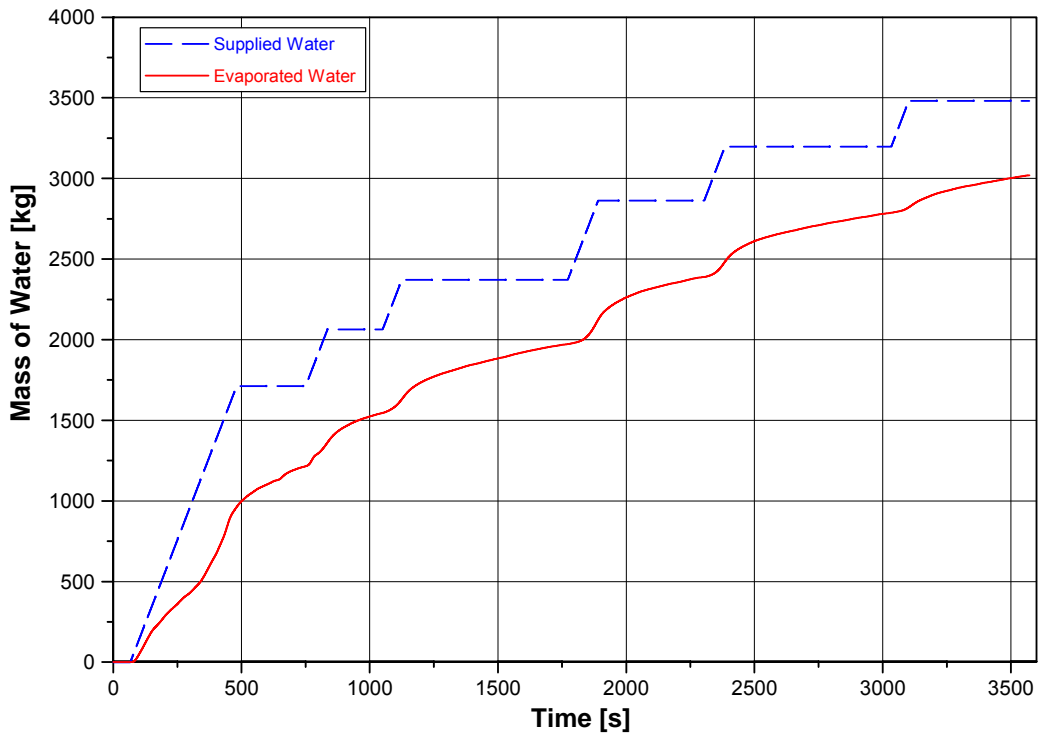
Figure 3-30: Integrated mass of supplied and evaporated water during top flooding

Integrating the curves of Figure 3-29 yields the total mass of supplied water and of the evaporated water, as given in Figure 3-30. Over the time period of 3102 s (52 min) when the sixth flooding phase stopped, 3480 kg water were supplied to the melt surface and 2825 kg water were evaporated or - to a lower fraction - lost by leakage or spill-over.

Using the evaporation rate $\dot{e}$ of Figure 3-29, the heat flux $\dot{q}$ per area extracted by evaporation through top flooding was determined by

$$\dot{q} = \dot{e} \cdot (c_p \cdot \Delta T + h_v) / A \ .$$

Therein the values for the water are: c_p the specific heat (4.183 kJ/kg·K); ΔT the temperature difference to boiling (80 K), h_v the heat of vaporization (2257 kJ/kg); A is the area of the melt surface including the support channel, and amounts to 4.81 m^2.

Figure 3-31 gives the calculated heat flux $\dot{q}$ versus time, which is proportional to the evaporation rate. Additionally the lower trend curve is given which eliminates the peaks generated by the water supply.

The time integral of the heat flux yields the total energy per area that was extracted by the top flooding process and is given in Figure 3-32. With the measured curve in the first hour of the experiment ECOKATS-2 an upper value for the total energy extracted by evaporation is 1.65 GJ/m^2. The lower trend curve delivers 0.97 GJ/m^2, which neglects the contributions of the peaks.

These results can be compared with the enthalpy of the melt in the characteristic temperature range. The enthalpy of the melt at the initial temperature of 1830 °C was calculated as 7.8 GJ. In a first estimate, it is assumed that the melt cools down to a homogenous temperature of 700 °C which was reached after about 1 hour (see Figure 3-6). This translates to a thermal energy of 5.6 GJ that had to be extracted. With the area of 4.81 m^2, the specific energy, to be extracted, amounts to 1.2 GJ/m^2, which is between the two experimental values. This means that the measured curve in Figure 3-32 overpredicts the energy extracted by the evaporation by more than 1/3. This may be partly due to the unknown leakages and to the overspill of some cooling water. The lower trend curve is below this estimate and may indicate that 80 % of the energy are transferred to the water overlayer, whereas the rest is transferred downwards and lateral to heat up and to melt the concrete cavity. Moreover, heat losses by radiation prior to flooding have to be taken into account.

A more detailed comparison can be made based on the calculation performed by Altstadt et al. for the ECOKATS-2 experiment [10]. In this calculation, the crust growth and the heat transfer from the flooded melt during ongoing MCCI are modelled (Figure 3-33). Heat transfer to the overlying water layer is calculated based on empirical correlations for a smooth surface, considering different boiling modes. Onset of solidification at the melt/water interface is modelled to form a stable horizontal crust without any downward water penetration. Under the crust the melt is well stirred by the gases from the decomposing concrete, until after 540 s the bulk of the melt reaches a sufficiently low temperature, for which immobilization of the melt occurs because of the high content of crystals in the melt (slurry). Then, further crust growth and cooling proceeds from the upper surface in the form of transient heat conduction. The calculated final downward concrete erosion of 1 - 2 cm is in a good agreement with the measured value.

Comparison with the measured upward heat flux in Fig. 3-31 shows a reasonable agreement between the calculated and the measured data, especially with the green trend curve. After onset of flooding the heat flux reduces from about 2 to 1 MW/m^2 after 200 s in both Figures. The subsequent increase of the measured heat flux, which is probably due to crust relocation and elevation, is not seen in the calculation. At 500 s, the experimental heat flux is 0.5 MW/m^2 to be compared with 0.7 MW/m^2 from the calculation. The corresponding data at 1000 s are 0.25 vs. 0.2 MW/m^2, and at 1500 s 0.2 vs. 0.16 MW/m^2, respectively. This agreement indicates, that the simple model of stable crust growth is nearly adequate to describe the cooling process by the overlaying water layer, and that indeed cooling by downward water progression, by whatever mechanism, has negligible effect on the majority of the melt. This corroborates the result which was derived from the structure of the bulk of the solidified melt. Only in the early phase of crust growth, some crust elevation or volcanic activities give rise to higher upward heat flux, as indicated in the major peak at 400 s.

Another important aspect observed in the experiment is the stability of the crust at the concrete wall. Calculations show that also in case of decay heat generation in the melt, the crust would be stably anchored with the concrete wall as the temperature at the contact zone is clearly below the concrete decomposition temperature allowing firm anchoring. It is top cooling which keeps crust and concrete wall stable.
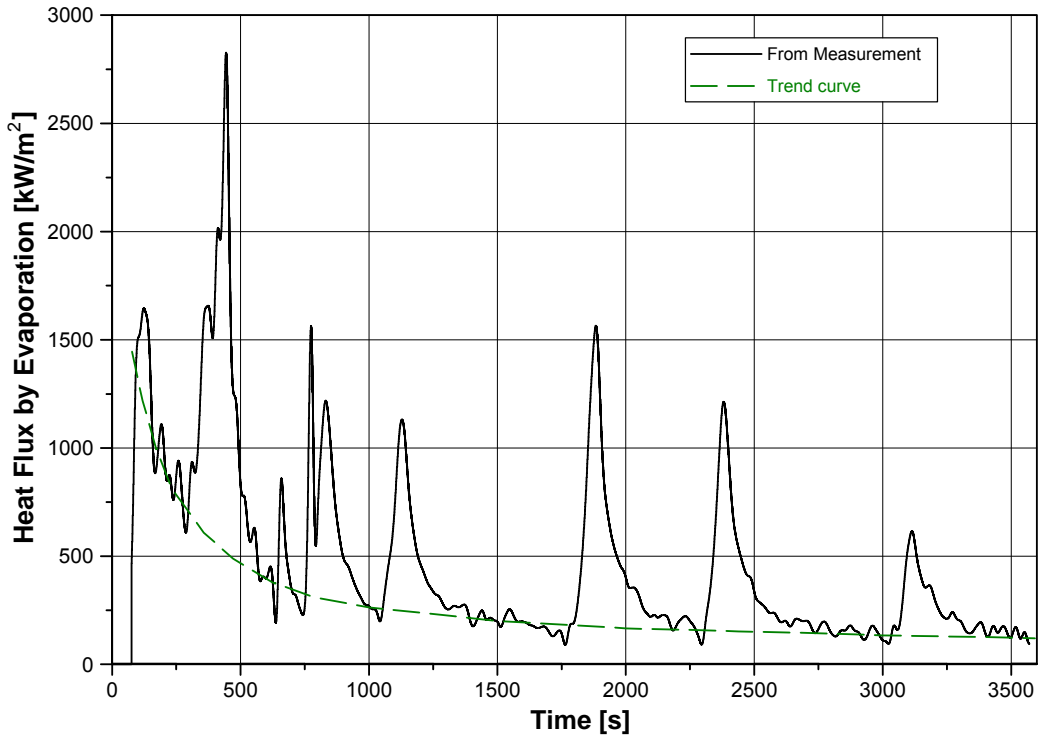
Figure 3-31: Heat flux per area by evaporation on top flooding
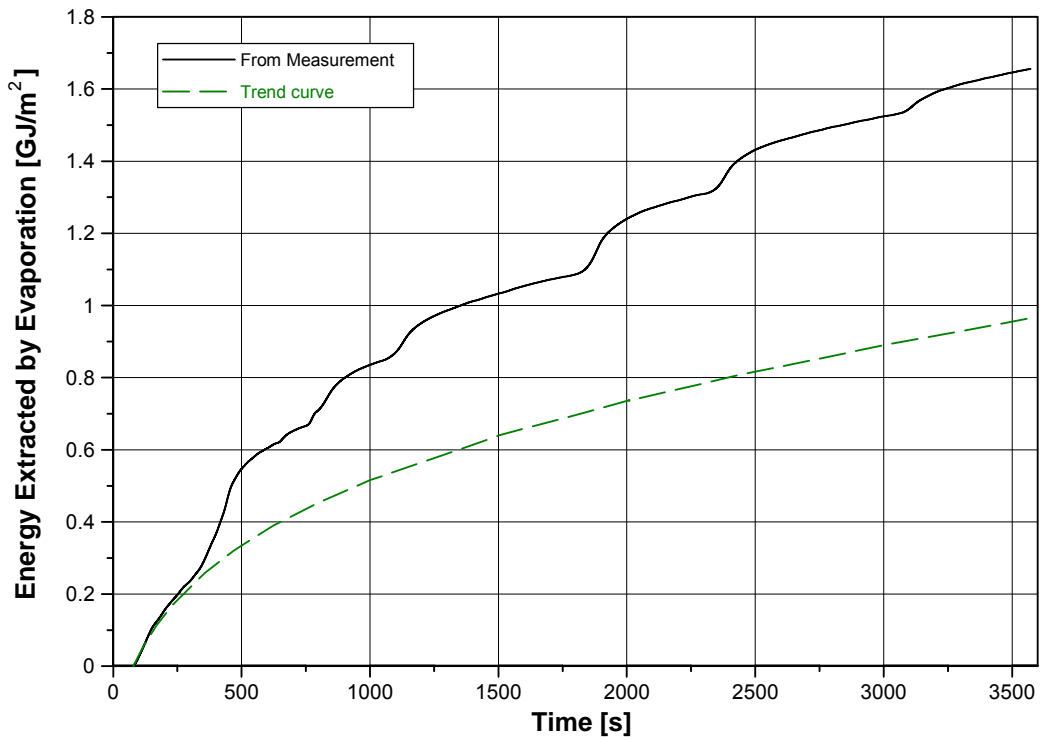
Figure 3-32: Cooling energy per area extracted by top flooding
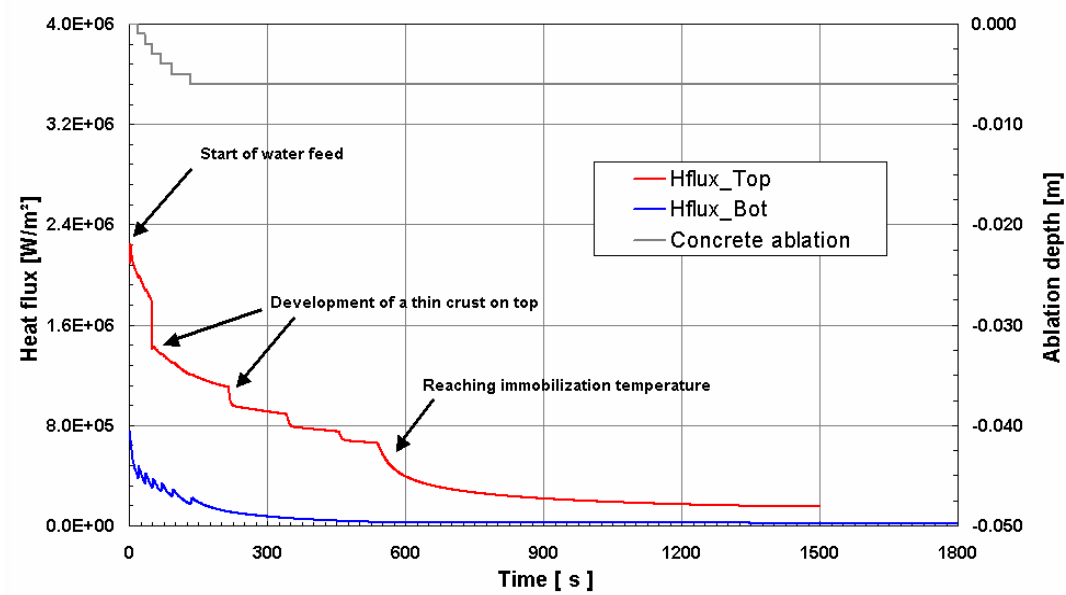
Figure 3-33: Heat flux and concrete ablation in ECOKATS-2 from theoretical models [10]; red: heat flux into the water layer, blue: heat flux into the concrete; grey: concrete ablation

4 Conclusions

The ECOKATS-2 experiment is the largest test on melt spreading and subsequent top flooding by water that has been performed so far. The experiment demonstrated very fast and highly efficient spreading for conditions of high melt release rate and some melt overheat. These are the conditions, which are expected under most accident conditions.

Top flooding which was initiated 30 s after the completion of spreading showed important phenomena during melt cooling by top flooding. It also clarified the influence of the concrete walls on the processes of crust formation and crust stability.

The following important processes were observed:

-    Spreading of the large melt mass of 3200 kg on the 2 m x 2 m concrete area was very efficient because of the high flow rate and the overheat of the released melt. Under these conditions, spreading was controlled by gravity and inertia forces and resulted in an evenly distributed melt some 20 cm high. This was accompanied by the well-known concrete erosion, leading to a high volume flux of gases from the concrete through the melt.

-    Top flooding of the agitated melt during the initial phase of concrete erosion was performed with 4.13 litres water/s. The contact of the upper oxide melt and water was very smooth and did not produce energetic melt/water interactions.

-    After flooding the 2 m x 2 m wide cavity, a closed surface crust was formed that firmly anchored to the vertical sidewalls of concrete. The crust at the walls was stable throughout the test, as heat extraction by the overlaying water layer was higher for the 2-D wall geometry than in the 1-D central cavity, and the wetted section of the vertical concrete wall acted like an additional heat sink. Theoretical analysis showed that at the contact zone of crust and vertical concrete wall, the wall is not eroded, as the temperature of the concrete remains below 700 K, for which the concrete is still stable and far from melting [10]. This is the necessary condition for crust anchoring. Below the crust, erosion of concrete occurs by the liquid melt into the lateral and downward direction.

-    The formation and persistence of the crust was a limiting factor for the further cooling processes. Initially the crust had a high temperature and was probably in film boiling condition. Quenching by the water overlayer occurred within a few minutes and resulted in a dark crust, which clearly showed the existence of a multitude of holes through which the gases from concrete were released.

-    About 50 % of the vent holes in the crust remained open during the further cooling process and were the origin of 16 volcanic vents that piled up by gas-driven, lava-like outflow of melt through the crust into the water layer. The height of the vents was 10 to 15 cm. No particles were ejected through the vents. This was different from the MACE experiments, where parts of the melt were ejected also in form of liquid particles [6]. The lava flow probably ended when locally the crust and melt separated, e. g. by lowering of the melt level.

-    The initially flat crust was slowly elevated in the centre of the spreading area by up to 20 cm, probably driven by gas release from the concrete. The crust in this region was irregular and had a high void with open and closed cavities. By this process, the uppermost 4 cm of the dense (unvoided) oxide melt were transferred into a highly porous structure, which could be cooled by the water overlayer through open cavities.

- The majority of the melt under the crust was not fragmented, and solidified without open porosity. This showed that ingression of coolant water to the bulk of the melt did not occur. Also, no significant cracks were visible in the lower solidified melt.

- In conclusion, this experiment on top flooding showed that a closed surface crust was formed on top of the melt, which was firmly anchored to the concrete sidewalls. Efficient cooling due to the formation of an upper crust with high porosity was restricted to the upper 4 cm of the original melt. The contribution of volcanic eruptions to coolabilty was smaller than expected, as no loose particles were ejected. The bulk of the oxide melt and the iron layer at the bottom were not cooled by water ingression from the top.

- Comparison with theoretical modelling shows that heat transfer and melt behaviour during cooling in the experiment are adequately described by transient heat transfer through conduction and convection in the presence of a stable, growing surface crust flooded by the water overlayer. Only in the early phase of crust growth, some crust elevation or volcanic activities give rise to higher upward heat flux.

With respect to reactor application the experiment showed that for deeper melt pools the stop of concrete erosion through top flooding only is unlikely. Efficient fragmentation and cooling was restricted to the upper few cm of the oxide melt, but this is not adequate to extract sufficient decay power from the bulk of the melt. Some uncertainties, however, persist from the present experiment as no decay heat could be simulated in the melt. Also, the properties of the melt were different, especially with respect to the oxide density and the level of the freezing temperature, and the spreading dimension in a reactor which is typical 6 m instead of 2 m. It is however unlikely, that this changes the sequence and importance of the observed coolant phenomena.

5 References

[1] H. ALSMEYER et al., *"Ex-Vessel Core Melt Stabilization Research (ECOSTAR)"*, FISA 2003 : EU Research in Reactor Safety, Luxembourg, L, November 10-13, 2003 Preproc S. 401-406

[2] H. ALSMEYER, Proc. of the OECD Workshop on Ex-Vessel Debris Coolability", Session B3: Spreading, p. 138-266, Forschungszentrum Karlsruhe, FZKA 6475 (2000)

[3] C. JOURNEAU et al., *"Ex-Vessel Corium Spreading: Results from the VULCANO Spreading Tests"*, Nucl. Eng. Des., 233, 75-102 (2003)

[4] C. SPENGLER et al., *"Blind Benchmark Calculations for Melt Spreading in the ECOSTAR Project "*, Proc. of ICAAP '04, Pittsburgh, Pa., USA, June 13-17, 2004 Madison, Wis.: Omnipress, 2004, S. 1220-31, CD-ROM

[5] B. R. SEHGAL, *"Stabilization and Termination of Severe Accidents in LWRs"*, Proc. NURETH-10, Seoul, Korea, October 5-11, 2003 American Nuclear Society : La Grange Park, Ill., 2004, CD-ROM

[6] M. T. FARMER, B. W. SPENCER, D. J. KILSDONK, *"Assessment of Water Ingression Phenomenon and proposed Separate Effect Tests"*, presented at MACE/TAC meeting, Palo Alto, Ca., USA (2000)

[7] J. V. BECK; B. BLACKWELL; C. R. ST.CLAIR, Jr, *"Inverse Heat Conduction. Ill-posed Problems"*, Wiley-Interscience, New York, 1985

[8] H. ALSMEYER, T. CRON, J.J. FOIT, G. MESSEMER, S. SCHMIDT-STIEFEL, W. HÄFNER, H. KRISCIO, *"Test Report of the Melt Spreading Tests ECOKATS-V1 and ECOKATS-1"*; ECOSTAR-Report SAM-ECOSTAR-D15, January, 2004, Forschungszentrum Karlsruhe

[9] J.J. FOIT, *Personal Communication* (2004)

[10] E. ALTSTADT, H.-G. WILLSCHUETZ, *"Melt Coolability by Top Flooding: Thermal and Mechanical Simulations on the ECOKATS2 Test"*; ECOSTAR-Report SAM-ECOSTAR-D41-D42-D43, February, 2004, Forschungszentrum Rossendorf, Dresden

[11] *GEMINI 2 Code for Thermochemical Equilibria Calculation*, Version 3.4 (2000), and *TDBCR97 Thermodynamic Database*, Thermodata Company, 38400 Saint Martin d'Heres, France

Appendix A   ECOKATS 2 Instrumentation Plan

A.1   Instrumentation Code

This table gives a short description of the sensor abbreviations and of the sensor locations

Abbreviation			Description
Char 1 - 4	Char 5	Char 6	
Sensor type			Sensor type
WOPLxx			WRe thermocouple (plunging type)
WOMAxx			WRe sheath thermocouple (mantle)
NIWIxx			NiCrNi wire thermocouple
NIMAxx			NiCrNi sheath thermocouple (mantle)
RTEM			Reference temperature sensor
LOAD			Load sensor
FLOWxx			Flow sensor
TRIG			Trigger input
	Location		Sensor location
	W		Whirl basin
	C		Supply channel
	1		Instrumentation module 1
	2		Instrumentation module 2
	3		Instrumentation module 3
	4		Instrumentation module 4
	0		Other
		Number	Identification number

A.2   Instrumentation Scheme

In the following table all the inserted sensors for the experiment ECOKATS-2 are listed. Here is the description of the abbreviations.

Block: Terminal block for the thermocouples, 2 blocks available, each with 50 terminals.

Term: Terminal number of block.

5B01 M: Number of the I/O subsystem module 5B01 from Analog Devices.
Each module has space for 16 input channels (0-15), each equipped with an amplifier matching the input signal.
3 modules are available.

5B01 CH: Channel number of the I/O subsystem module 5B01.

SCXI M: Number of the Multiplexer SCXI module from National Instruments with 32 channels.
Two 5B01 modules are per Multiplexer.
2 modules are available.

SCXI CH: Channel number of the Multiplexer SCXI

CH: Input channel number of the application program under LabWindows resp. the index in the data array.

Additionally measured environmental temperatures

RTEM01:   Temperature of the 5B01 module, integrated in the module.

RTEM02:   Temperature of the terminal block under the spreading cavity.
Thermocouple of type Pt-100

RTEM03:   Temperature of the environment outside the measuring container.
Thermocouple of type Pt-100

Special wiring for the load cells LOAD01-LOAD04

The load cells LOAD01 to LOAD04 are connected directly to four input channels of the multiplexer unit SCXI.
Each load cell has a cable with 7 conductors and is provided with a bridge amplifier.
Thus terminal 8 of the block Gx is free and terminal 9 and 10 yields the output signal.

Location	Identifier	Conductor	Block	Term	5B01 M	5B01Ch	SCXI M	SCXI Ch	Ch	Remarks
Whirl basin	WOPLW1	yellow (Scr)	1	1	1	0	1	0	0	Type D / 5B30-02
	WOPLW1	green +	1	2	1	0	1	0	0	Cable 17
	WOPLW1	red -	1	3	1	0	1	0	0	
	WOPLW2	yellow (Scr)	1	4	1	1	1	1	1	Type D / 5B30-02
	WOPLW2	red +	1	5	1	1	1	1	1	Cable 18
	WOPLW2	green -	1	6	1	1	1	1	1	
	WOPLW3	yellow (Scr)	1	7	1	2	1	2	2	Type D / 5B30-02
	WOPLW3	green +	1	8	1	2	1	2	2	Cable 20
	WOPLW3	red -	1	9	1	2	1	2	2	
Supply channel	WOPLC1	yellow (Scr)	1	10	1	3	1	3	3	Type D / 5B30-02
	WOPLC1	green +	1	11	1	3	1	3	3	Cable 14
	WOPLC1	red -	1	12	1	3	1	3	3	
	NIMAC1	black (Scr)	1	13	1	4	1	4	4	Typ K / 5B37-K-02
	NIMAC1	red +	1	14	1	4	1	4	4	Cable 13
	NIMAC1	green -	1	15	1	4	1	4	4	
	WOPLC2	yellow (Scr)	1	16	1	5	1	5	5	Type D / 5B30-02
	WOPLC2	red +	1	17	1	5	1	5	5	Cable 16
	WOPLC2	green -	1	18	1	5	1	5	5	
Instrument Module 1	WOPL11	Screen	1	19	1	6	1	6	6	Type D / 5B30-02
	WOPL11	blue +	1	20	1	6	1	6	6	(silicon cable)
	WOPL11	brown -	1	21	1	6	1	6	6	
			1	22	1	7	1	7	7	not applied
			1	23	1	7	1	7	7	
			1	24	1	7	1	7	7	
	NIWI11	Screen	1	25	1	8	1	8	8	Type K / 5B37-K-02
	NIWI11	green +	1	26	1	8	1	8	8	(red)
	NIWI11	white -	1	27	1	8	1	8	8	
	NIWI12	Screen	1	28	1	9	1	9	9	Type K / 5B37-K-02
	NIWI12	green +	1	29	1	9	1	9	9	(yellow)
	NIWI12	white -	1	30	1	9	1	9	9	
	NIWI13	Screen	1	31	1	10	1	10	10	Type K / 5B37-K-02
	NIWI13	green +	1	32	1	10	1	10	10	(blue)
	NIWI13	white -	1	33	1	10	1	10	10	
	NIWI14	Screen	1	34	1	11	1	11	11	Type K / 5B37-K-02
	NIWI14	green +	1	35	1	11	1	11	11	(black)
	NIWI14	white -	1	36	1	11	1	11	11	
Instrument Module 2	WOPL21	Screen	1	37	1	12	1	12	12	Type D / 5B30-02
	WOPL21	blue +	1	38	1	12	1	12	12	(silicon cable)
	WOPL21	brown -	1	39	1	12	1	12	12	
	NIWI21	Screen	1	40	1	13	1	13	13	Type K / 5B37-K-02
	NIWI21	green +	1	41	1	13	1	13	13	(red)
	NIWI21	white -	1	42	1	13	1	13	13	
	NIWI22	Screen	1	43	1	14	1	14	14	Type K / 5B37-K-02
	NIWI22	green +	1	44	1	14	1	14	14	(blue)
	NIWI22	white -	1	45	1	14	1	14	14	
	NIWI23	Screen	1	46	1	15	1	15	15	Type K / 5B37-K-02
	NIWI23	green +	1	47	1	15	1	15	15	(black)
	NIWI23	white -	1	48	1	15	1	15	15	
			1	49						
			1	50						
	NIWI24	Screen	2	1	2	0	1	16	16	Type K / 5B37-K-02
	NIWI24	green +	2	2	2	0	1	16	16	(blue)
	NIWI24	white -	2	3	2	0	1	16	16	
Instrument Module 3	WOPL31	Screen	2	4	2	1	1	17	17	Type D / 5B30-02
	WOPL31	blue +	2	5	2	1	1	17	17	(silicon cable)
	WOPL31	brown -	2	6	2	1	1	17	17	
			2	7	2	2	1	18	18	not applied
			2	8	2	2	1	18	18	
			2	9	2	2	1	18	18	
	NIWI31	Screen	2	10	2	3	1	19	19	Type K / 5B37-K-02
	NIWI31	green +	2	11	2	3	1	19	19	(red)
	NIWI31	white -	2	12	2	3	1	19	19	
	NIWI32	Screen	2	13	2	4	1	20	20	Type K / 5B37-K-02
	NIWI32	green +	2	14	2	4	1	20	20	(yellow)
	NIWI32	white -	2	15	2	4	1	20	20	
	NIWI33	Screen	2	16	2	5	1	21	21	Type K / 5B37-K-02
	NIWI33	green +	2	17	2	5	1	21	21	(blue)
	NIWI33	white -	2	18	2	5	1	21	21	
	NIWI34	Screen	2	19	2	6	1	22	22	Type K / 5B37-K-02
	NIWI34	green +	2	20	2	6	1	22	22	(black)
	NIWI34	white -	2	21	2	6	1	22	22	

Location	Identifier	Conductor	Block	Term	5B01 M	5B01Ch	SCXI M	SCXI Ch	Ch	Remarks
Instrument Module 4	WOPL41	Screen	2	22	2	7	1	23	23	Type D / 5B30-02
	WOPL41	blue +	2	23	2	7	1	23	23	(silicon cable)
	WOPL41	brown -	2	24	2	7	1	23	23	
	NIWI41	Screen	2	25	2	8	1	24	24	Type K / 5B37-K-02
	NIWI41	green +	2	26	2	8	1	24	24	(red)
	NIWI41	white -	2	27	2	8	1	24	24	
	NIWI42	Screen	2	28	2	9	1	25	25	Type K / 5B37-K-02
	NIWI42	green +	2	29	2	9	1	25	25	(yellow)
	NIWI42	white -	2	30	2	9	1	25	25	
	NIWI43	Screen	2	31	2	10	1	26	26	Type K / 5B37-K-02
	NIWI43	green +	2	32	2	10	1	26	26	(blue)
	NIWI43	white -	2	33	2	10	1	26	26	
	NIWI44	Screen	2	34	2	11	1	27	27	Type K / 5B37-K-02
	NIWI44	green +	2	35	2	11	1	27	27	(black)
	NIWI44	white -	2	36	2	11	1	27	27	
Diverse			2	37	2	12	1	28	28	not applied
			2	38	2	12	1	28	28	
			2	39	2	12	1	28	28	
	FLOW01	Screen	2	40	2	13	1	29	29	Type K / 5B32-02
	FLOW01	+			2	13	1	29	29	
	FLOW01	-			2	13	1	29	29	
	TRIG01	Screen	2	43	2	14	1	30	30	Signal provided by FZK
	TRIG01	red +	2	44	2	14	1	30	30	~24 V; voltage division: ~8 V
	TRIG01	black -	2	45	2	14	1	30	30	(5B31-03)
	RTEM02		2	46	2	15	1	31	31	Terminal block temp.
	RTEM02	HI red	2	47	2	15	1	31	31	Terminal 3 (5B34-03)
	RTEM02	LO yellow	2	48	2	15	1	31	31	Terminal 2
			2	49						
	RTEM02	RTN blue	2	50	2	15	1	31	31	Terminal 4
Load sensors	LOAD01	green	G1	1					32	Amplifier input
(spreading area)	LOAD01	grey	G1	2					32	
	LOAD01	white	G1	3					32	
	LOAD01	yellow	G1	4					32	
	LOAD01	pink	G1	5					32	
	LOAD01	brown	G1	6					32	
	LOAD01	Screen	G1	7					32	
	LOAD01		G1	8					32	
	LOAD01	grey-pink -	G1	9			2	0	32	Amplifier output <10 V
	LOAD01	blue-red +	G1	10			2	0	32	
	LOAD02	green	G2	1					33	Amplifier input
	LOAD02	grey	G2	2					33	
	LOAD02	white	G2	3					33	
	LOAD02	yellow	G2	4					33	
	LOAD02	pink	G2	5					33	
	LOAD02	brown	G2	6					33	
	LOAD02	Screen	G2	7					33	
	LOAD02		G2	8					33	
	LOAD02	white-green -	G2	9			2	1	33	Amplifier output <10 V
	LOAD02	brwn-green +	G2	10			2	1	33	
	LOAD03	green	G3	1					34	Amplifier input
	LOAD03	grey	G3	2					34	
	LOAD03	white	G3	3					34	
	LOAD03	yellow	G3	4					34	
	LOAD03	pink	G3	5					34	
	LOAD03	brown	G3	6					34	
	LOAD03	Screen	G3	7					34	
	LOAD03		G3	8					34	
	LOAD03	white -	G3	9			2	2	34	Amplifier output <10 V
	LOAD03	brown +	G3	10			2	2	34	
	LOAD04	green	G4	1					35	Amplifier input
	LOAD04	grey	G4	2					35	
	LOAD04	white	G4	3					35	
	LOAD04	yellow	G4	4					35	
	LOAD04	pink	G4	5					35	
	LOAD04	brown	G4	6					35	
	LOAD04	Screen	G4	7					35	
	LOAD04		G4	8					35	
	LOAD04	brown-olive -	G4	9			2	3	35	Amplifier output <10 V
	LOAD04	white-olive +	G4	10			2	3	35	

Location	Identifier	Conductor	Block	Term	5B01 M	5B01Ch	SCXI M	SCXI Ch	Ch	Remarks
LWL ports (not appl.)							2	4	36	not applied (LWL)
							2	4	36	
							2	4	36	
							2	5	37	
							2	5	37	
							2	5	37	
							2	6	38	
							2	6	38	
							2	6	38	
							2	7	39	not applied (LWL)
							2	7	39	
							2	7	39	
							2	8	40	
							2	8	40	
							2	8	40	
							2	9	41	
							2	9	41	
							2	9	41	
							2	10	42	not applied (LWL)
							2	10	42	
							2	10	42	
							2	11	43	
							2	11	43	
							2	11	43	
							2	12	44	
							2	12	44	
							2	12	44	
							2	13	45	not applied (LWL)
							2	13	45	
							2	13	45	
							2	14	46	
							2	14	46	
							2	14	46	
							2	15	47	
							2	15	47	
							2	15	47	
							2	16	48	not applied (LWL)
							2	16	48	
							2	16	48	
							2	17	49	
							2	17	49	
							2	17	49	
							2	18	50	
							2	18	50	
							2	18	50	
Reference temperatures	RTEM01				3	0	2	19	51	5B01 module temperature
	RTEM01				3	0	2	19	51	Wire bridge (5B37-K-02)
	RTEM01				3	0	2	19	51	Wire bridge
	RTEM03	RTN blue			3	1	2	20	52	Environment temp, terminal 4
	RTEM03	HI red			3	1	2	20	52	Terminal 3 (5B34-03)
	RTEM03	LO yellow			3	1	2	20	52	Terminal 2
Diverse	TRIG02	Screen			3	2	2	21	53	Signal provided by FZK
	TRIG02	red +			3	2	2	21	53	~6 V
	TRIG02	black -			3	2	2	21	53	(5B31-03)
							2	22	54	not applied
							2	22	54	
							2	22	54	
							2	23	55	not applied
							2	23	55	
							2	23	55	
Load sensors	LOAD00	Screen					2	24	56	Signal provided by FZK <10 V
(crucible)	LOAD00	black -					2	24	56	(without resistor packs:
	LOAD00	red +					2	24	56	RP4, RP8)

Location	Identifier	Conductor	Block	Term	5B01 M	5B01Ch	SCXI M	SCXI Ch	Ch	Remarks
							2	25	57	not applied
							2	25	57	
							2	25	57	
							2	26	58	not applied
							2	26	58	
							2	26	58	
							2	27	59	not applied
							2	27	59	
							2	27	59	
							2	28	60	not applied
							2	28	60	
							2	28	60	
							2	29	61	not applied
							2	29	61	
							2	29	61	
							2	30	62	not applied
							2	30	62	
							2	30	62	
							2	31	63	not applied
							2	31	63	
							2	31	63	
	NIWI15	Screen	3	1	4	0	3	0	64	Type K / 5B37-K-02
	NIWI15	green +	3	2	4	0	3	0	64	(black / red)
	NIWI15	white -	3	3	4	0	3	0	64	
	NIWI18	Screen	3	4	4	1	3	1	65	Type K / 5B37-K-02
	NIWI18	green +	3	5	4	1	3	1	65	(blue / yellow)
	NIWI18	white -	3	6	4	1	3	1	65	
	NIWI17	Screen	3	7	4	2	3	2	66	Type K / 5B37-K-02
	NIWI17	green +	3	8	4	2	3	2	66	(blue / red)
	NIWI17	white -	3	9	4	2	3	2	66	
	NIWI16	Screen	3	10	4	3	3	3	67	Type K / 5B37-K-02
	NIWI16	green +	3	11	4	3	3	3	67	(yellow / red)
	NIWI16	white -	3	12	4	3	3	3	67	
	NIWI25	Screen	3	13	4	4	3	4	68	Type K / 5B37-K-02
	NIWI25	green +	3	14	4	4	3	4	68	(black / red)
	NIWI25	white -	3	15	4	4	3	4	68	
	NIWI26	Screen	3	16	4	5	3	5	69	Type K / 5B37-K-02
	NIWI26	green +	3	17	4	5	3	5	69	(yellow / red)
	NIWI26	white -	3	18	4	5	3	5	69	
	NIWI27	Screen	3	19	4	6	3	6	70	Type K / 5B37-K-02
	NIWI27	green +	3	20	4	6	3	6	70	(blue / red)
	NIWI27	white -	3	21	4	6	3	6	70	
	NIWI28	Screen	3	22	4	7	3	7	71	Type K / 5B37-K-02
	NIWI28	green +	3	23	4	7	3	7	71	(blue / yellow)
	NIWI28	white -	3	24	4	7	3	7	71	
	NIWI35	Screen	3	25	4	8	3	8	72	Type K / 5B37-K-02
	NIWI35	green +	3	26	4	8	3	8	72	(black / red)
	NIWI35	white -	3	27	4	8	3	8	72	
	NIWI36	Screen	3	28	4	9	3	9	73	Type K / 5B37-K-02
	NIWI36	green +	3	29	4	9	3	9	73	(yellow / red)
	NIWI36	white -	3	30	4	9	3	9	73	
	NIWI37	Screen	3	31	4	10	3	10	74	Type K / 5B37-K-02
	NIWI37	green +	3	32	4	10	3	10	74	(blue / red)
	NIWI37	white -	3	33	4	10	3	10	74	
	NIWI38	Screen	3	34	4	11	3	11	75	Type K / 5B37-K-02
	NIWI38	green +	3	35	4	11	3	11	75	(blue / yellow)
	NIWI38	white -	3	36	4	11	3	11	75	
	NIWI45	Screen	3	37	4	12	3	12	76	Type K / 5B37-K-02
	NIWI45	green +	3	38	4	12	3	12	76	(black / red)
	NIWI45	white -	3	39	4	12	3	12	76	
	NIWI46	Screen	3	40	4	13	3	13	77	Type K / 5B37-K-02
	NIWI46	green +	3	41	4	13	3	13	77	(yellow / red)
	NIWI46	white -	3	42	4	13	3	13	77	
	NIWI47	Screen	3	43	4	14	3	14	78	Type K / 5B37-K-02
	NIWI47	green +	3	44	4	14	3	14	78	(blue / red)
	NIWI47	white -	3	45	4	14	3	14	78	
	NIWI48	Screen	3	46	4	15	3	15	79	Type K / 5B37-K-02
	NIWI48	green +	3	47	4	15	3	15	79	(blue / yellow)
	NIWI48	white -	3	48	4	15	3	15	79	
			1	49						
			1	50						